Alma Mater Studiorum · University of Bologna

school of science
Department of Physics and Astronomy
Master Degree in Physics

Synthesis and Optoelectronic Characterization of 2D/3D $MAPbBr_3$

Supervisor:
Prof. Daniela Cavalcoli

Co-supervisor:
Dr. Thibault Lemercier
Dr. Lorenzo Maserati

Submitted by:
Sophia Pinnavaia

Academic Year 2022/2023

Abstract

The excellent optoelectronic properties and the band gap tunability combined with ease of fabrication make perovskites the most promising materials for producing high efficiency solar cells, light emitting diode, laser, photodetector and radiation detectors. 3D perovskites, present a strong ions migrations and an easy moisture degradation that make them no ready for industrial use. 2D perovskites show a better resistance to moisture, but they are less efficient materials compared to 3D. 2D/3D perovskites could be the best compromise between 3D and 2D perovskite in order to achieve high optoelectronic performance. 2D/3D perovskite structure combines the stability and high resistance to moisture of 2D perovskites with good optical and charge carrier transport properties of 3D perovskites.
The aim of this work is to find the best process to fabricate 2D/3D $MAPbBr_3$ perovskites structure and to verify if the construction of a thin 2D perovskite layer on the 3D surface has passivated the surface defects and has improved the charge transport in 3D perovskite. The study on fabrication process of 2D/3D perovskites was performed at Neèl Institute (CNRS), Grenoble (France). It consisted on verifying through optical and SEM microscope image, absorbance, PL and XRD measurements the formation of 2D perovskite layer on surface $MAPbBr_3$ thin films after being treated with three different 2D perovskite solutions (PEA+Toluene, PEA+IPA and PEABr+IPA) for three diverse reaction time ($30''$, $3'$ and $10'$). The study on the charge transport and defect states was carried out at the Department of Physics and Astronomy (DIFA) of University of Bologna (Italy). It consisted on performing I-V and PICTS measurements on pristine and treated with PEA+Toluene thin films for $15''$, $1'$ and $10'$ and single crystals for $15''$ and $1'$. The times of treatment were chosen for such samples in order to study a case in which the treatment does not form a 2D perovskite and a case in which it forms with one or two layers of 2D perovskite. Current voltage characteristics and photocurrent analyses allowed for a detailed investigation of charge transport phenomena in 2D/3D perovskites.

Table of Contents

Introduction

Hybrid Perovskites are a class of semiconducting materials which have proven to be excellent active layers for optoelectronic devices like solar cells, light emitting diode, laser, photodetector and the radiation detectors. The 3D hybrid perovskites have high absorption coefficient, moderate mobility, long carrier diffusion length, direct and tunable band gap with simply halogen substitution and easy and low-cost process of fabrication, which make promising for many optoelectronic devices. However, these excellent properties are hindered by issues that make them no still ready for industrial use. The 3D perovskites are highly reactive to water and oxygen molecules in the atmosphere, leading to device instability and long term degradation under real operational conditions. The ion migration under external stimuli like light and applied voltage is another source of instability which leads to decrease of device performance. 2D perovskites, due to high resistance to moisture and the substantially suppression of ions migration, were intensively studied for replacing 3D perovskite. However, the strong quantum confinement at high number of layers, make them less efficient materials for fabricating optoelectronic devices. 2D/3D perovskites have been recently studied as the best compromise between 3D and 2D perovskite in order to achieve high optoelectronic performance. 2D/3D perovskite structure combines the stability and high resistance to moisture of 2D perovskites with good optical and charge carrier transport properties of 3D perovskites. The aim of this work is to find the best process to fabricate 2D/3D $MAPbBr_3$ perovskites structure and to verify if the construction of a thin 2D perovskite layer on the 3D surface has passivated the surface defects and has improved the charge transport in 3D perovskite. The study on fabrication of 2D/3D perovskites was performed at Neèl Institute (CNRS), Grenoble (France) and consisted on characterize $MAPbBr_3$ thin films after being treated with PEA+Toluene, PEA+IPA, PEABr+IPA for a time of reaction equal to 30 second ($30''$), 3 minute ($3'$) and 10 minute ($10'$) through optical microscope and S.E.M image, absorbance, PL and XRD measurements. The analysis on the charge transport and defect states was carried out at the Department of Physics and Astronomy (DIFA) of University of Bologna (Italy) and consisted on performing I-V and PICTS measurements on thin films and single crystals treated with PEA+Toluene respectively for $15''$, $1'$ and $10'$ and for $15''$ and $1'$. This thesis is structured in three chapters:

Chapter 1 gives an overview of the structural and optoelectronic properties of 3D, 2D and

2D/3D perovskites. The defects, which hinder the performance of 3D perovskite, are described. A general description of main application of hybrid perovskites is presented.

Chapter 2 describes the synthesis of $MAPbBr_3$ thin films, the growth of $MAPbBr_3$ single crystals and the fabrication of 2D/3D $MAPbBr_3$. It illustrates the experimental techniques (UV-Vis Spectroscopy, Florescence Spectroscopy, XRD, GIXRD) which allowed to verify the formation of 2D perovskite after being treated the 3D surface of thin films with a 2D perovskite solution and the method used to study the charge transport and the defect states (I-V and PICTS measurements) of thin films and single crystals treated with PEA+Toluene.

Chapter 3 describes the experimental results which have lead to select the best process to fabricate the 2D/3D $MAPbBr_3$ perovskite structure. The experimental analysis performed to characterize the defects states and charge transport of thin films and single crystals after being treated with PEA+Toluene is also described.

Chapter 1

Properties of Hybrid Perovskites and Applications

This chapter gives an overview of the structural and optoelectronic properties of 3D, 2D and 2D/3D perovskites and describes the defects present in 3D perovskites. The main optoelectronic applications of hybrid perovskites are illustrated at the end of this chapter.

1.1 Structural Properties

1.1.1 3D Perovskite

The 3D perovskites are a class of materials with chemical formula ABX_3, where A is a monovalent cation, B a divalent metallic cation, and X a halogen monovalent anion. The 3D perovskites with the A-site occupied by a small monovalent organic cation such as methylammonium ($[CH_3NH_3]^+$, MA^+) or formamidinium ($[CH(NH_2)_2]^+$, FA^+) are called hybrid perovskites because of their organic-inorganic nature, whereas those with Cs^+ in A site are said inorganic perovskites. The divalent metallic cation B is usually lead (Pb^{2+}) or tin (Sn^{2+}) whereas the halogen monovalent anion X is iodide (I^-), bromide (Br^-), chloride (Cl^-). The 3D perovskites with A= MA^+, B=Pb^{2+} and X=I^-, Cl^- are usually called lead halide perovskites. The cubic crystal structure of 3D perovskite is shown in Fig1.1a-b. The A is at the corner of the unit cell, B at center and X at the face center. In such crystal structure, the B atom is sixfold coordinated with the X atoms, creating a BX_6 octahedron that is interconnected via all corners to form a three-dimensional perovskite network (Fig.1.1a-b). In the perovskite structure the size of cation A must have a small size. Large dimension tilt the MX_6 octahedra or contract the lattice and leads to a modification of band gap. The cation at the B site influences the optoelectronic properties and the stability of perovskite. Usually the lead is preferred to tin as B site

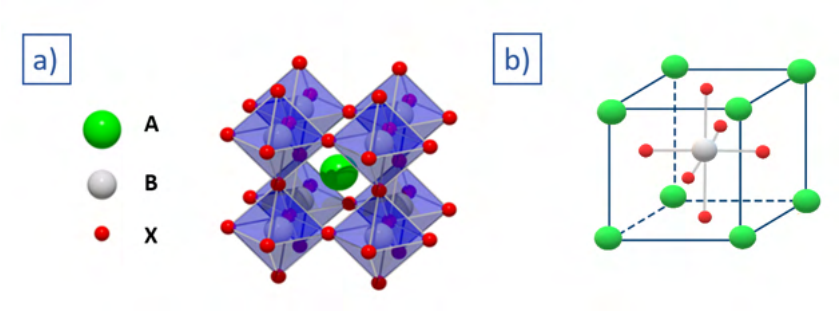

Figure 1.1: 3D Perovskite: a) Crystal Structure b) Unit Cell.

because tin, although it is less toxic, does not guarantee the high optoelectronic properties and good stability of lead. The halogen X is the part of perovskite structure which allows to tuning the band gap and optical absorption by simply substitution of halide. Moreover the halogen X, due to its higher electronegativity, enhances the ionicity of perovskite. The charge neutrality of hybrid perovskites is expressed as $A^+B^{2+}(X^-)_3$ where A^+ is balanced with $BX_3{}^-$. The stability of perovskite crystal is described by the Goldschmidt tolerance factor t which is a dimensional value calculated by the following formula:

$$t = \frac{(r_A + r_X)}{\sqrt{2}(r_B + r_X)} \tag{1.1}$$

where r_A, r_B and r_X are the ionic radii of A, B and X sites. The perovskites usually have a t value in the range 0.75-1 [5]. In table 1.1 the ionic radii value of A, B and X site are reported.

A^+	r_A (Å)	B^{2+}	r_B (Å)	X^-	r_X (Å)
Methylammonium: $[CH_3NH_3]^+$	2.17	Pb^{2+}	1.19	Cl^-	1.81
Formamidinium: $[HC(NH_2)_2]^+$	2.53	Sn^{2+}	1.10	Br^-	1.96
Cs^+	1.67			I^-	2.20

Table 1.1: Ionic radii (r_A, r_B, and r_X) of monovalent A site cation (A^+), divalent B-site cation (B^{2+}), and monovalent X-site anion (X^-) in ABX_3 halide perovskites [5]. The values are calculated by Kieslich and Shannon [2] [3].

The three-dimensional lead halide perovskites exhibit three temperature dependent phases of the crystal structure which are classified as: i) α phase (cubic), ii) β phase (tetragonal), iii) γ phase (orthorhombic). Fig.2.2 shows cubic structure (α phase) and formation of the tetragonal (β) and orthorhombic (γ) phases by the octahedral tilting of the α. The tetragonal and orthorhombic phase are non cubic structures characterized by

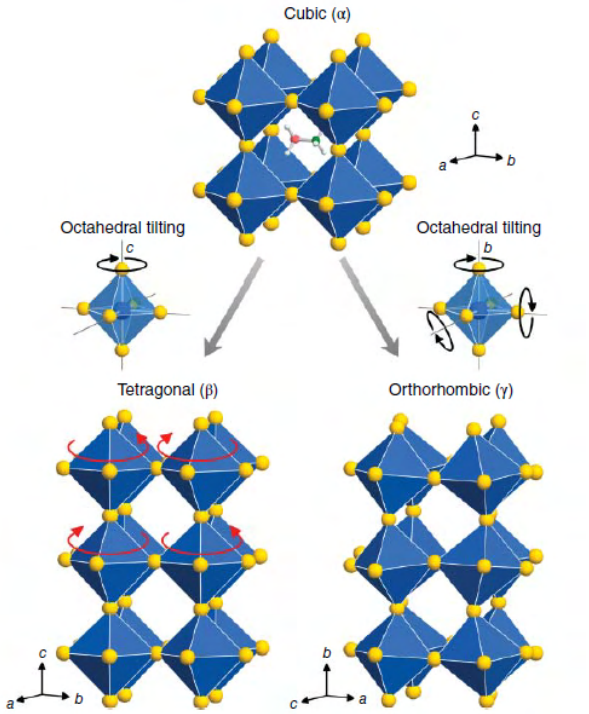

Figure 1.2: Cubic structure (α phase) and formation of the tetragonal (β) and orthorhombic (γ) phases by the octahedral tilting of the (α) phase crystal. The a, b, and c indicate the axis directions. From Ref[5].

a three-dimensional network of corner-sharing octahedra. In the β phase, only one tilting angle is different from zero, whereas all the tilting angles are non-zero in γ phase. In the β phase, PbX_6 octahedra are rotated only along the c-axis, while in γ the octahedra are tilted in all directions. The $MAPbI_3$ has three phase: the α phase at high temperature (T>327 K), β phase at room temperature and γ phase at low temperature (T<162 K)[5]. The $MAPbBr_3$ has α phase between 330K and 240K. The phase transition from α to β phase occurs around at 240K, whereas from β to γ at 130K[5]. The $MAPbCl_3$ has α until 177 K where there is phase transition from α phase to β. At 170K $MAPbCl_3$ changes phase from β to γ [4].

1.1.2 2D and 3D/2D Perovskite

The 2D perovskites consist of single (or multiple) inorganic sheets located between organic spacers held together by Coulombic forces. 2D perovskites have the general formula $R_2A_{n-1}B_nX_{3n+1}$, where R is an additional bulky organic cation that acts as a spacer between the inorganic sheets (Fig.1.3) and n defines the number of inorganic layers held together. On the contrary 3D, the layered structure of 2D perovskite allows to relaxes

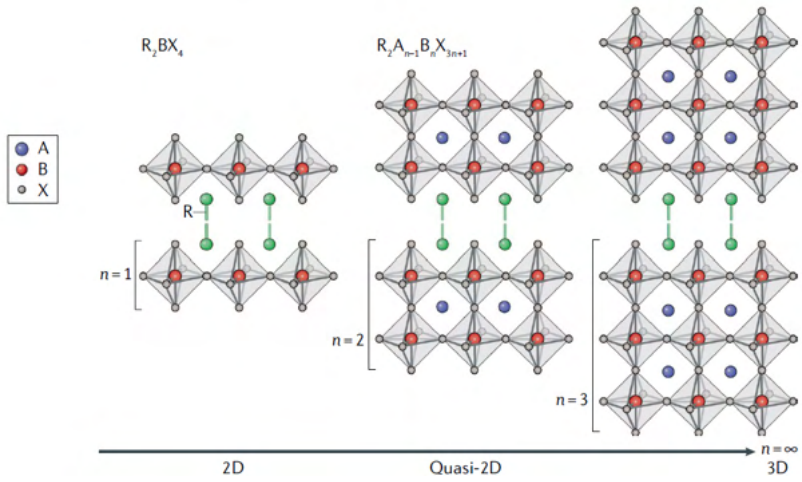

Figure 1.3: 2D perovskite structure with different number of perovskite layers (n). Adapted from Ref.[6].

the limit on dimension of A cation and to accommodate the bulky R cations between the inorganic sheets. This allows to have a wide choice of organic cation and to design it to have properties suited to a specific optoelectronic application. When n=1, 'pure-2D' perovskite, the bulky organic cations isolate single layers of the inorganic framework (figure 1.3). When n>1 a multi-layered structure, 'quasi-2D' perovskite, forms and a small organic cation (A) adds to crystal structure. At n=∞ 'quasi-2D' perovskite converges into 3D structure. Usually the phenylethylammonium (PEA^+) and butylammonium(BA^+) are employed as bulky R cations in 2D perovskites with n=1. For example the PEA_2PbI_4 and BA_2PbI_4 are the currently studied 2D perovskite with n=1 for many optoelectronic devices [6]. To synthesised 'quasi-2D' perovskites with n>1, the MA^+ is used as small organic cation. For example mixing PEA^+ and BA^+ with MA^+ the 'quasi-2D' perovskite $PEA_2MA_{n-1}Pb_nI_{3n+1}$ and $BA_2MA_{n-1}Pb_nI_{3n+1}$ are obtained. Because of the hydrophobic nature of R cation, highly oriented structure and dense packing, which reduces the density of grain boundaries and prevents direct contact of water, the 2D perovskites result more stable than 3D. However the narrow absorption in visible range, due to strong quantum confinement at high value of n, limits their use in some optoelectronic devices like solar cells. The 2D/3D perovskites are obtained by combining the 2D perovskite with 3D. The aim of this approach is to combining the superior stability of 2D with the high efficiency of 3D maintaining the structural integrity of the 2D phases. The 2D/3D structure are usually obtained by reaction of 3D surface with a 2D perovskite solution so that a 2D perovskite with one or more layers forms upon 3D. Fig.1.4a-b) shows the 2D/3D perovskite formed after the treatment of 3D perovskite with a 2D perovskite solution. Example of 2D/3D structure are 2D $BA_2MA_{n-1}Pb_nI_{3n+1}$/3D $MAPbI_3$, 2D $(BA)_2PbI_4$/ 3D $MAPbI_3$.

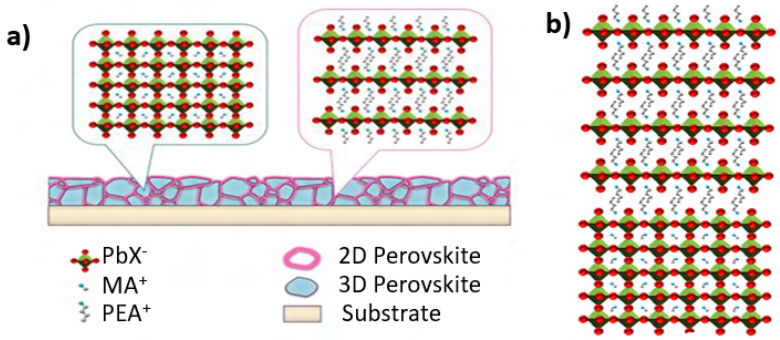

Figure 1.4: a) schematic representation of thin films treated with 2D solution to form 2D/3D stacked structure b) 2D/3D structure. Adapted from Ref.[17].

1.2 Optoelectronic properties

1.2.1 Band structure

3D hybrid perovskites are three dimensional semiconductors and can be described with an electronic band structure, where the valence band (VB) maximum and the conduction band (CB) minimum are separated by an energy gap E_G. The band structure of a semiconductor can form either a direct or indirect band-gap. In the direct case, the VB maximum and the CB minimum occur at the same point in the Brillouin zone. Experimental data and density functional theory (DFT) calculations determined that the lead halide perovskites are direct band-gap semiconductors[5]. There has been some evidence of a slightly indirect gap in lead halide perovskites, possibly induced by Rashba-splitting of the bands [6][5]. The band structure of lead halide perovskites is dictated by the Pb-X lattice, where an antibonding hybrid orbital between the s orbitals of Pb and p orbitals of X compose the VB maximum, while the CB minimum is formed by a non-bonding hybrid state between the p orbitals of Pb and the p orbitals of X. As a consequence to that, the band-gap of the material can be tuned by changing the halide composition, from lead iodide perovskites with band-gap around 1.6 eV to wider gaps around 2.4 eV in lead bromides and 3 eV in lead chlorides, covering the whole visible range. Fig.1.5 shows the band structure of $MAPbCl_3$, $MAPbBr_3$ and $MAPbI_3$. From these band structure we can see that the energy band gap is at R points and is equal to 3.11 eV, 2.22 eV and 1.51 eV respectively for $MAPbCl_3$, $MAPbBr_3$ and $MAPbI_3$.
DFT calculation and experimental measures have shown that 2D perovskites are direct gap materials. The peculiar characteristics of 2D perovskites is that that the energetic alignment of band edges change with the number of layers. The energy of the valence band (VB) maximum increases with a decrease in dimensionality from n =1 to n = ∞ and the energy of the conduction band (CB) minimum increases in parallel with the VB edge. This means that 2D perovskites with low number of layers have large band

gap, whereas those with large number of layers have narrow band gap. As example, Fig.2.1 shows the electronic band structure of 2D perovskites $(BA)_2(MA)_{n-1}Pb_nI_{3n+1}$ with n=1, 3, 4. The energy band gap is 1.99 eV for n=1 , 1.78 eV for n=3 and 0.99 for n=4 [12]. The electronic band structure of 2D/3D perovskites is still matter of study. Recently some research groups have been shown that the electronic band structure of 2D/3D perovskites preserve the characteristic of that 2D and 3D [6][17][10].

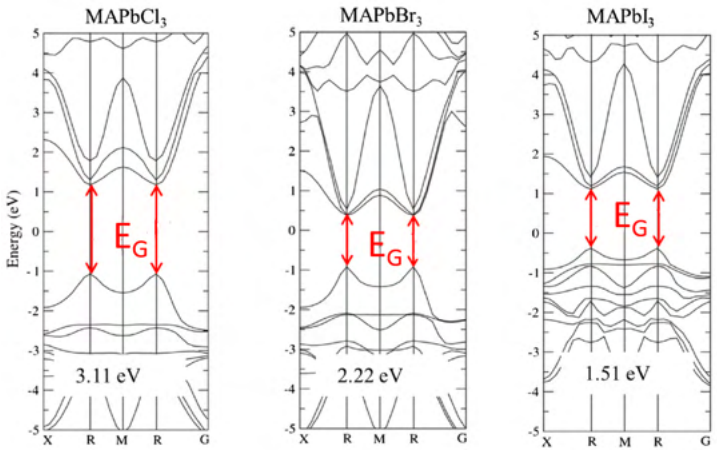

Figure 1.5: Electronic Band Structure of $MAPbX_3$ where X=Cl, Br and I. From Ref [8].

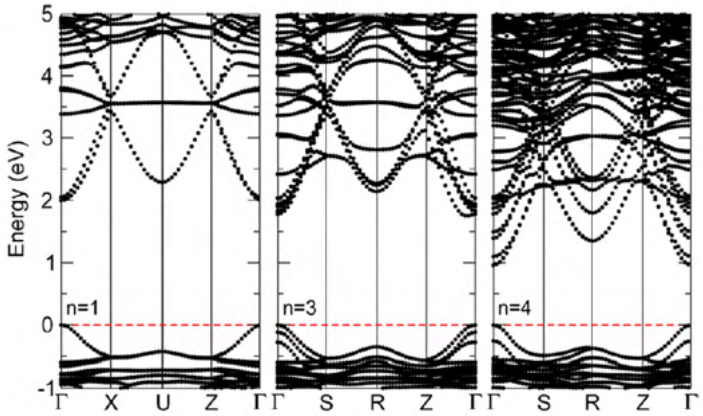

Figure 1.6: Electronic Band Structure of 2D perovskites $(BA)_2(MA)_{n-1}Pb_nI_{3n+1}$ with n=1, 3, 4. From Ref [12].

1.2.2 Charge Transport Properties

3D perovskites are characterized by moderate mobility (14-217 $cm^2\ V^{-1}s^{-1}$ for holes and 25–190 $cm^2\ V^{-1}s^{-1}$ in single crystals $MAPbBr_3$[22]), long diffusion length ($> 1\mu m$[5])

and higher resistivity (10^8-10^9 Ωcm[5]) which make them interesting materials for many optoelectronic applications. However the main characteristic of 3D perovskites is that ions move under external stimuli like light or applied voltage. The ions migration is a temperature dependent process and it is caused principally by native point defects such as iodine vacancy in $MAPbI_3$ or bromine vacancy in $MAPbBr_3$. Ions migration causes the hysteresis in current density-voltage (J-V) characteristics of 3D perovskite solar cells which limits their performance and their stability[5][23][9]. As example, the room temperature J-V characteristics in the dark of $MAPbI_3$-based the solar cell in Fig.1.7 show the hysteresis which is due to ions migration under applied voltage[9].

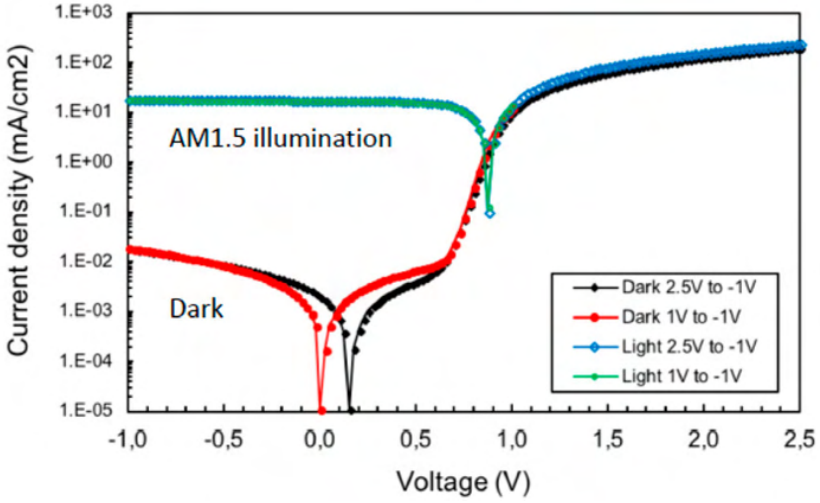

Figure 1.7: J-V characteristics of the $MAPbI_3$-based perovskite solar cells in dark and under 1 sun illumination as a function of the initial applied voltage. From Ref [9].

The conductivity in 3D perovskite consists of charge and ionic conductivity and depends exponentially on the temperature. At low temperature, ions are fixed and the ionic conductivity is very low while when the temperature increases, the ions began to migrate and contribute to the conductivity[19]. The parameter which quantifies the rate of ions migration is the ion migration activation energy E_a and it can be derived from the temperature-dependent electrical conductivity (σ) using the Nernst-Einstein relation[9][19][24]:

$$\sigma(T) = \left(-\frac{\sigma_0}{T}\right) \exp\left(-\frac{E_a}{k_b T}\right) \tag{1.2}$$

where σ_0 is a constant, k_b and T are respectively the Boltzmann constant and the absolute temperature. Lower value of E_a means that ions can migrate easily in the lattice giving a important contribution to charge transport. High value of E_a instead means that ions migration is hampered and electrons or holes contribute principally to transport. Fig.1.8 the conductivity of the perovskite film measured in the dark is plotted versus 1/T in the

Nernst-Einstein formalism. Two conduction regimes are clearly observed: ionic conduction regime at high temperature and electronic conduction regime at low temperature.

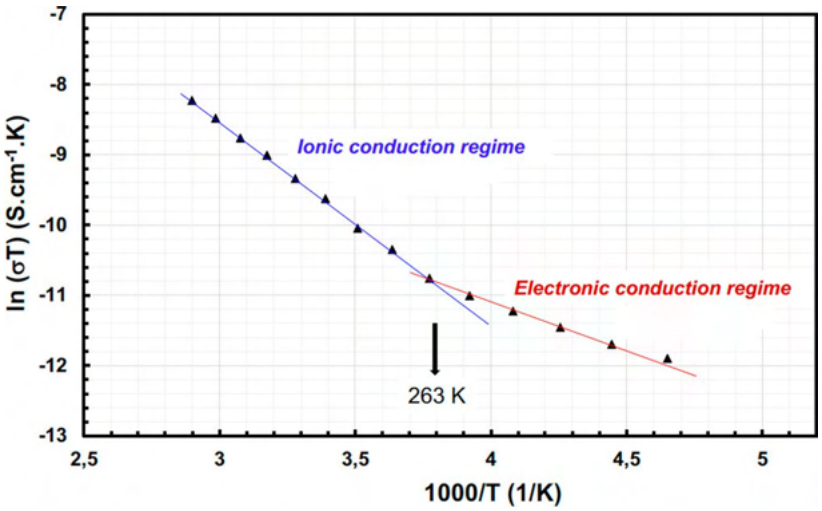

Figure 1.8: Conductivity of the metal halide perovskites as a function of the temperature. From Ref [9].

The change from ionic to electronic conduction is found at 263 K. This temperature value is often reported in literature for 3D $MAPbI_3$ or $MAPbBr_3$[9][18][19]. The activation energies reported for 3D perovskite are typically between 0.2-0.8 eV. This means that ion migration is much more active in 3D perovskites and that a relevant ionic contribution to charge transport is expected. The poor stability under real operative conditions of 3D perovskite is main due to this higher ions migration and represents the main issues which make 3D perovskite based devices non still ready for industrial use. The 2D perovskites exhibit higher activation energy and a substantially suppressed ion migration compared to 3D[10]. This explains the long-term stability compared to 3D perovskites. However the 2D perovskites show low conductivity compared to 3D[6] which limit their use in some optoelectronic applications like solar cells or photodetectors[6]. The effect on hampering the ions migration by introducing a thin layer of 2D perovskite (n=1) upon 3D surface to form a 2D/3D perovskites is still matter of study. Recent studies have shown that 2D/3D perovskites are characterized by higher ions migration activation and a major stability than 3D perovskite[18][19]. Moreover it was demonstrated by some research groups that 2D/3D perovskites have higher conductivity compared to 2D and closed to that 3D [7][18][19].

1.2.3 Optical Absorption

When light impinges on a semiconductor with thickness d (figure1.9a), it gets absorbed and the intensity exponentially decreases as it goes through the material. The relation-

ship between the intensity of impinging light I_0 and the intensity I of light passed through the semiconductor (transmitted light) can be expressed through the Beer-Lambert's law:

$$I(d) = I_0 e^{\alpha(\lambda)d} \tag{1.3}$$

where $\alpha(\lambda)$ is the wavelength-dependent absorption coefficient. When the photon, that impinges on the semiconductor, has energy equal or higher than the energy band gap E_G of material an electron can be promoted from the VB to the CB leaving a hole in the VB. In direct band gap semiconductor, the VB and CB are aligned, and the electron can be directly excited from VB to CD without change of wavevector $\vec{K}$(figure 1.9b). In indirect band gap semiconductor, the VB and CB are not aligned, and the promotion of electron from VB to CB involve the interactions of photon and phonons in order to overcome the distance between conduction and valence bands in $\vec{K}$ space(Fig.1.9c). This process which involves three particles (photon, phonon and electrons) is slow and less efficient than that in direct band gap semiconductor. For this reason the direct band gap semiconductors are materials widely used in optoelectronic devices (solar cells, LED, laser).

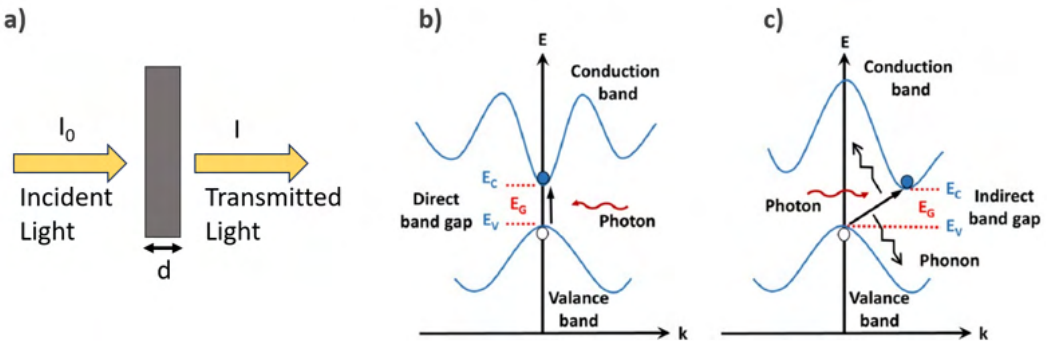

Figure 1.9: a) Light transmitted through a semiconductors of thickness d b-c) Photon absorption in direct (left) and indirect (right) bandgap semiconductor.

3D perovskites are direct gap semiconductor which exhibit high absorption coefficient ($\alpha \sim 10^5$ cm^{-1}) in the visible-ultraviolet (UV) region. Fig.1.10 summarizes the α spectra of methylammonium lead iodide ($MAPbI_3$), formamidinium lead iodide ($FAPbI_3$), methylammonium lead bromide $MAPbBr_3$, $CsFAPb(I_{1-x}Br_x)_3$ and $FAMA(Sn,Pb)I_3$ with x=0.0, 0.2 and 0.4. High absorption coefficient is fundamental property for perovskite solar cells and photodetectors because the spin coating process does not allow to fabricate thinner absorber making difficult the photogeneration and the collection of carriers. The 2D perovskites are characterized by absorption spectra which depends on the number of layers. As an example, the Fig.1.11a shows the absorption spectra of 'quasi-2D perovskite' $BA_2MA_{n-1}Pb_nI_{3n+1}$ with n=1, 2, 3, 4 and n=∞. The 2D perovskites with n< 3, because of strong quantum confinement, have narrow absorption with one or more

peaks and large band gap [6]. The perovskites with n> 3 have instead a large absorption in UV visible with one peak and narrow band gap. The absorbance spectra converge to that of 3D perovskite at n=∞. The absorption spectra of 2D/3D perovskite is combination of 3D and 2D perovskite absorption spectra. As an example, Fig.1.11b shows the absorption spectra 2D/3D perovskite (2D $BA_2MA_{n-1}Pb_nI_{3n+1}$/3D $MAPbI_3$) measured through UV-Vis spectroscopy. The 3D perovskite absorbance peak is slightly reduced after introduction of 2D layer, and peaks of 2D perovskite with n=2,3,4 are present together to that of 3D perovskite.

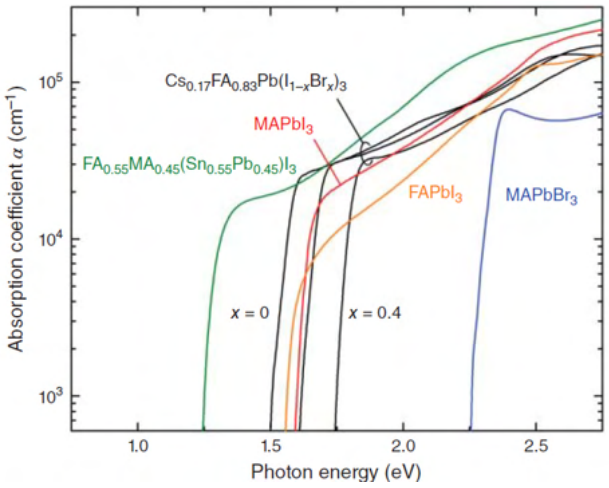

Figure 1.10: α spectra of various hybrid perovskites ($MAPbI_3$, $FAPbI_3$, $MAPbBr_3$, $CsFAPb(I_{1-x}Br_x)_3$ and $FAMA(Sn,Pb)I_3$ determined by spectroscopic ellipsometry. From Ref.[5]

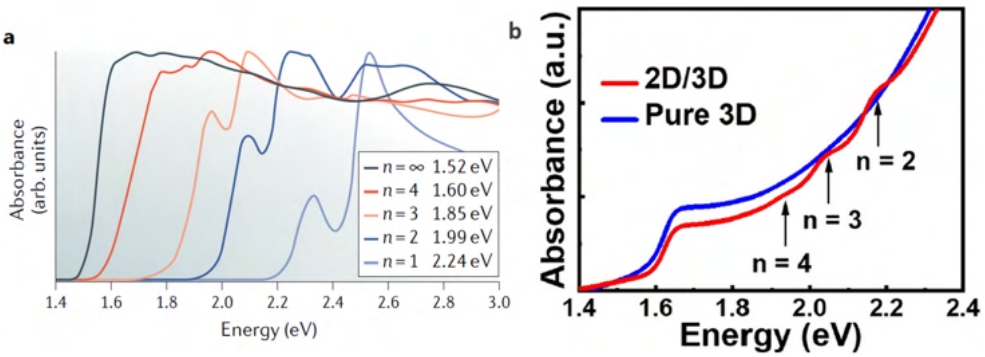

Figure 1.11: a) Absorption spectra of 'quasi-2D' $BA_2MA_{n-1}Pb_nI_{3n+1}$ perovskites determined by UV-Vis spectroscopy. The value of band gap are also listed. From Ref.[6] b) Absorption spectra 2D/3D perovskite (2D $BA_2MA_{n-1}Pb_nI_{3n+1}$/3D $MAPbI_3$) by UV-Vis spectroscopy. From Ref[11].

1.2.4 Photoluminescence

Photoluminescence (PL) is a physical process in which light is emitted from a material after the absorption of photons. In semiconductors, this process is observed only in those with direct bandgap, since the emission of photon in indirect band gap is less probable due to non aligned VB and CB. The emission of light from a direct gap semiconductor can be explained considering the band diagram in Fig.1.12. When light with energy equal or higher than energy band gap of the material impinges on a semiconductor, electrons and holes are generated in CB and VB (figure1.12a) which rapidly fall to conduction band bottom and valence band top by thermalization, typically within the timescale of picoseconds. The radiative recombination of electron and holes leads to light emission (PL) (figure1.12b).

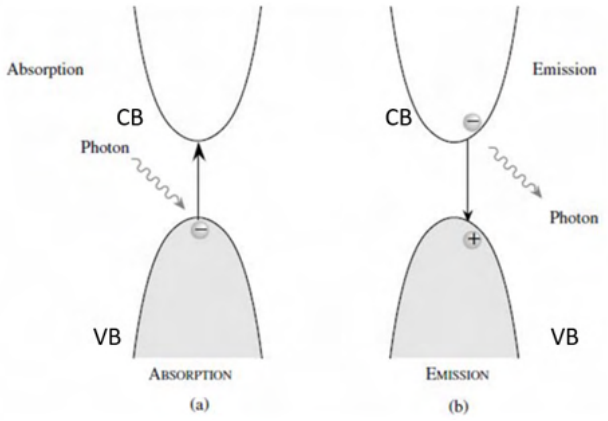

Figure 1.12: schematic illustration for photoexcitation (optical absorption) and emission (PL) in direct gap semiconductor.

The 3D perovskites are characterized by PL spectral shape with broad linewidth (∼100meV for $MAPbI_3$[5]) and by PL emission that changes with halogen substitution as shown Fig.1.13a. $MAPbI_3$, $MAPbBr_3$, and $MAPbCl_3$ have respectively PL energy peak at 1.6 eV, 2.3 eV and 3.2eV [5]. All this materials display strong room temperature PL as shown in Fig.1.13b. The halogen substitution(I→ Br→Cl) shifts the band gap energy to the higher energy side, which covers from the near-UV to the near-infrared spectral region. The top of Fig.1.13a shows PL spectra of $MAPbI_3$, $MAPbBr_3$, and $MAPbCl_3$ thin films (dotted curves) and single crystals (solid curves). The different PL spectral shape between thin films and single crystals is attributable to the photon reabsorption effect. The 3D perovskite are materials which do not show Stokes shift. As an example, the lower panel of graph in Fig.1.13a shows that there is no difference between the positions of the band maxima of the absorption and emission spectra. The 2D perovskites are characterized by PL spectral shape with narrow bandwidth and by PL emission that depends on the number of layers (n). As an example, Fig.1.14a shows

the room temperature PL spectra of 'quasi 2D perovskite' $BA_2MA_{n-1}Pb_nI_{3n+1}$ with n=1,2,3,4 and n=∞. The PL energy peak decreases with increasing of n value from n=1 to n=∞. This behaviour is due to strong quantum confinement at high value of n. The 2D/3D perovskites are characterized by a PL spectra which comprise the emission of 2D and 3D perovskite. As an example, Fig.1.14b reports the PL spectra of spectra 2D/3D perovskite (2D $BA_2MA_{n-1}Pb_nI_{3n+1}$/3D $MAPbI_3$) measured through steady state fluorescence spectroscopy. The 3D perovskite PL curve is the same of 3D after the introduction of 2D perovskite, and 2D perovskite PL peak with n=3 and n=4 is present together to that of 3D perovskite.

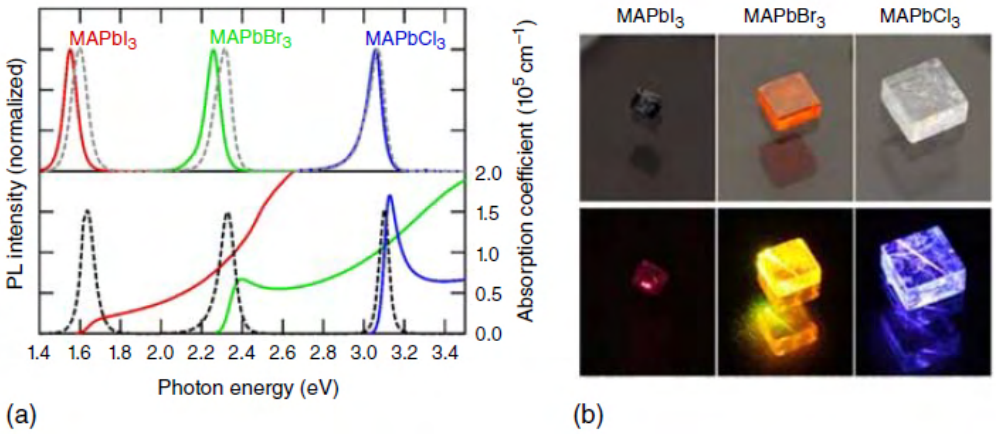

Figure 1.13: (a) PL spectra of $MAPbI_3$, $MAPbBr_3$, and $MAPbCl_3$ thin films (dotted curves) and single crystals (solid curves). Optical absorption spectra are also plotted in the lower panel. (b) Photographs of $MAPbI_3$, $MAPbBr_3$, and $MAPbCl_3$ single crystals. From Ref.[5].

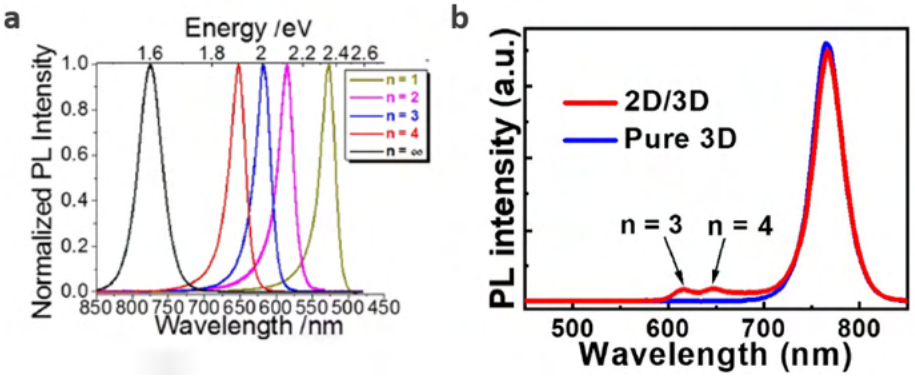

Figure 1.14: a) PL spectra of 'quasi-2D' $BA_2MA_{n-1}Pb_nI_{3n+1}$ perovskites. From Ref.[12] b) PL spectra 2D/3D perovskite (2D $BA_2MA_{n-1}Pb_nI_{3n+1}$/3D $MAPbI_3$). From Ref[11].

1.2.5 Excitons

Excitons are quasi-particles resulting from the Coulomb interaction between an electron and hole pair. The exciton is regarded as an elementary excitation of condensed matter which can transport energy without transporting net electric charge. The value of the exciton binding energy E_b is particularly relevant for both photodetectors and solar cells because determine the energy necessary to dissociate it and to create free charge carriers. In inorganic semiconductors, the exciton binding energy is low enough (few meV) to allow the separation of the pair quite immediately with the absorption of light, thus creating free charge carriers at room temperature. These excitons are called Wannier exciton and are characterized by a low binding energy and wavefunction strongly delocalized. For this reason such quasi-particles are also called a free excitons. In organic semiconductors, the light does not create immediately free charges, because excitons have binding energy(of order of several eV) much larger than the thermal energy($\sim$25 meV). These excitons are called Frenkel excitons and characterized by a large binding energy and wavefunction strongly localized at a specific atom or molecule. 3D perovskites are hybrid materials (both organic and inorganic) and although their excitation binding energy lies in a regime intermediate between tightly bound organic Frenkel exciton and the loosely bound inorganic Wannier one, the majority of excitations in perovskite materials are free carriers like in low-gap inorganic semiconductors [7]. Values for E_b for halide perovskite reported in literature are comprised between 2 meV and 60 meV, with lower values for lead iodide perovskites compared to lead bromides[7]. Unlike 3D perovskite stable excitons form in 2D perovskites at room temperature, with large exciton binding energies up to hundreds of meV[6]. The large binding energies are due to the mismatch between the dielectric constants of the organic and inorganic layers and the low dielectric screening from the organic sheets. The exciton binding energy progressively decreases with increasing n, that is, on going from a pure 2D to a fully 3D perovskite structure[6]. In 2D/3D perovskites, due to mixed structure, excitons of the same type as 3D and 2D perovskites are formed[6][10].
Several research groups have demonstrated that the peak presents in both absorption and PL spectra can be attributed to absorption of exciton states and to exciton recombination[7][8]. Fig.1.15 reports the experimental measured absorbance and PL spectra of $MAPbBr_3$ fitted using Elliott formula and line shape analysis which reveal as the peak in absorbance an PL spectra are due to exciton absorption and recombination, rather than the band-to-band transition.

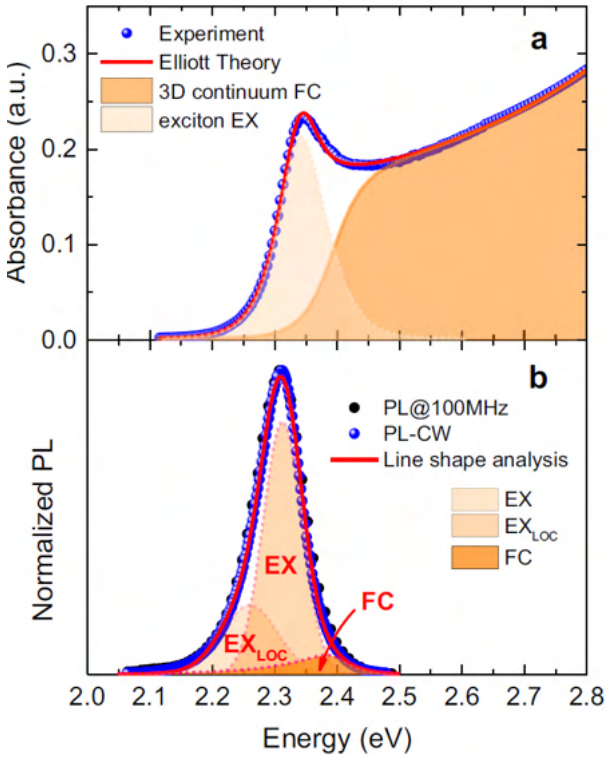

Figure 1.15: Absorption and photoluminescence spectra of $MAPbBr_3$ films with line-shape analysis. a) Absorption spectrum with Elliott theory fitting. b) Photoluminescence (PL) spectrum with line-shape analysis. The red lines through the experimental data (blue symbols, indicating the obtained continuous-wave PL, named PL-CW in the legend) represent the best fit. The single PL components are also highlighted for free/localized excitons (EX/ EX_{LOC} in the legend, indicated by the light-orange-shadowed areas) and for free carriers (FC in the legend, indicated by the dark-orange-shadowed area). The contribution of the single components to the total PL area results to be 66% (25%) for free (localized) excitons, and less than 9% for free carriers. From [8].

1.3 Defects

Defects in semiconductors can be categorized as crystallographic defects and impurities. Crystallographic defects are interruptions to an otherwise perfect crystal lattice and can be classified in point defects such as atomic vacancies, interstitials and anti-site substitutions (atoms occupying the wrong site in lattice) and higher dimensional defects such as grain boundaries, dislocations and precipitates. Defects introduce electronic states within the forbidden gap of the semiconductor. The activation energy (E_a) is defined as the energy difference between the defect state and the corresponding band.

The capture cross section σ quantifies the ease with which a defect level capture a mobile carrier. Typically, defect states are classified as shallow and deep. The shallow defects are close to the band edges (either conduction band or valence band) and have low activation energy and capture cross section. When a shallow defect capture a charge carrier (electron or hole), this will be easily remitted back to the nearest energy band due to thermal excitation. The shallow traps act as a trap and not recombination center. Deep defects are positioned deeper in the band gap and have higher activation energy and large capture cross section. When a carriers is captured by deep defect, it will recombine non radiatively emitting of a phonon. The non-radiative recombination process is one of important loss mechanism in solar cells. Fig.1.17 describes the schematic representation of the ideal tetragonal perovskite crystal lattice with AMX_3 formula and defects present in it. In the following two sections the point defects and grain boundaries in metal halide perovskite are described.

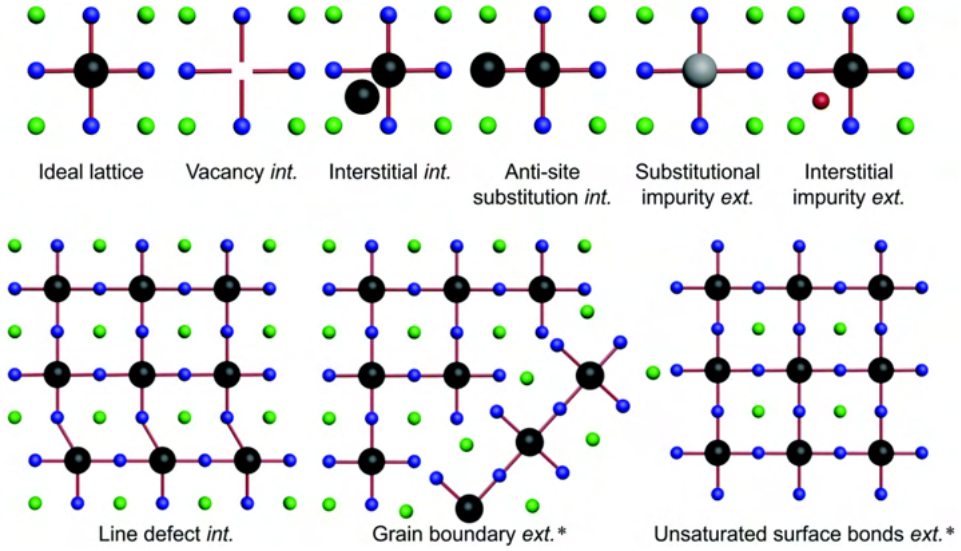

Figure 1.16: schematic representation of an ideal perovskite lattice with AMX_3 formula and the possible defects in it (green, black and blue dots represent the A-, M- and X-site; Red and grey dots represent the impurities). From Ref. [13].

1.3.1 Point defects in 3D Perovskite

The point defects in halide perovskite can be interstitial (I), vacancy (V) or substitutional defects. These are ionic defects which are not static, but they move in response to external stimuli such as voltage or light. In $MAPbI_3$, the possible types of defects are vacancies V_{MA}, V_{Pb} and V_I, interstitials MA_i, Pb_i, and I_i and anti-site MA_{Pb}, Pb_{MA}, MA_I, I_{MA} and I_{Pb}. The energy levels associated with the ionic point defects in $MAPbI_3$

are shown in Fig.1.17 where shallow traps are indicated by grey and deep traps indicated by orange colour. The interstitials (Pb_i, I_i, I_{MA}) and anti-site (Pb_I, I_{Pb}) defects are positioned at the deep electronic levels resulting in non-radiative recombination. Defects like I_i or MA_i, with relatively low formation energy, form shallow levels. A similar behaviour is found for the bromide perovskite.

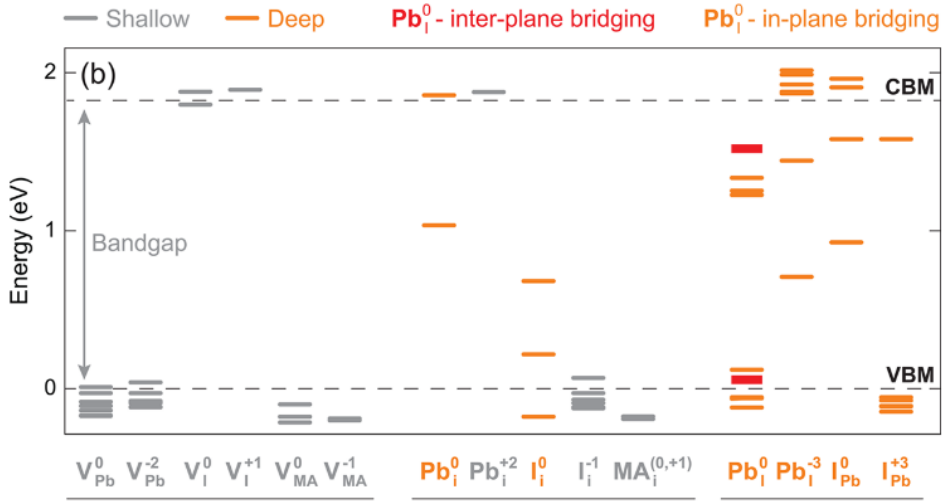

Figure 1.17: Energy levels associated with the defect states corresponding to neutral and charged vacancies (V_{Pb}, V_I, V_{MA}), neutral and charged interstitials (Pb_i, I_i, MA_i), and neutral and charged states associated with anti-sites (Pb_I and I_{Pb}). From Ref.[13].

1.3.2 Grain Boundaries in 3D Perovskite

Grain boundaries (GBs) are defined as an interface that separates grains with different crystal orientations and they are regions in which dangling bonds, impurities or point defects can bond. GBs are planar defects or 2D defects in the crystal structure and they introduce a defect states within the forbidden gap of semiconductors. The local electronic states formed by grain boundaries are strictly dependent on their distinctive crystallography and chemical bondings. Fig.1.18 shows the typical top view of polycrystalline perovskite thin film. The grain size of 3D perovskites polycrystalline thin films varies between several tenths of nanometers to millimeters depending on processing conditions such as temperature, a solution concentration, processing environment, posttreatment, and additive incorporation. The interior of grain boundary is known to be less influenced by such factors. Many studies have been performed on the effect of GBs on charge transport and their influence on the device performance. Up to date, two distant results and conclusions have raised: (i) GBs play a benign role, promote charge separation and collection compared with grain interiors (GIs) and enhance the

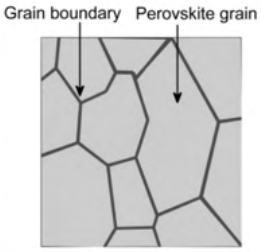

Figure 1.18: schematic of a typical top view of perovskite thin film illustrating different grains and grain boundaries. From Ref.[5].

overall charge transport (ii) GBs play a detrimental role, promote the non-radiative recombination and lower density of GBs are preferred to enhance charges transport. For example, in polycrystalline silicon, GBs are known to trap the majority carriers and to create mid-gap states within a bandgap that promote non-radiative recombination. The role that the grain boundaries play on charge transport in 3D perovskite is still matter of study. Experimental and theoretical results have shown that iodide vacancies can accumulate or be trapped at GBs. However it is not clear if GBs promote or not the ions movement within the crystal structure. Some research group have experimentally shown that number and density of grain boundaries influence the ions activation energy[21]. In particular these studies have proven that ion migration in polycrystalline $MAPbBr_3$ is reduced in the case of large grains. Other groups, through Kelvin probe force microscopy (KPFM) have demonstrated that charge potential barrier, like that depicted Fig.1.19, exists across the GBs in polycrystalline thin films and it could hamper the ions migration and enhance the charges transport at GBs. Depending on the polarity of ionic species, the barriers can be either positive (downward band bending) or negative (upward band bending).

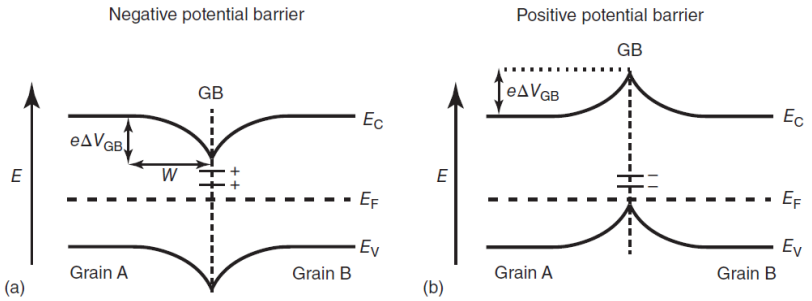

Figure 1.19: schematics of the electronic band diagram in the vicinity of GBs for (a) a negative and (b) a positive potential barrier. Defect states (arbitrary) at the GB are indicated by a sequence of small dashes. ΔV_{GB} and w denote potential barrier height and barrier width respectively. From Ref.[5].

1.4 Applications

High absorption coefficient, moderate mobility, long carrier diffusion length, direct and tunable band gap with simply halogen substitution and easy and low-cost process of fabrication make 3D perovskite the most promising materials for fabricating high efficiency solar cells. The performance of 3D perovskites solar cells (3D PSCs) has grown at incredible rate, reaching nowadays a value of power conversion efficiency (PCE) ($> 26\%$) which is almost comparable to those of commercially available solar cells technologies[27](Fig1.20). However 3D PSCs are not still ready for photovoltaic market because of some issues that limit their stability under real operative conditions. There are two main problems which affect the stability of 3D PSCs. The first is that 3D perovskites are more reactive to water and oxygen molecules in the atmosphere, leading to device instability and long term degradation when operated in air. The second is that ions move inside the lattice when the 3D PCSs is illuminated by sunlight leading to not only a degradation of PCS, but also to modification of device behaviour, contributing to the anomalous hysteresis observed in the current-voltage characteristics.

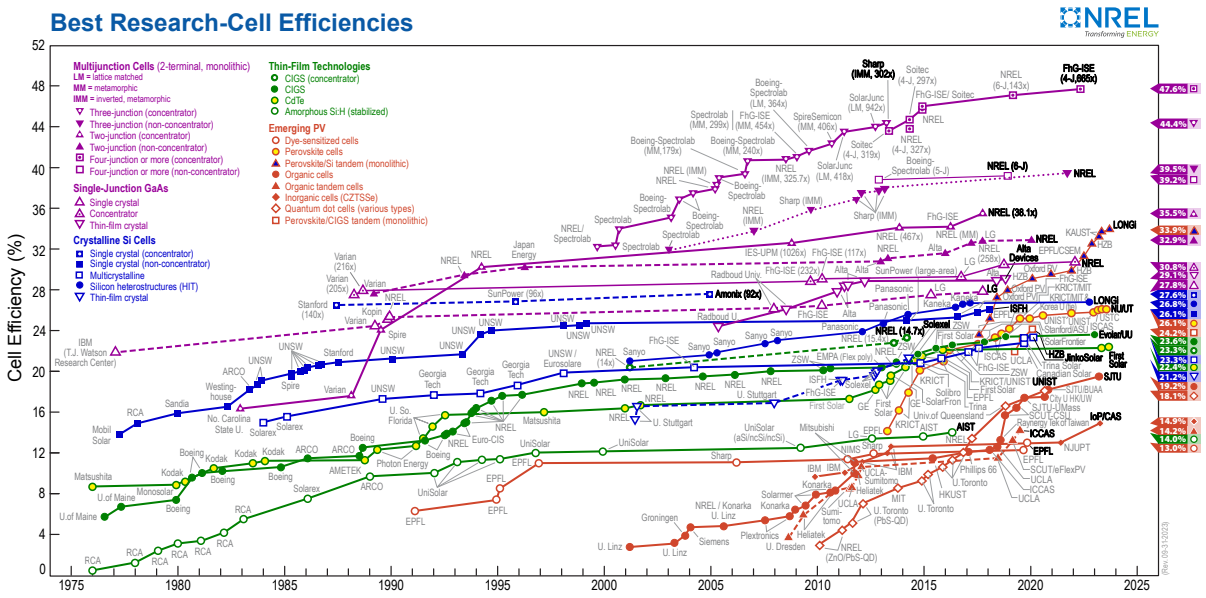

Figure 1.20: Chart of the highest confirmed conversion efficiencies for research cells for a range of photovoltaic technologies, plotted from 1976 to the present. From [27]

Recently the 2D perovskites, due to higher resistance moisture and substantially suppressed ions migration, have been considered as suitable candidate for PSCs. However the performance of 2D perovskite solar cells is still poor compared to 3D. This is mainly ascribable to strong quantum confinement at high number of layers which lead to broad band gap and so to low absorption in visible range. Combining low-dimensional per-

ovskites with 3D perovskites in layered 2D/3D composites has been proposed recently as the best strategy to overcome the PSC stability issues. The aim of this approach is to combine the high efficiency of 3D perovskites with the superior stability of 2D perovskites while maintaining the structural integrity of the two phases. The stability test have shown that this configuration has the same resistance to moisture of 2D perovskites, but compared to those the PCE do not depends strictly on the number of layers and is closed to 3D one(20%)[6][17][28][29]. As example, the group [28] have reported that the PCE of 2D/3D perovskite $MAPbI_3/(PEA)_2Pb_2I_4$ is 19.19% and that this value remains stable for 14 days at room temperature with 50% of humidity. Due to outstanding optoelectronic properties, the 3D perovskites have proven to be excellent active layers also in light emitting diodes, photodetectors, lasers, and radiations detectors. However the performance of these devices are limited by the same issues described for solar cells. Recently 2D/3D perovskites have been employed as active layer in X-ray detectors showing better performance compared to 3D one. For example, it was reported by a research group that $MAPbBr_3$ bases X-ray detectors show better stability and higher X-ray response after being treated with PEABr to form 2D/3D structure [18].

Chapter 2

Materials and Experimental Techniques

The first part of this chapter describes the synthesis of $MAPbBr_3$ polycrystalline thin films, the growth of $MAPbBr_3$ single crystals and the fabrication of 2D/3D $MAPbBr_3$. Then the experimental techniques (UV-Vis Spectroscopy, Florescence Spectroscopy, XRD, GIXRD), used to verify the formation of 2D perovskite after treating the 3D perovskite surface with one of 2D perovskite solutions (PEA+Toluene, PEA+IPA and PEABr+IPA), are presented. This entirely part was carried at Nèel Institute (CNRS), Grenoble (France), under the supervision of Dr.Thibault Lemercier. In the last part, the experimental methods (I-V, PICTS) used to study the charges transport and the defect states $MAPbBr_3$ polycrystalline thin films and single crystals after being treated with PEA+Toluene, are illustrated. This work was done entirely at the Department of Physics and Astronomy (DIFA) of University of Bologna(Italy).

2.1 Synthesis of 3D Perovskites

2.1.1 $MAPbBr_3$ Thin Films

The polycrystalline thin films (THFs) were obtained by spin-coating technique. A solution of 1.2 mol/L of $MAPbBr_3$ in DMSO (Dimethyl sulfoxide-CAS 67-68-5)-GBL (Gamma-Butyrolactone-CAS 96-48-0) in ratio 4:1 v, was spin-coated onto the clean glass substrate using as anti-solvent chlorobenzene. Fig.2.1 shows a THF obtained thorough this technique.

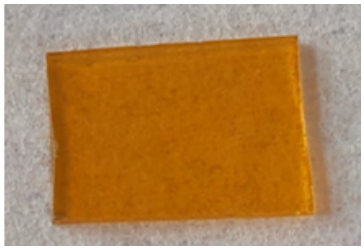

Figure 2.1: Image of a $MAPbBr_3$ thin film.

2.1.2 $MAPbBr_3$ Single Crystals

The experimental set-up, used for the growth of single crystals, is shown in Fig.2.2.

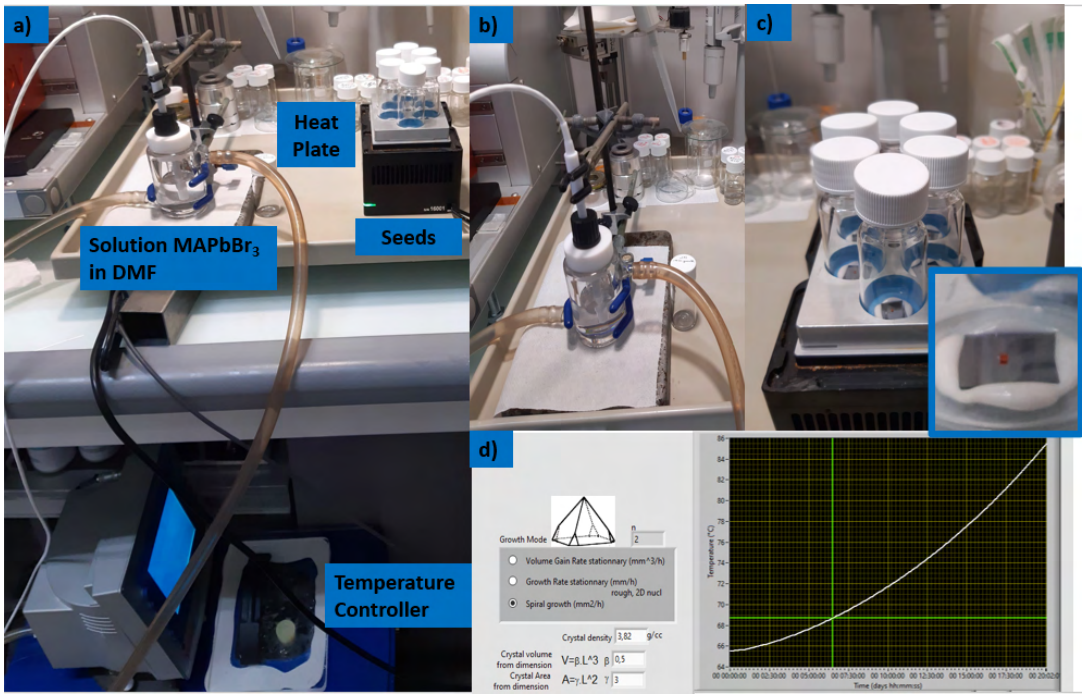

Figure 2.2: a) Set-up b) Vial containing $MAPbBr_3$ solution in DMF c) Heat plate used to single crystal growth. In zoom the $MAPbBr_3$ seeds placed on silicon wafer. d) Spiral growth for single crystal.

The starting point for crystal growth was a vial containing a concentration of 1 mol/L of $MAPbBr_3$ in DMF. The temperature inside it was setted at 57.3 °C and monitored through a temperature controller. At exact 57.3 °C, 3.5 ml of $MAPbBr_3$ in DMF was taken out using a micropipette and poured onto a vial containing the seed of $MAPbBr_3$ and placed on heat plate at 65.5 °C. The temperature of solution and heat plate were chosen in order to avoid formation of small crystals while the solution is poured on the

vial. The last step for growing single crystals consists on temperature ramp procedure. Through lab view interface a spiral growth was selected and starting from 65.5 °C the temperature of heat plate was brought at 85.5 °C in 20 hour through an exponential growth (Fig.2.2d). The small seeds of $MAPbBr_3$, used for growth, were obtained by a solution containing 1.1 mol/L of $MAPbBr_3$ in DMF and it was checked they do not have internal strain in order to guarantee an efficient crystal growth. Each seeds were glued using a CAF4 silicon glue on a silicon wafer(Fig.2.2d) in order to have a uniform well shaped single crystals.

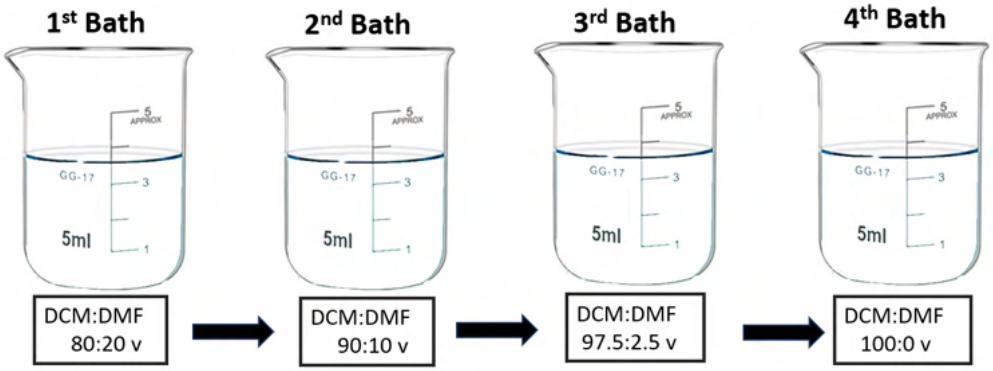

Figure 2.3: Passarelli treatment steps.

The seed of grown crystals was mechanically removed and the surface of each samples was cleaned through Passarelli treatment. This consists of four steps (Fig.2.3) in each of which the volume concentration of DMF is progressively reduced. Each single crystals are immersed for 10 second in a bath of DCM(Dichloromethane- CAS-75-09-2)-DMF(Dimethyl sulfoxide-CAS 67-68-5) and dried with Argon flow at pressure of 2 bar before to be put on the following. In Fig.2.4 a single crystal(SC), obtained though the procedure described before, is shown.

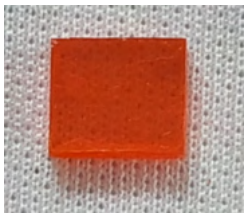

Figure 2.4: Image of a $MAPbBr_3$ single crystal.

2.2 Fabrication of 2D/3D Perovskites

In first part of this section, the synthesis of 2D ligand PEABr and the solvents and 2D ligands, used to prepare the 2D perovskites solutions, are described. This part was carried at Nèel Institute under the supervision of Dr.Julien Zaccaro. In the last part the procedure for the fabrication of 2D/3D perovskites are illustrated.

2.2.1 Synthesis of 2D Perovskite Solutions

To synthesize the PEABr, PEA(Phenethylamine-CAS 64-04-0) and HBr (Hydrobromic acid-CAS 233-109-9) react in a volumetric flask according to the reaction $PEA + HBr \longrightarrow PEA^+ + Br^-$. The volumetric flask was immersed in ice within a becker and the overall system (Fig.2.5a) was located on a magnetic stir plate, which helps to mix the two solutions. In this work 10 ml of PEA and 11.25 ml of HBr were used to form 16 g of powder of PEABr. Moreover during the procedure of solution mixing, it was added in sequence 0.5 mL of HBr until a basic solution of PEABr was obtained. The PH of final powder of PEABr was equal to 9 and it purity was estimated to be 100%. The powder obtained was dried by a rotavapor (Fig.2.5b) which was brought from a pressure of 240 mbar to 25 mbar in order to remove all residual water drops. Finally diethyl-ether (CAS 60297) was added and successively removed for four time in order to dry completely the powder.

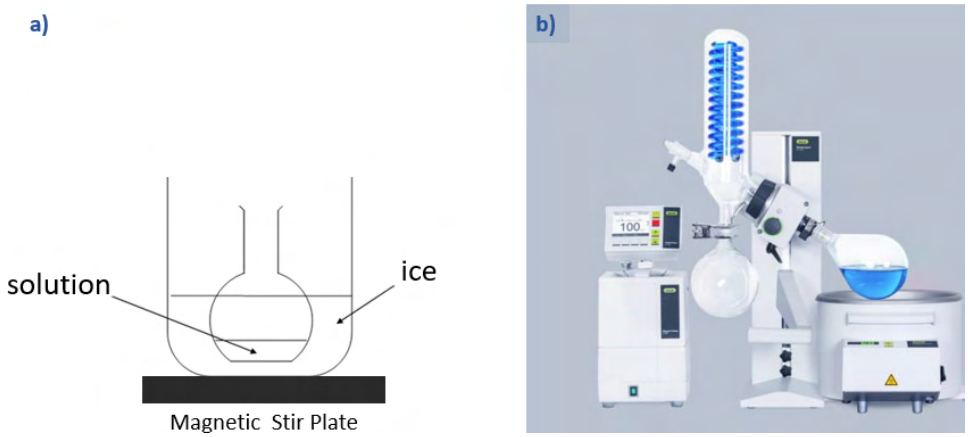

Figure 2.5: a) System used to produce the powder of PEABr b) Buchi Rotavapor used to dry it.

The 2D perovskite solutions used in this work to fabricate 2D/3D perovskites, are PEA+Toluene(PT), PEA+IPA(PI), PEABr+IPA(PBI) (2D ligand+solvent). This kind of 2D perovskite solutions were chosen because of polar crystal structure of 3D $MAPbBr_3$. All solutions were prepared inside a glove box in order to avoid environmental contamination. In table the values of PEA (Phenethylamine-CAS 64-04-0), PEABr, Toluene

(CAS-108-88-3), IPA (Isopropanol-CAS 67-63-0) used to prepare 20 ml of PT, PI and PBI solution are reported.

2D Perovskite solution	Concentration	2D Ligand	Solvent
PEA+Toluene(PT)	0.1 v%	0.02 mL PEA	19.98 mL Toluene
PEA+IPA(PI)	0.1 v%	0.02 mL PEA	19.98 mL IPA
PEABr+IPA(PBI)	1.6 mg/mL	0.04 g PEABr	18.96 mL IPA

Table 2.1: 2D ligands and solvents used to prepare 20 ml of PT, PI and PBI solution.

2.2.2 Fabrication of 2D/3D $MAPbBr_3$

The fabrication of 2D/3D perovskites comprises a sequence of steps which are illustrated in Fig.2.6 and can be listed as:

1st step: A 3D $MAPbBr_3$ sample is immersed in a 5 mL of one of 2D perovskite solutions for a given time;

2nd step: The sample is dipped in a few mL of toluene in order to remove the excess of treatment solution;

3rd step: The sample is immersed for 5 minute in a solution containing 40 mL of Toluene;

4th step: The sample is dried for 10 minute in hot plate at 100 °C.

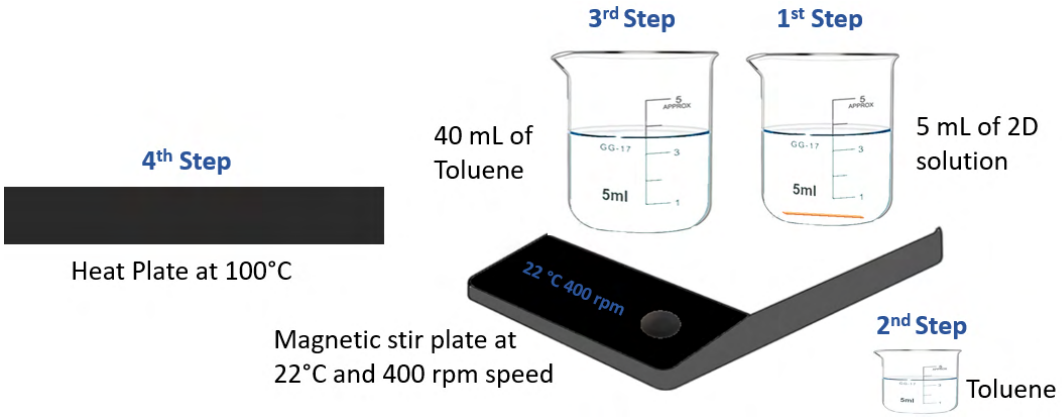

Figure 2.6: Steps for fabrication the 2D/3D perovskites.

In the first part of this work, in order to find the best treatment to fabricate the 2D/3D perovskites, only THFs were treated with one of the 2D perovskite solutions for

a time of reaction equal to 30 second (30″), 3 minute (3′) and 10 minute (10″). In the last part, to study the charges transport and defect states of 2D/3D perovskites with I-V and PICTS measurements, THFs and SCs were treated only with PT. The time of reaction was chosen equal to 15 second(15″), 1 minute (1′) and 10 minute (10′) for THFs, whereas for SCs 15 second(15″), 1 minute (1′). The list of treated samples studied in this work are reported in the table 2.2.

Name	Type	Treatment	time
THF_PT_15″	THF	PEA+Toluene	15 sec
THF_PT_30″	THF	PEA+Toluene	30 sec
THF_PT_1′	THF	PEA+Toluene	1 min
THF_PT_3′	THF	PEA+Toluene	3 min
THF_PT_10′	THF	PEA+Toluene	10 min
THF_PI_30″	THF	PEA+IPA	30 sec
THF_PI_3′	THF	PEA+IPA	3 min
THF_PI_10′	THF	PEA+IPA	10 min
THF_PBI_30″	THF	PEABr+IPA	30 sec
THF_PBI_3′	THF	PEABr+IPA	3 min
THF_PBI_10″	THF	PEABr+IPA	10 min
SC_PT_15″	SC	PEA+Toluene	15 sec
SC_PT_1′	SC	PEA+Toluene	1 min

Table 2.2: Samples treated with 2D perovskite solutions and analysed in this work.

2.3 Electrodes Deposition

In order to perform I-V and PICTS measurements, chromium electrodes were evaporated on surface of THFs and SCs treated with PT. As drawn in figure 2.7a the contacts geometry for SCs is top-bottom with top (30 nm) less ticker than bottom (90 nm), whereas for THF is coplanar and the thickness is 30 nm (Fig.2.7b). The electrodes were evaporated at speed of 0.1 nm/s, pressure of 10^{-6} mbar and temperature 100°C.

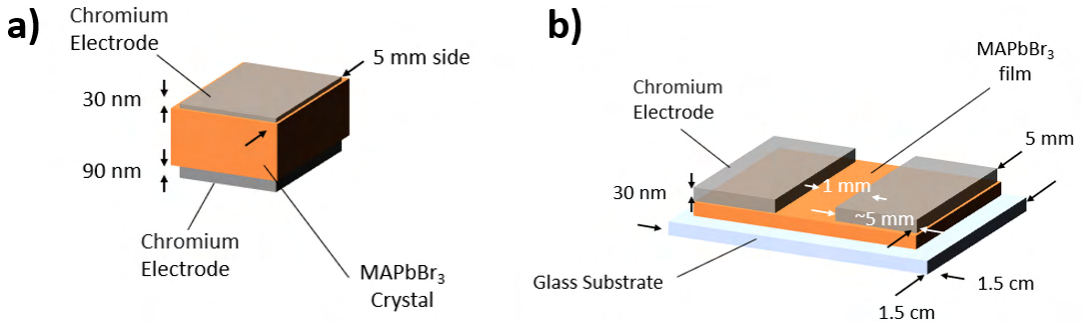

Figure 2.7: a) Top-Bottom electrode geometry for single crystal b) Co-planar electrode geometry for polycrystalline thin films.

2.4 UV-Vis Spectroscopy

In this thesis work, absorbance measurements were performed on THFs pristine and on THFs treated with one of the 2D perovskite solutions for a given time. To acquire absorbance spectra it was used a PerkinElmer Lambda 900 UV/VIS/NIR Spectrometer, which work principle is illustrated in Fig.2.8a. In Fig.2.8b the sample holder with an aperture of 3 mm used to perform absorbance measurements is shown together with the relationship between absorbance, incident and transmitted beam.

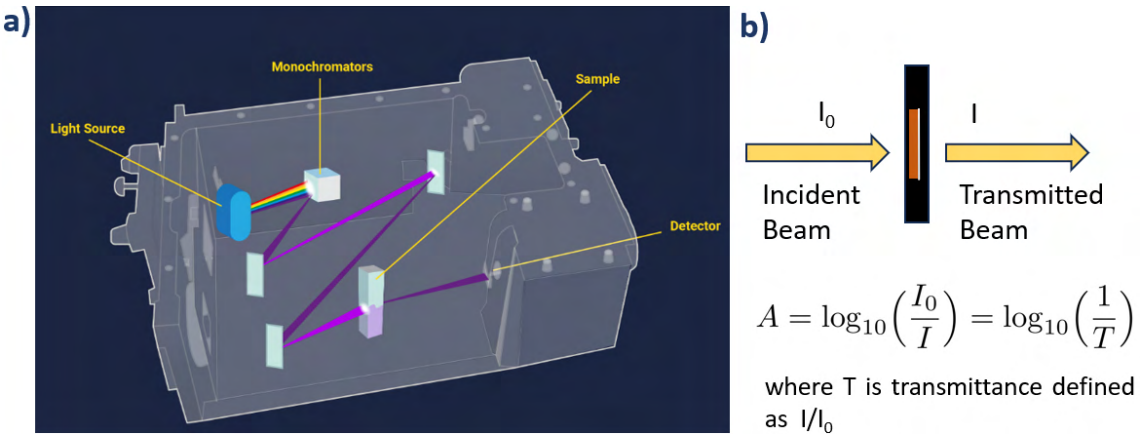

Figure 2.8: a) schematic diagram of UV-Vis spectroscopy system b) Sample holder used to perform absorbance measurements and relationship between absorbance, incident and transmitted beam.

In this work the absorbance spectra were acquired scanning wavelengths from 250 to 800 nm. This range was chosen because $MAPbBr_3$ and 2D perovskite have a maximum of absorbance respectively at the wavelength of around 500 nm and 400 nm.

2.5 Fluorescence Spectroscopy

The Photoluminescence (PL) spectra in steady state of THFs and SCs pristine and treated were acquired using the fluorometer Horiba Fluorolog-QM which is shown in Fig.2.9a.

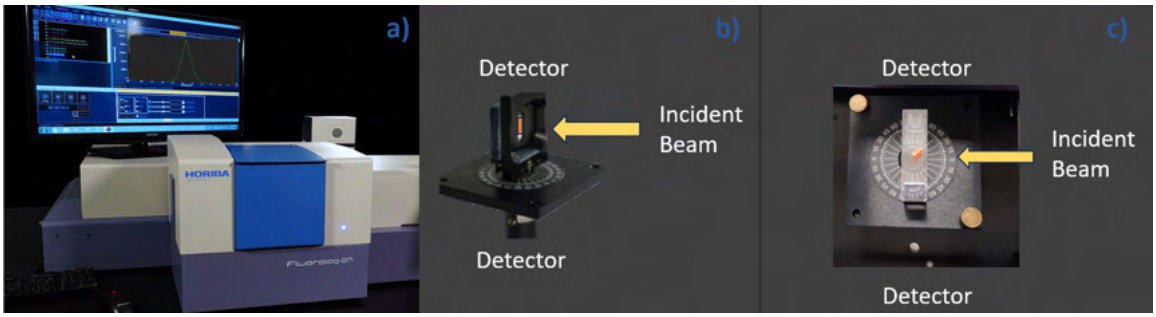

Figure 2.9: a) Horiba Fluorolog b-c) polycrystalline thin films and single crystals position with respect to impinging light and detector.

In this work, the fluorescence measurements of THF pristine and THF treated with one of the 2D perovskite solutions for a given time were performed placing a given sample inside a holder at 60° with respect to the incident light as shown in Fig.2.9b. The emission spectra of each sample, after being excited at wavelength of 360 nm, was recorded at wavelengths from 390 to 700 nm. The emission spectra was acquired in this range because the $MAPbBr_3$ and 2D perovskite have an emission spectrum respectively between 500 and 600 nm and between 400-450 nm. The emission slits were chosen of 2 mm aperture in order to increase the number of photons collected from the sample. The fluorescence measurements of SC pristine and SC treated with PT for 15″ and 1′, were performed placing a given sample upon two 10.00 mm quartz glass cuvette at 30° with respect to incident light exactly as shown in Fig.2.9c. This was done, because the quartz glass background has less influence on the acquired PL spectra compared to sample holder used to THFs. The emission spectra of SCs were acquired in the same spectral range and with the same excitation wavelength used for THFs. The aperture of emission slit was chosen equal to 4 mm in order to maximize the number of detected photons.

2.6 X-Ray Diffraction and Grazing Incidence X-ray Diffraction

The crystal structure of THFs pristine and THFs treated with one of the 2D solutions for a given time, and SCs, pristine and treated with PT for 15″ and 1′, was determined

through X-Ray diffraction (XRD) measurements using Bruker AXS D8 Advance diffractometer shown in Fig.2.10a.

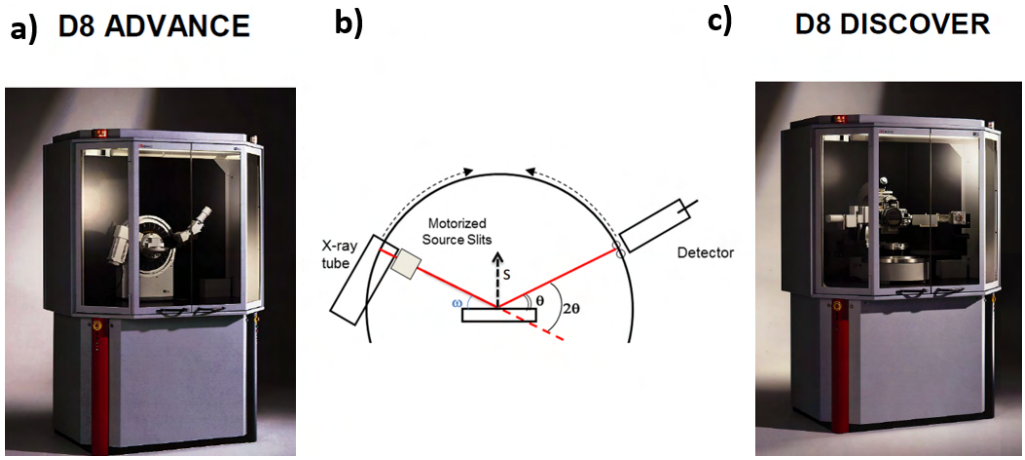

Figure 2.10: a) Bruker AXS D8 Advance used for XRD measurement b) Bragg-Brentano Geometry c) Bruker AXS D8 Discovery used for GIXRD measurement.

This diffractometer is equipped with a monochromator and it has Bragg-Bretano geometry as that shown in Fig.2.10b, which allows to have, compared to other geometries, high signal/noise ratio and high resolution of detected beam. In this work the X-rays, generated in the x-ray tube, before to impinges onto a given samples, are filtered by the monochromator at wavelength of CuK_α equal to 1.5418 Å. The X-ray diffracted beams were collected while the sample rotated at angle 2θ between 0° to 60°. The indexes of lattice plane of a given sample was determined using DIFFRAC.EVA software which allowed to compare the intensity peak detected at given angle with that reported in Crystallographic Open Database(COD). The COD 1545320 and 2224096 were used respectively for identifying the $MAPbBr_3$ and 2D perovskite diffraction peaks. In order to investigated the 2D crystal structure formed on the surface of 3D perovskite after the treatment, Grazing Incidence X-ray Diffraction (GIXRD) measurements were performed on THFs and SCs treated with PT respectively for 15″, 1′, 10′ and for 15″, 1′. The GIXRD measurements were acquired at incidence angle of 1° using the Bruker AXS D8 Discovery diffractometer shown in Fig.2.10b.

2.7 Current-Voltage Characterization

The optoelectronic characterization of THFs, pristine and treated with PT for 15″, 1′ and 10′, and SCs, pristine and treated with PT for 15″, 1′, was performed by acquiring in air and in vacuum the Current-Voltage (I-V) characteristics in dark and light. Moreover in

order to assess the ions contribution to electrical conductivity in such samples I-V measurements at different temperatures in vacuum were performed. All I-V characteristics were acquired using the experimental set-up shown in Fig.2.11.

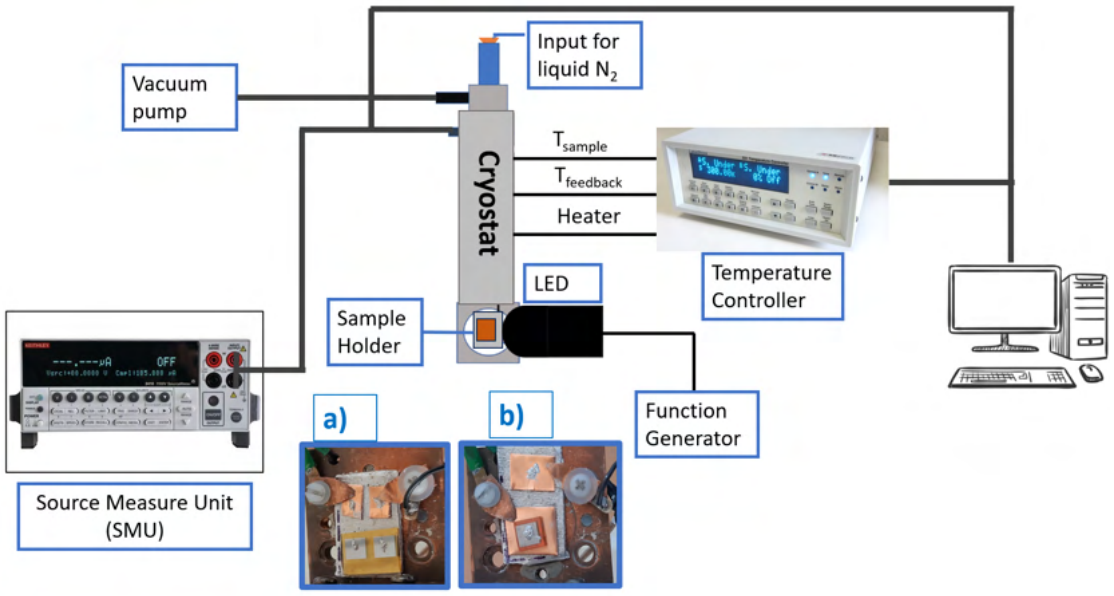

Figure 2.11: schematic representation of the experimental set-up for I-V measurements. a-b) Thin Film and Single Crystals placed on cold finger of cryostat.

In such experimental apparatus a given sample is mounted on the cold finger at the bottom of Janis VPF-800 cryostat. Two copper clamps are screwed on the electrical copper pads which bring electrical signal, through gold narrow wire, to chromium electrodes of THFs and to top electrode of single crystals. Two wires are soldered to the clamps and bring the electrical signal to BNC output at the top of the cryostat. In the case of THFs the contact on left is connected to the core of BNC whereas that in the right to shield of BNC. Instead in the SCs case the top contact is connected to BNC, whereas the bottom to shield of BNC. The KEITHLEY 2401 Source Measure Unit (SMU), connected to BNC output, measures a given current when a voltage is given by LabView software. In this work the I-V measurements were performed in a voltage range from -20V to 20 V. To acquire I-V in light, a given sample was illuminated by a LED with wavelength (475nm) above the band gap of the sample through a glass windows found at bottom of cryostat where the sample is placed. To turn on the LED during the I-V measurements, the GW Instek MFG-2110 function generator was used. This provides a square wave voltage signal to LED at frequency of 1MHz. To perform I-V at different temperatures, a given samples was put in vacuum through a rotary vacuum pump connected to the top of cryostat. This, which pumps around 10^{-4} mbar vacuum, simultaneously guarantees

a good thermal isolation from environment and avoids condensation when, at low temperature, liquid nitrogen (N_2) is poured inside the cryostat. In this work the I-V were acquired in a temperature range from 330K to 240K in order to avoid phase transition of 3D crystal lattice.

2.8 Photoinduced Current Transient Spectroscopy

In this work photoinduced current transient spectroscopy (PICTS) was used as technique to characterize defects of THFs and SCs pristine and treated with PT respectively for $15''$, $1'$, $10'$ and for $15''$, $1'$. In the following the working principle of PICTS and experimental set-up are presented.

2.8.1 Working Principle*

PICTS is an experimental technique which consists on measuring photocurrent transients as function of temperature. Compared to golden standard techniques for defects characterization, like DLTS (Deep-level transient spectroscopy), it does not require the construction of schottky or p-n junctions to extract the defect parameter such as activation energy and capture cross section. The fact that PICTS is not a capacitance based technique, make it particular suitable for high resistivity materials like hybrid perovskites, which was studied in this work, because for those materials it is experimental challenging build a schottky or p-n junctions. PICTS, like DLTS, is a rate-windows technique and in its classical picture consider only static shallow defect states like that depicted in Fig.2.12a-b. The PICTS experimental strategy for characterization of defect levels comprises a sequence of steps which are illustrated in Fig.2.12 a-c. First, starting from dark condition where the current is zero, a given device is illuminated under a fixed voltage through its transparent electrode with a near monochromatic light pulse of duration t_p and photon energy $h\nu > E_g$ where E_g is the band gap energy of materials (Fig.2.12a). In presence of volume of photogenerated, the defect levels present in the materials capture some of the photocarriers (Fig.2.12a). For a sufficient long t_p, a steady state is reached under illumination, with a constant photocurrent traversing the devices and a constant density of charge carriers populating the defect levels (Fig.2.12a-c). Once the light pulse ends, mobile carriers quickly recombine or drift out the device, leading to a rapid drop in overall current (Fig.2.12c). However, carriers populating the defect levels are thermally re-emitted into the respective bands at much slower rate thereby resulting in a long-lived current tails (Fig.2.12c in zoom). The current flowing through the device after the light pulse terminates provides a window on which it is possible determine the defects parameters. The current, which is thermally re-emitted from a defect, has an

*This section is entirely based on article [14] and [15]

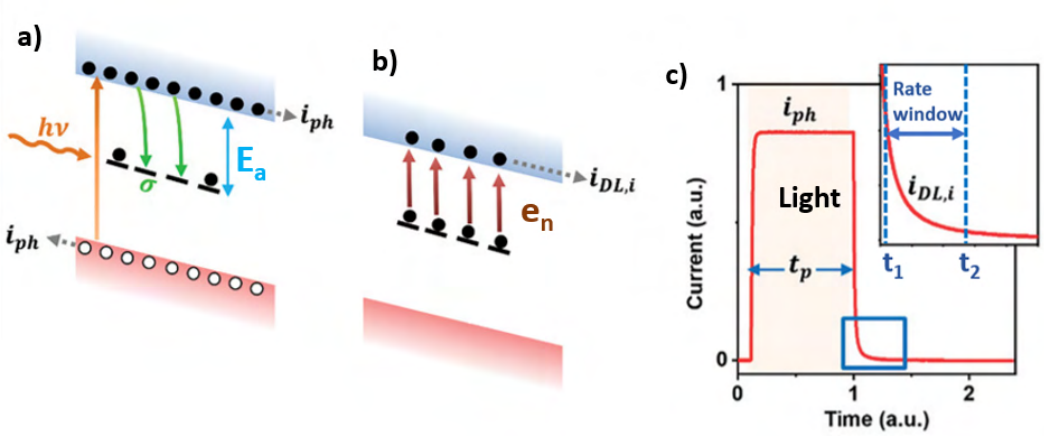

Figure 2.12: a) Defect-level filling during illumination in PICTS experiment. i_{ph}, σ, E_a refer to photocurrent, capture cross section and energy depth of a electronic defect level. b) Defect level emptying after the termination of a light pulse. $i_{DL,i}$ and e_n are defect-level emptying current and emission rate. c) Ideal Photocurrent transient t_p is the duration of light pulse.

exponential behaviour and it can be expressed by the following equation:

$$i_{DL,i} = eAE\mu_n\tau_n n_t \frac{1}{\tau} \exp\left(-\frac{t}{\tau}\right) \tag{2.1}$$

where e is the elementary electron charge, A is the device area, E is electric field that collects the current, μ_n and τ_n are the electron mobility and life-time, n_t is the density of occupied traps at any instant, τ is the decay rate of the current and depends on temperature. τ is linked to emission rate e_n of the defect level through the following Arrhenius equations:

$$\frac{1}{\tau} = e_n = \sigma v_n N_c \exp\left(-\frac{E_a}{k_b T}\right) \tag{2.2}$$

where σ is the capture cross section of defect level, v_n is average thermal velocity of free electrons, N_c is the effective density of states in the conduction band, E_a is the activation energy, which is the energy difference between the defect state and the conduction band, k_b is Boltzmann constant, T is absolute temperature. In the previous equation, the thermal velocity v_n of free electrons and the effective density of state N_c in the conduction band can be write in function of temperature as:

$$v_n = \sqrt{3k_b T/m^*} \tag{2.3}$$

$$N_c = 2M_c\left(\frac{2\pi m^* k_b T}{h^2}\right)^{3/2} \tag{2.4}$$

where m*, M_c, h are electron effective mass, the number of conduction band minima and Planck constant. Substituting the equations 2.3 and 2.4 in equation 2.2, we find the following equation:

$$\ln\left(\frac{T^2}{e_n}\right) = \gamma\sigma + \frac{E_a}{k_b T} \tag{2.5}$$

where $\gamma = 2\sqrt{3}M_c(2\pi)^{2/3}k^2m^*h^{-3}$ is a constant.
The equation 2.5 is fundamental for defect characterization. Indeed plotting the experimental data of the emission rate as $\ln(T^2/e_n)$ vs 1/T (Arrhenius plot) a straight line is found from which through a linear fit, using the equation 2.5, the activation energy E_a and capture cross section σ of a defect states are calculated as slope and intercept. In PICTS analysis to characterized the defect state it is important to determine the straight line of Arrhenius plot, called trap signature, rather than E_a and σ because it allows to classified the kind of defect state and compare it with trap signature reported in literature. To build the Arrhenius plot the emission rate as function of temperature must be determined. To do so, a double gate rate windows method is used for PICTS analysis. It consists on choosing two instant times t_1 and t_2, as in figure 2.12c, called gate, which defines a rate widows of duration t_1-t_2. The PICTS signal for a given rate window is defined as current at time t_1 and t_2, calculated in function of temperature: $\Delta i(T)=i(t_1,T)-i(t_2,T)$. The PICTS spectra is found by plotting such PICTS signal as function of temperature. A generic PICTS (Fig.2.13) spectrum presents a peaks for each distinct defect levels, which are parametrized with respect to the rate windows e^* represented in figure with colour bar. The i-th peak of such spectrum is maximum at a given temperature T_M at which the associated defect level has an emission rate equal to the rate window: $e(T_M) = e^*$. By tracking the position of a given peak for different rate window values, the emission rate of the corresponding defect level as a function of temperature e(T) is determined allowing to build the Arrhenius plot.

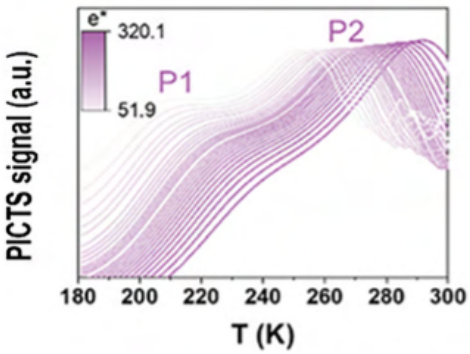

Figure 2.13: PICTS map example. P1 and P2 peaks corresponds to two distinct defect levels.

The PICTS physical model described above considers only the case of static defects of an

electronic nature which is not the case of samples studied in this work. To characterize the defects of $MAPbBr_3$ it is necessary to adapt PICTS model to the case of ionic defects which move in response to external stimuli such as voltage or light. In the following, the PICTS model, which, keeping the same backbone of classical PICTS to analysed the data, allows to interpreter the PICTS photocurrent transients in term of ions migrations, is illustrated. The band structure diagram of $MAPbBr_3$ can be represented as the metal-perovskite heterojunctions.

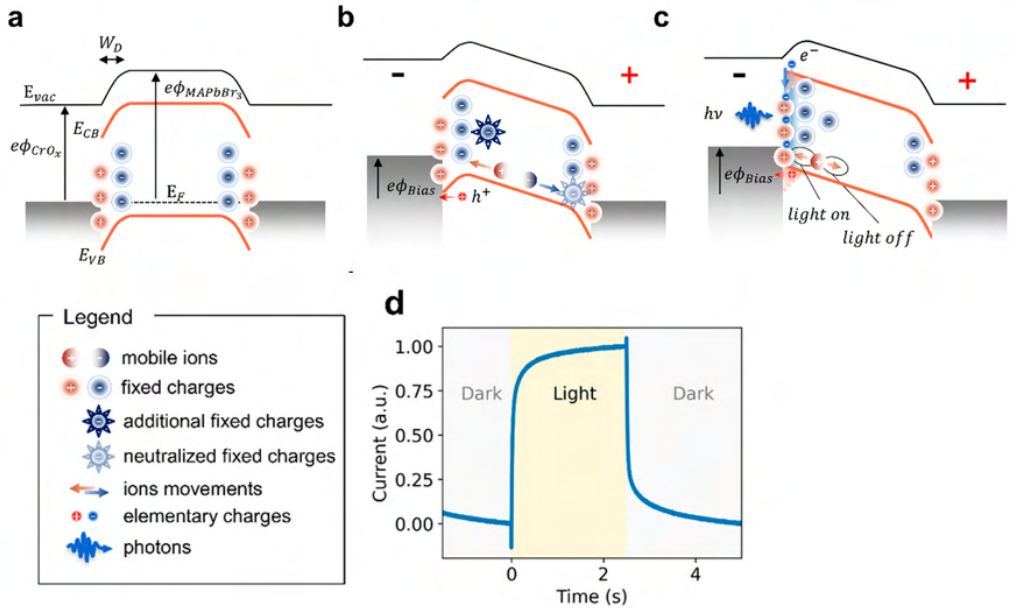

Figure 2.14: (a–c) Photocurrent model to describe transient photocurrent in $MAPbBr_3$ where ions dominate the charge transport. E_{vac} is vacuum level energy, ϕ is work function, W_D is the depletion layer, E_F is Fermi Energy, E_{VB} and E_{CB} are conduction and valence band edges. (d) Experimental photocurrent transient at room temperature.

In dark and at zero bias (figure 2.14a) the valence (VB) and conduction (CB) bands bend downward due to accumulation of fixed positive charges (ions) at metal-perovskite interfaces. This downward band bending causes a negative space charged region (scR) at perovskite-metal electrode interface. When a negative voltage it is applied, as in the case of samples treated in this work, holes and positive ions move towards the semi-transparent negative contact, whereas electrons and ions towards the positive one. After applying a negative voltage (figure 2.14b), only elementary charge (holes and electrons) are collected at negative or positive electrode, whereas ions accumulated at perovskite-metal interfaces enlarging the band bending. When above band gap photons impinging on perovskite-metal interfaces (Fig.2.14c) induced electron-holes pairs are created in few hundred nanometres inside the perovskite layer. Due to the downward band bending, photogenerated electrons initially are not collected at positive electrode, but they are

confined at negative electrode interface where they get trapped by the fixed positive ions. The negative charge of this localized electrons is screened by holes attracted by external circuit to negative contact. This movements of holes toward positive electrode gives rise to reverse current spike (RCS). Subsequently the photogenerated electrons are able to compensate and neutralize the fixed ions. This allows to flatten the band so that they can move towards the positive electrode. But also the ions, when the light is turn, can move toward the negative electrode and modifying the band bending. At given time, the light it is turn off and the electron trapped by ions are thermally realized. This give us a window to characterized the defects as in PICTS classical model. This de-trapped electrons recombine with holes that move in opposite direction. This movement of holes yields to arise again a RCS signals. Now the mobile positive ions are no more neutralized and they go back to the downward banding condition. Due to this local change of band, the mobile ions can return back as at initial condition (dark and no applied voltage). To summarize, under negative bias, the light, generating the photoinduced carriers, induce a change in band banding and the ions can migrated. When light it is turn off, the ions turn back to their initial position, recovering the starting band configuration. Fig.2.14d the photocurrent transient in the case of ions migration is shown. Compare photocurrent signal of classical PICTS model(Fig.2.13c) this photocurrent signal shows a asymmetry in rise and fall time of photocurrent which it is typical of signal due to slow particles(ions).

2.8.2 Experimental Set-up

The experimental set-up used to perform PICTS measurements is shown in Fig.2.15. As in set-up for I-V measurements, a given sample is mounted on the cold finger at the bottom of Janis VPF-800 cryostat. Two copper clamps are screwed on the electrical copper pads which bring electrical signal, through gold narrow wire, to chromium electrodes of polycrystalline thin films and to top electrode of single crystals. Two wires are soldered to the clamps and bring the electrical signal to BNC output at the top of the cryostat. In the case of THFs the contact on left is connected to the core of BNC whereas that in the right to shield of BNC. Instead in the SCs case the top contact is connected to BNC, whereas the bottom to shield og BNC. A Femento DLPCA-200 current amplifier is connected to BNC output. This allows to bias the sample with a voltage equal to -5V and to amplify the output current. For THFs in order to enhance the noise-signal ratio of the photocurrent, the current amplifier was set in low noise range (L) with a transimpedance gain of 10^8 and it was considered all bandwidth (FBW). For SCs, the same configuration for current amplifier was chosen, but with a gain of 10^6. The output signal of current amplifier is connected through BNC cable with National Instrument PCI-6013 digital acquisition board (DAQ) mounted inside a PC. The LabView PICTS softwer connected to DAQ allows to set the parameter for acquisition data. A LED with wavelength (475nm) above the band gap of the sample was used to illuminate the

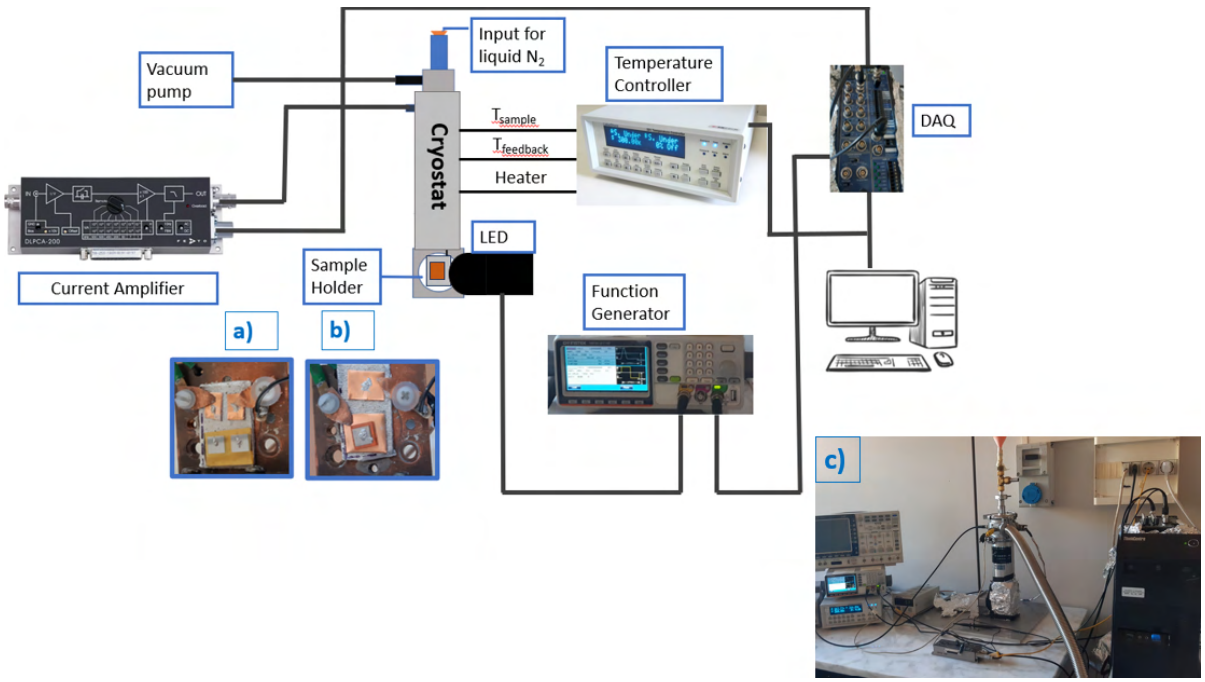

Figure 2.15: schematic representation of the experimental set-up for PICTS measurements. a-b) Thin Film and Single Crystals placed on cold finger of cryostat c) Picture of PICTS set-up.

sample through a glass windows found at bottom of cryostat where the sample is placed. A GW Instek MFG-2110 function generator provides a square wave voltage signal to LED, turning it on and off with configurable frequency and duty cycle. The frequency was equal to 300 Hz for THFs whereas 0.2 Hz for SCs. A square wave reference signal with same frequency is sent to the DAQ as trigger. The light intensity of LED was 3 mW/cm^2. The photocurrent transients for both THFs and SCs were acquired in a temperature range from 330K to 240K in order to avoid phase transition of 3D $MAPbBr_3$ crystal lattice. To perform such measurements the sample was put in vacuum using a rotary vacuum pump connected to the top of cryostat. This, which pumps around 10^{-4} mbar vacuum, simultaneously guarantee a good thermal isolation from environments and avoids condensation when, at low temperature, liquid nitrogen (N_2) is poured inside the cryostat.

Chapter 3

Experimental Results

In the first part of this chapter, the characteristics of $MAPbBr_3$ polycrystalline thin films and single crystals are presented. In the second part, the analysis, which was conducted to verify the formation of 2D/3D structure after treating the polycrystalline thin films with one of the 2D perovskite solutions for a given time of reaction, is illustrated. This activity was carried out at Nèel Institute (CNRS), Grenoble, France. In the last part, the analysis, performed on the charges transport and defect states of polycrystalline thin films and single crystals after being treated with PEA+Toluene, is presented. This activity was done at the Department of Physics and Astronomy (DIFA) of University of Bologna.

3.1 Characterization of 3D Perovskites

3.1.1 $MAPbBr_3$ Thin Films

The surface morphology of $MAPbBr_3$ THFs was analysed through the acquisition of optical microscope and S.E.M images (opt and S.E.M micrographs)*. The opt and S.E.M micrographs of a THF studied in this work are shown in Fig.3.1. The opt micrograph presents the typical rings of THFs obtained through spin coating techniques which use as anti-solvent the chlorobenzene. The S.E.M micrograph shows the grain boundaries of THF and a morphology which resembles that of THFs obtained by spin coating techniques. To determine at which wavelength λ_{abs} the THF absorbs photons, absorbance measurements were performed. Fig.3.2 shows the absorbance spectrum of a THF studied in this work, and from which it was possible to estimate roughly λ_{abs} equal to 520 nm. To determine the exactly λ_{abs}, the optical band gap was determined by plotting $(\alpha * E)^2$ against the photon energy (Fig.3.3). The x-axis intersection point of the linear fit of such

*In this work Nikon Eclipse Lv 100 ND optical microscope and Zeiss Gemini S.E.M ultraplus were used.

plot, allowed to determine the optical band gap E_{opt} equal to 2.30 eV and λ_{abs} equal to 537 nm. The y axis of such graph was calculated in the following way. First from the absorbance measurement the absorption coefficient, using the Beer-Lambert law, was calculated as:

$$\alpha = \frac{(\ln(10) * A)}{t} \tag{3.1}$$

where A is the absorbance and t is the thickness of THF equal to 300 nm. Then this value was multiplied by the photon energy E and elevated to a coefficient γ that in case of direct gap semiconductor is equal to 2 [16]. Fig.3.4 shows the PL spectrum, normalized to one, from which the energy band gap E_g was determined as PL peak. E_g value found is equal to (2.30 ± 0.01)eV and it is almost compatible with that reported in literature for $MAPbBr_3$ THFs [5]. The THFs studied in this work shows a value of E_{opt} closed to E_g. This is ascribable to low exciton binding energy in $MAPbBr_3$ which allows to created free charges, after the photon absorption, which recombine emitting a photon with the same wavelength of absorbed one[7]. The XRD spectrum, shown in Fig.3.5, corresponds to the one cubic crystalline structure of $MAPbBr_3$ reported in literature [5]. In particular, from XRD measurements it was possible to detect not only the lattice plane indexes of cube face ((100), (200), (300)) but also the diagonal ((110), (210), (220)) of cubic crystal unit. The detection of diagonal lattice indexes give the orientation of single crystals which THF is made and which are tilted with respect to substrate.

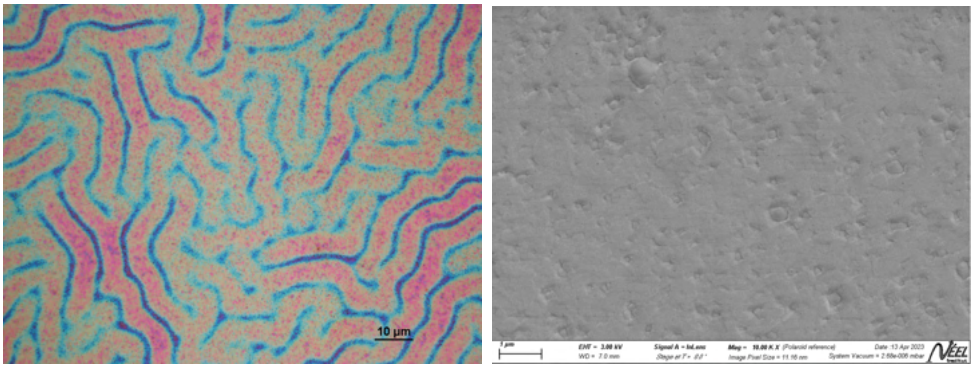

(a) optical microscope image (b) S.E.M

Figure 3.1: a) Optical microscope image b) S.E.M image of THF.

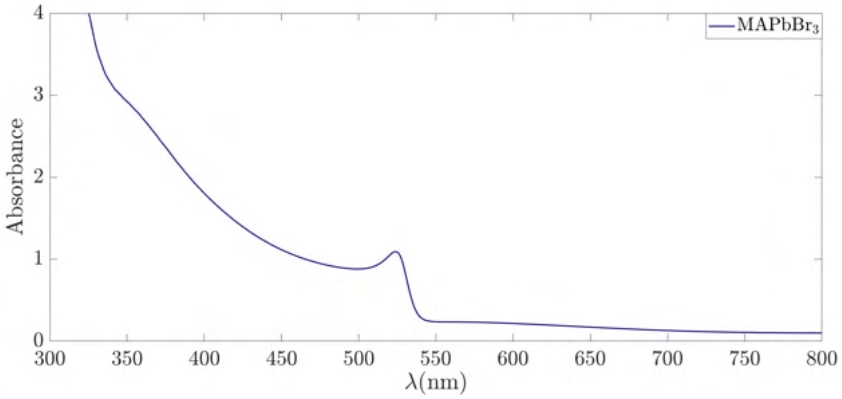

Figure 3.2: Absorbance spectrum of $MAPbBr_3$ THF.

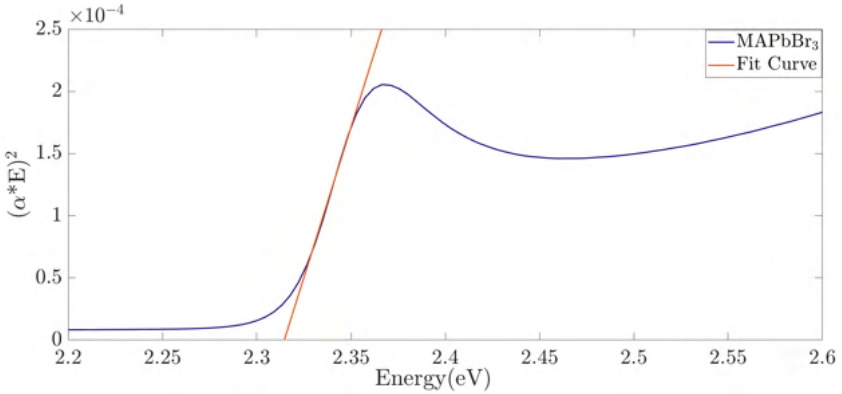

Figure 3.3: Determination of optical band gap of $MAPbBr_3$ THF.

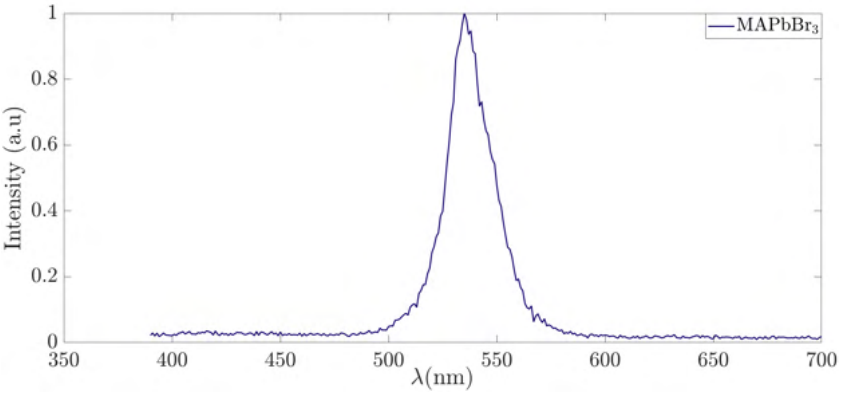

Figure 3.4: PL spectrum of $MAPbBr_3$ THF.

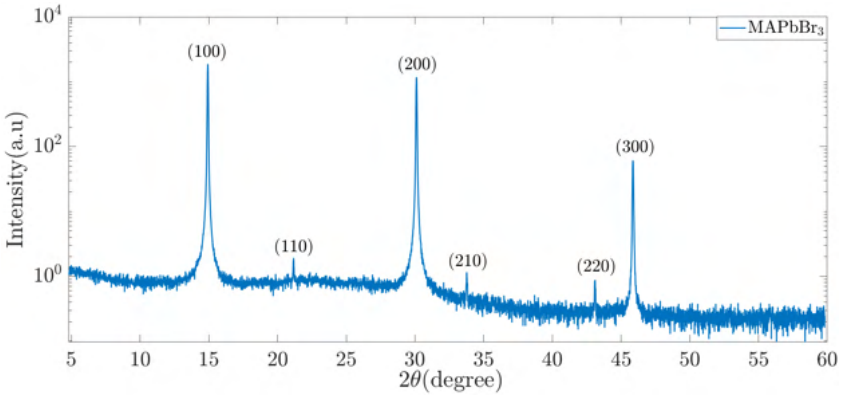

Figure 3.5: XRD spectrum of $MAPbBr_3$ THF.

3.1.2 $MAPbBr_3$ Single Crystals

Fig.3.6 shows the opt micrographs of the top and bottom surface of a $MAPbBr_3$ SC studied in this work. The bottom surface resembles that cleaned with Passarelli treatment after mechanically removal of seed. In this work SCs were characterized by PL and XRD measurements. In Fig.3.7 the PL spectrum normalized to one of a SC is shown. On the right side of PL spectra there is a small peak which it is observed in all single crystals and which nature is doubtful. Its origin may be due to background noise. E_g calculated as PL energy peak is equal to 2.27 ± 0.01eV and it is closed to that THFs. The XRD spectrum (Fig.3.8) shows diffraction peaks which corresponds to lattice plane indexes of face of cubic unit cell of $MAPbBr_3$.

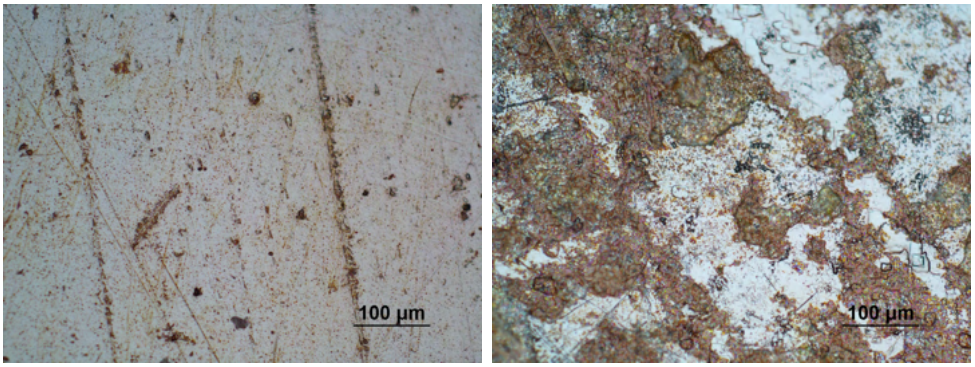

(a) Top surface (b) Bottom surface

Figure 3.6: optical microscope images of SC: a) top surface b) bottom surface.

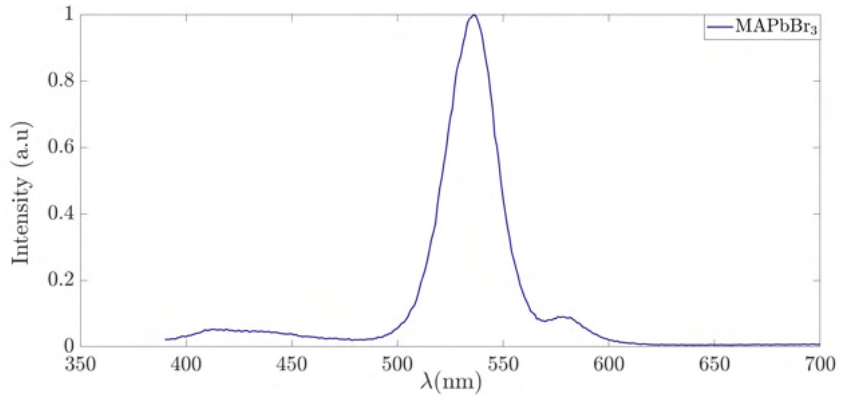

Figure 3.7: PL spectrum of $MAPbBr_3$ SC.

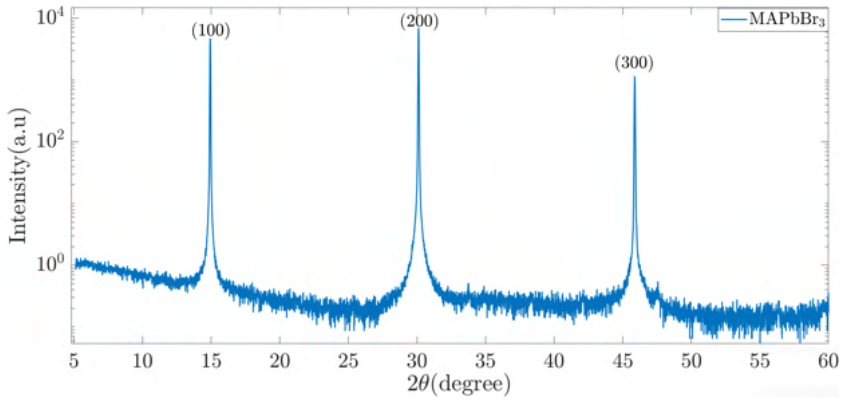

Figure 3.8: XRD spectrum of $MAPbBr_3$ SC.

3.2 Analysis on the Fabrication of 2D/3D Perovskite

One of the purpose of this work thesis is to find the best process to fabricate 2D/3D perovskite structure. In the following, the results, obtained treating the surface of $MAPbBr_3$ THFs with three different 2D perovskite solutions PEA+Toluene(PT), PEA+IPA(PI), PEABr+IPA(PBI) for three reaction times, 30 second (30″), 3 minute (3′) and 10 minute (10′), are reported. To verify the eventual changes on surface morphology of 3D perovskite and the crystallization of 2D perovskite on 3D surface, the opt and S.E.M micrographs of THFs before (THF pristine) and after the treatment with one of the 2D perovskite solution for a given reaction time, were acquired. The absorbance, fluorescence and XRD measurements are used to verify the formation of the 2D perovskite on 3D surface after the treatment.

The images of THFs after being treated with PT, PI and PBI for a time equal to 30″, 3′ and 10′ is shown in Fig.3.9.

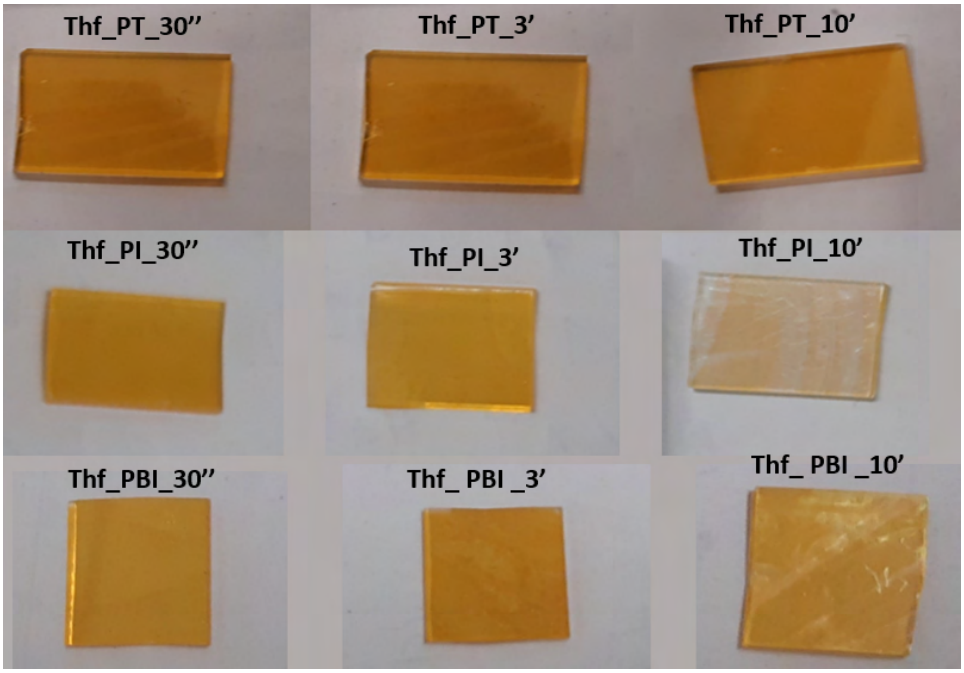

Figure 3.9: Images of THFs after the treatment with PT, PI and PBI.

The colour of THFs treated with PT is the same of THF pristine (Fig.2.1) which means that PT does not degrade the 3D structure. The opt and S.E.M micrographs, absorbance, PL and XRD spectra on THFs treated with PT show that:

(i) The time of treatment 30″ is too short to produce the 2D/3D perovskite structure. In particular the opt and S.E.M micrographs (Fig.3.10a and Fig.3.13a) show the same morphology of THF pristine (Fig.3.1a). The absorbance and PL spectra (Fig.3.16 and Fig.3.19) present only the 3D absorbance peak. The XRD (Fig.3.22) spectrum shows only the diffraction peaks of 3D perovskite.

(ii) The time of treatment 3′ is enough to produce the 2D/3D perovskite. In particular a 2D perovskite with layer n=1 was formed on 3D surface. The S.E.M micrograph (Fig.3.13b) shows the crystallization of 2D perovskite on the surface of 3D. In particular, the 2D perovskite, which is white in the image in contrast to the grey of 3D surface, was formed not only around the grain boundaries of THF, but also in the interior. The absorbance spectrum (Fig.3.16) does not show the 2D absorbance peak, but the PL spectrum (Fig.3.19) shows the 2D PL peak which corresponds to a 2D perovskite with layer n=1. The non detection of 2D absorbance peak may be due to too thin 2D perovskite to be measured by UV-Vis spectrometer. The XRD

spectrum (Fig.3.22) shows the diffraction peaks of 2D perovskite with layer n=1 and those of 3D perovskite.

(ii) The time of treatment 10′ is enough to produce the 2D/3D. In particular a 2D perovskite with layer n=1 and n=2 was formed on 3D surface. The opt and S.E.M micrographs (Fig.3.10c and Fig.3.13c) show that the morphology of the surface is completely changed compared to THF pristine (Fig.3.1a). The absorbance spectrum (Fig.3.16) shows a pronounced 2D absorbance peak which corresponds to a 2D perovskite with layers n=1, other 3D one. The PL spectrum (Fig.3.19) presents 2D PL peaks which correspond to 2D perovskite with layers n=1 and n=2. The XRD spectrum (Fig.3.22) shows the diffraction peaks of 2D perovskite with n=1 and those of 3D perovskite. The no detection of 2D perovskite diffraction peak with n=2, it may due that it forms only on 2D surface and not to the bulk, where the sensibility of XRD instrument is low.

The colour of THFs treated with PI changes significantly compared to THF pristine (Fig.2.1). In particular THF_PI_10′ has almost white colour, which means that the time of treatment 10′ has degraded completely the 3D perovskite. The opt and S.E.M micrographs, absorbance, PI and XRD spectra on THFs treated with PT show that:

(i) The time of treatment 30″ and 3′ produce a degradation of 3D perovskite crystal structure and not the formation 2D/3D structure. The XRD spectra of THF_PI_-3′ and THF_PI_10′ (Fig.3.23) show diffraction peak of $PbBr_2$. This means that after the treatment with PI the 3D structure collapses onto 0D one. The detection of $PbBr_2$ diffraction peak, allows to interpreter the white dots on the surface of THF_PI_3′ and THF_PI_10′ in the S.E.M micrographs (Fig.s 3.14a and 3.14b) as traces of $PbBr_2$.

(ii) The time of treatment 10′ is enough not only to degrade the 3D perovskite, but also to partially remove the THF from glass substrate. The almost white image of THF after the treatment shows the partial removal of THF from glass substrate. This in turn justified the flat morphology and the absence of grain boundaries of THF_PI_10′ S.E.M micrograph which may due to partially acquisition of glass S.E.M micrograph.

The colour of THFs treated with PBI looks more yellow compared to THF pristine (Fig.2.1). This means that there is probably an excess of PbBr in the crystal structure of THF after the treatment with PBI[20]. The opt and S.E.M micrographs, absorbance, PL and XRD spectra on THFs treated with PBI show that:

(i) The time of treatment 30″ is too short to produce the 2D/3D perovskite structure. In particular the opt and S.E.M micrographs (Fig.s 3.12a and 3.15a) show the same morphology of THF pristine (Fig.3.1a). The absorbance and PL spectra (Fig.3.18

and Fig.3.21) present only the 3D absorbance peak. The XRD (Fig.3.24) spectrum shows only the diffraction peaks of 3D perovskite.

(ii) The time of treatment $3'$ and $10'$ are enough to produce the 2D/3D. In particular a 2D perovskite with a thinner layer n=1 forms after the treatment with PBI. The opt and S.E.M micrograph of THF_PBI_$3'$ and THF_PBI_$10'$(Fig.s 3.12b, 3.12c and Fig.s 3.15b, 3.15c) do not show significant change compared to THF pristine (Fig. 3.1a) and they are similar each others. In particular S.E.M micrographs do not show 2D perovskite crystallization on 3D surface like those treated with PT. The absorbance spectra of THF_PBI_$3'$ and THF_PBI_$10'$ (Fig.3.18) do not show the 2D absorbance peak, but the PL spectra (Fig.3.21) present the 2D PL peak which corresponds to 2D perovskite with n=1. The XRD spectra of THF_PBI_$3'$ and THF_PBI_$10'$ show the diffraction peaks of 2D perovskite small and broad compared to that of XRD spectra of THFs treated with PT. This means that the 2D perovskite is not well crystallized on 3D surface.

In conclusion, the analysis of 2D/3D perovskite fabrication has shown that the process to produce a 2D/3D perovskite with well crystallized and stable 2D perovskite on 3D surface is obtained by treating THFs with PT. In particular only the time of treatment $3'$ and $10'$ allowed to fabricate a 2D/3D perovskite with 2D perovskite respectively with n=1 and n=1 and n=2, whereas that $30''$ leaves unchanged the 3D perovskite structure.

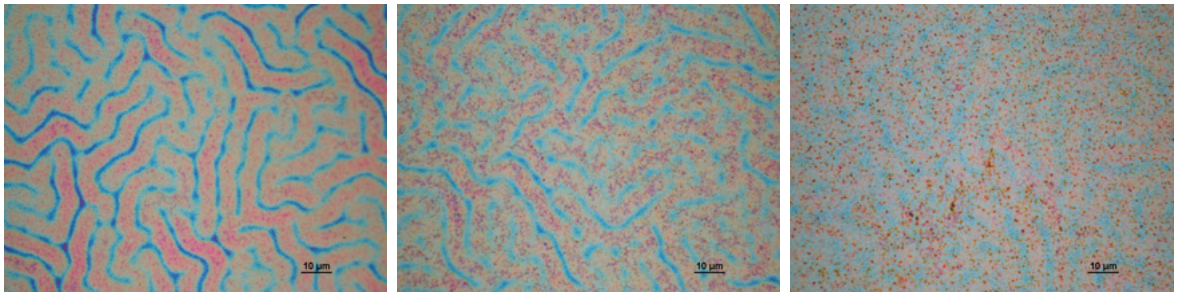

(a) THF_PT_30″ (b) THF_PT_3′ (c) THF_PT_10′

Figure 3.10: Optical microscope images of THFs after treatment with PT.

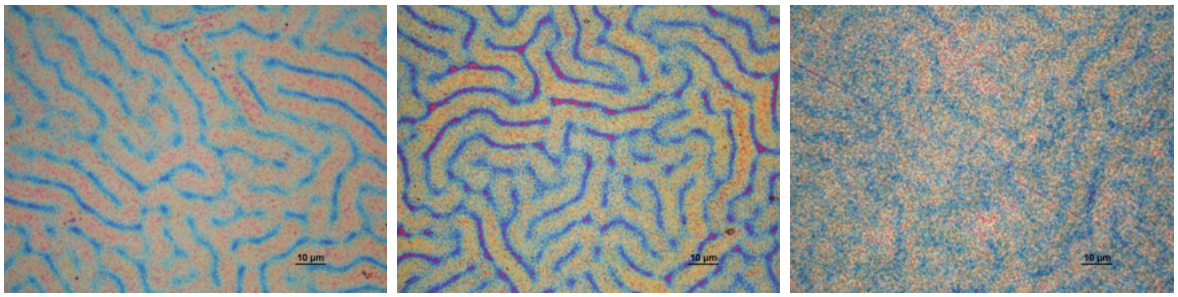

(a) THF_PI_30″ (b) THF_PI_3′ (c) THF_PI_10′

Figure 3.11: Optical microscope images of THFs after treatment with PI.

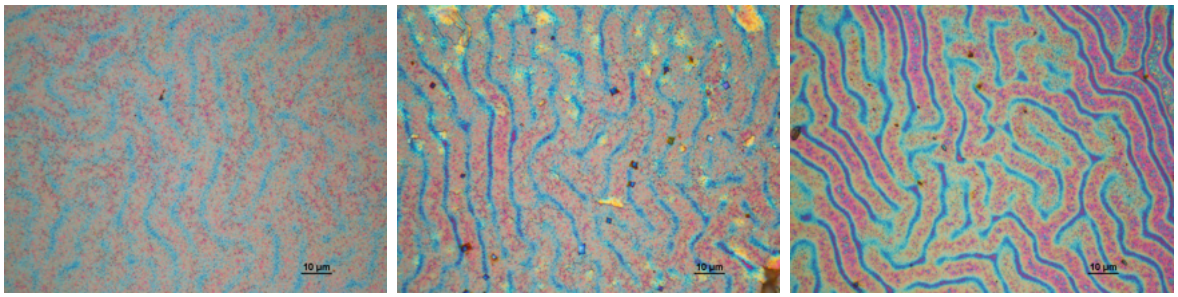

(a) THF_PBI_30″ (b) THF_PBI_3′ (c) THF_PBI_10″

Figure 3.12: Optical microscope images of THFs after treatment with PBI.

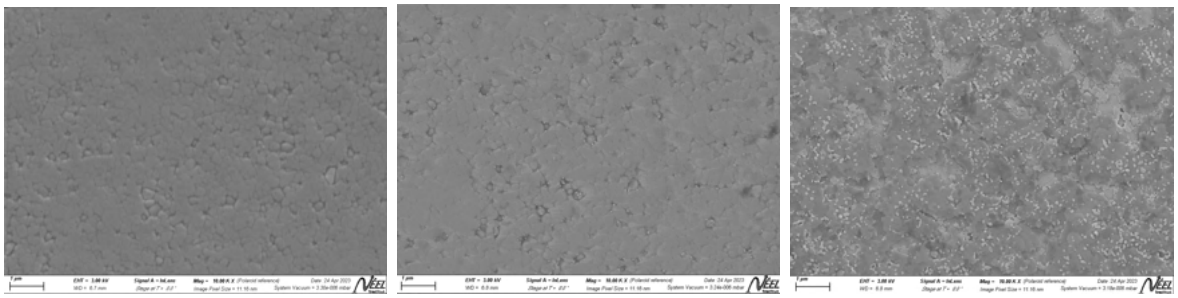

(a) THF_PT_30″ (b) THF_PT_3′ (c) THF_PT_10′

Figure 3.13: S.E.M images of THFs after treatment with PT.

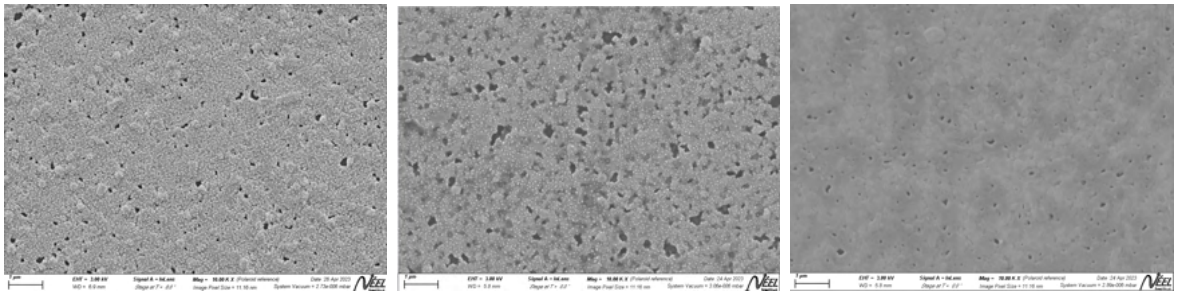

(a) THF_PI_30″ (b) THF_PI_3′ (c) THF_PI_10′

Figure 3.14: S.E.M images of THFs after treatment with PI.

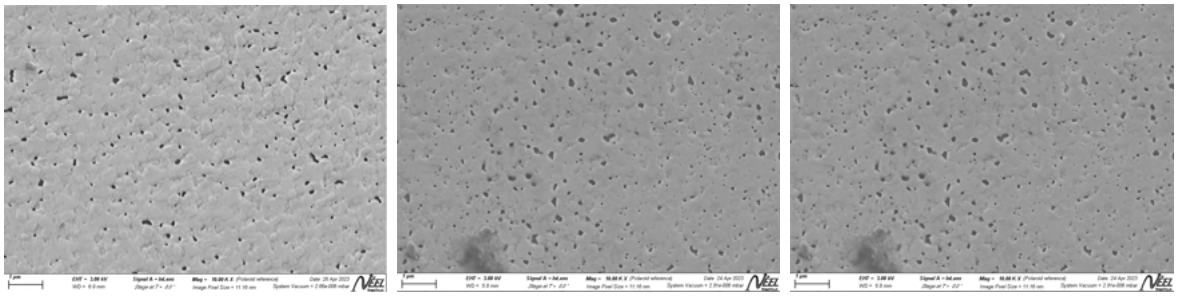

(a) THF_PBI_30″ (b) THF_PBI_3′ (c) THF_PBI_10′

Figure 3.15: S.E.M images of THFs after treatment with PBI.

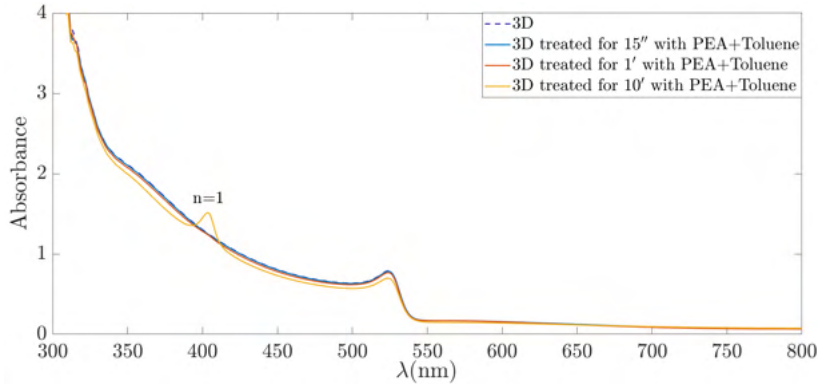

Figure 3.16: Absorbance spectra of THF pristine, THF_PT_30″, THF_PT_3′, THF_PT_10′.

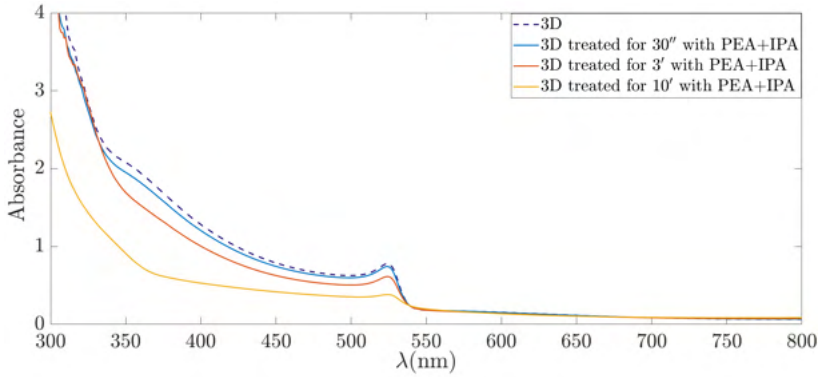

Figure 3.17: Absorbance spectra of THF pristine, THF_PI_30″, THF_PI_3′, THF_PI_10′.

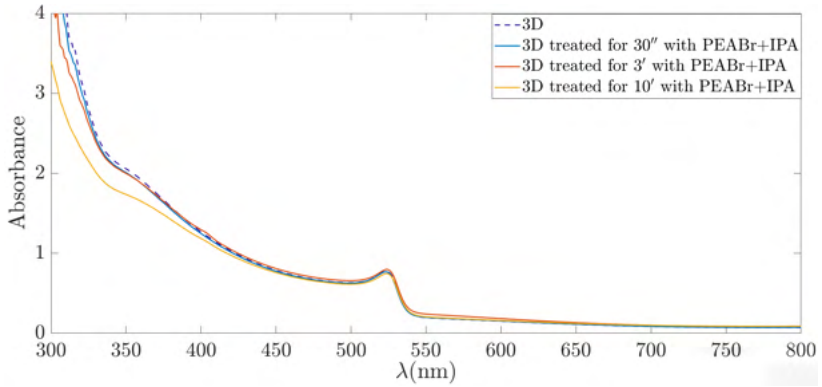

Figure 3.18: Absorbance spectra of THF pristine, THF_PBI_30″, THF_PBI_3′, THF_PBI_10′.

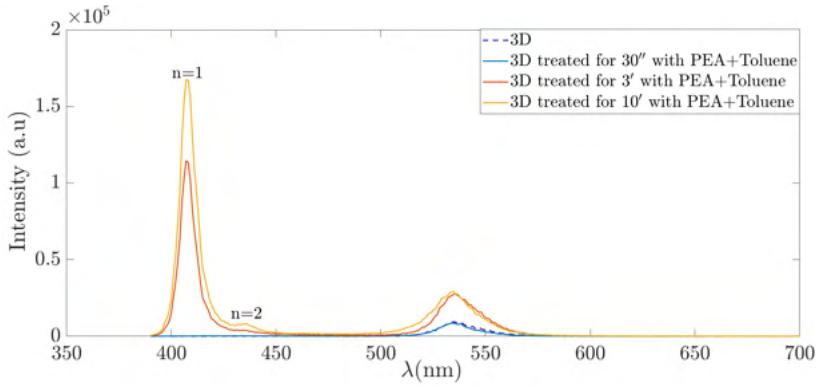

Figure 3.19: PL spectra of THF pristine, THF_PT_30″, THF_PT_3′, THF_PT_10′.

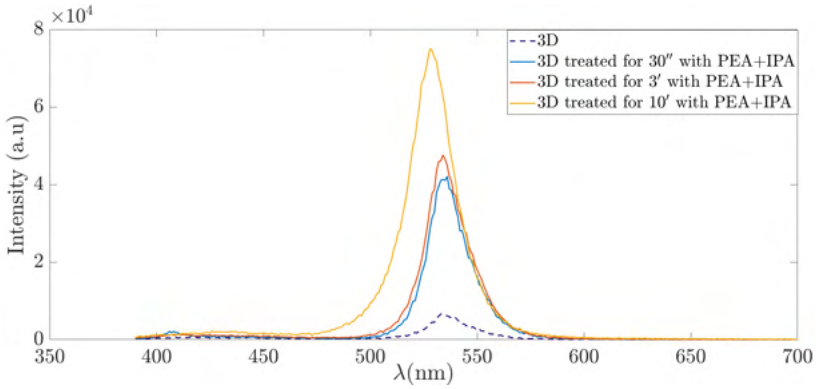

Figure 3.20: PL spectra of THF pristine, THF_PI_30″, THF_PI_3′, THF_PI_10′.

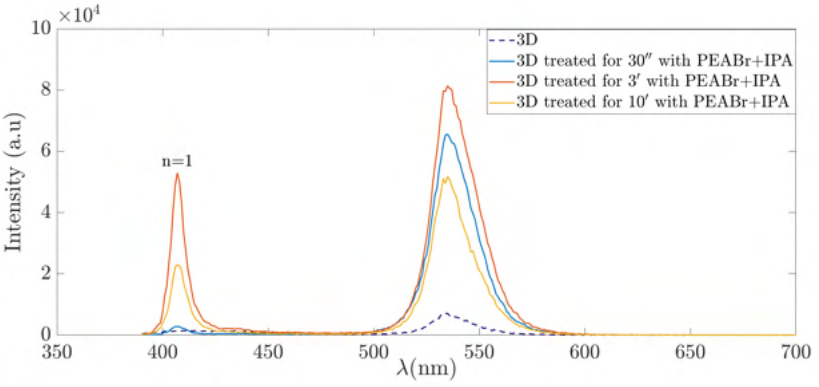

Figure 3.21: PL spectra of THF pristine, THF_PBI_30″, THF_PBI_3′, THF_PBI_10′.

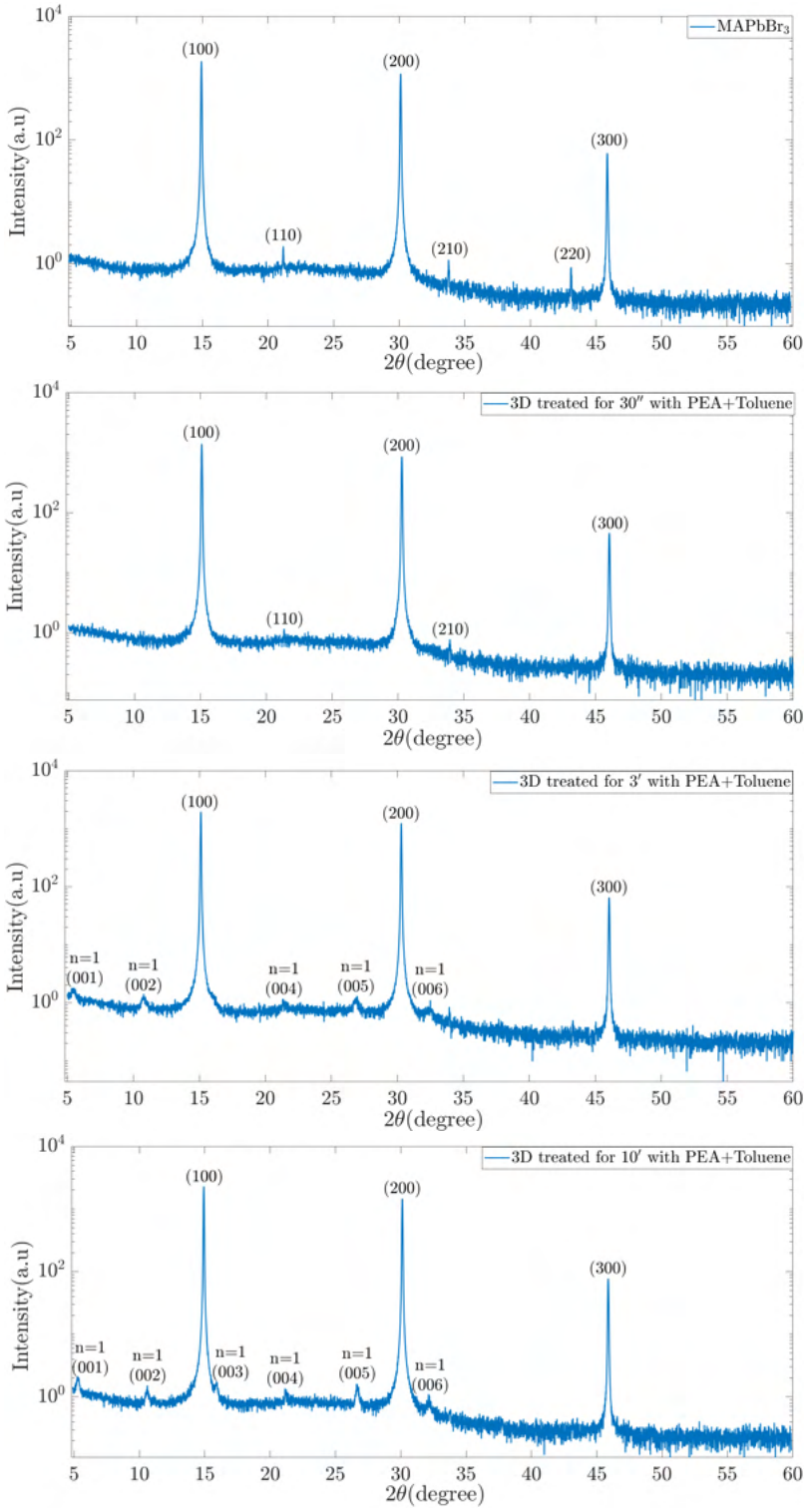

Figure 3.22: XRD spectra of THF pristine, THF_PT_30″, THF_PT_3′, THF_PT_10′.

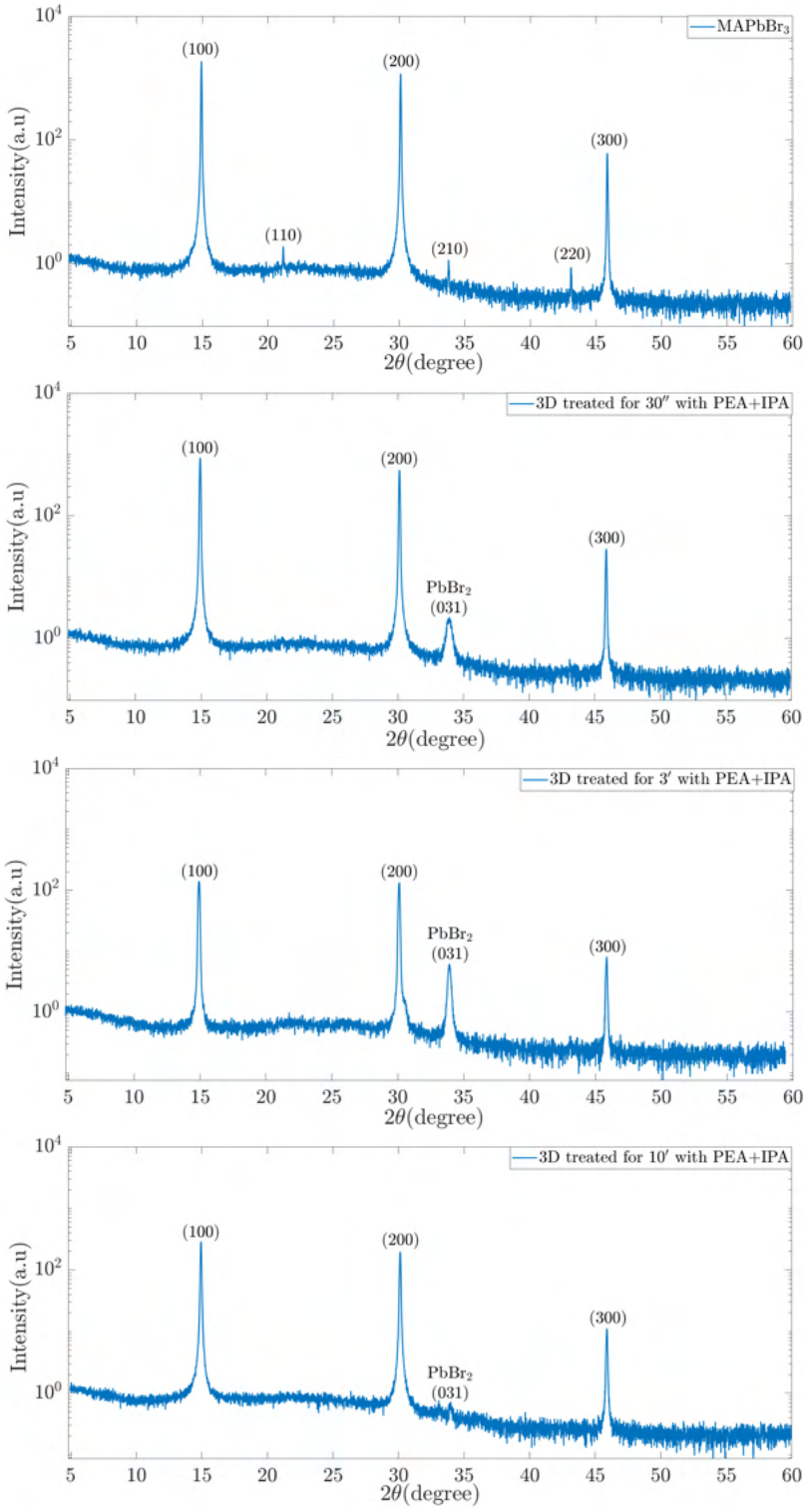

Figure 3.23: XRD spectra of of THF pristine, THF_PI_30″, THF_PI_3′, THF_PI_10′.

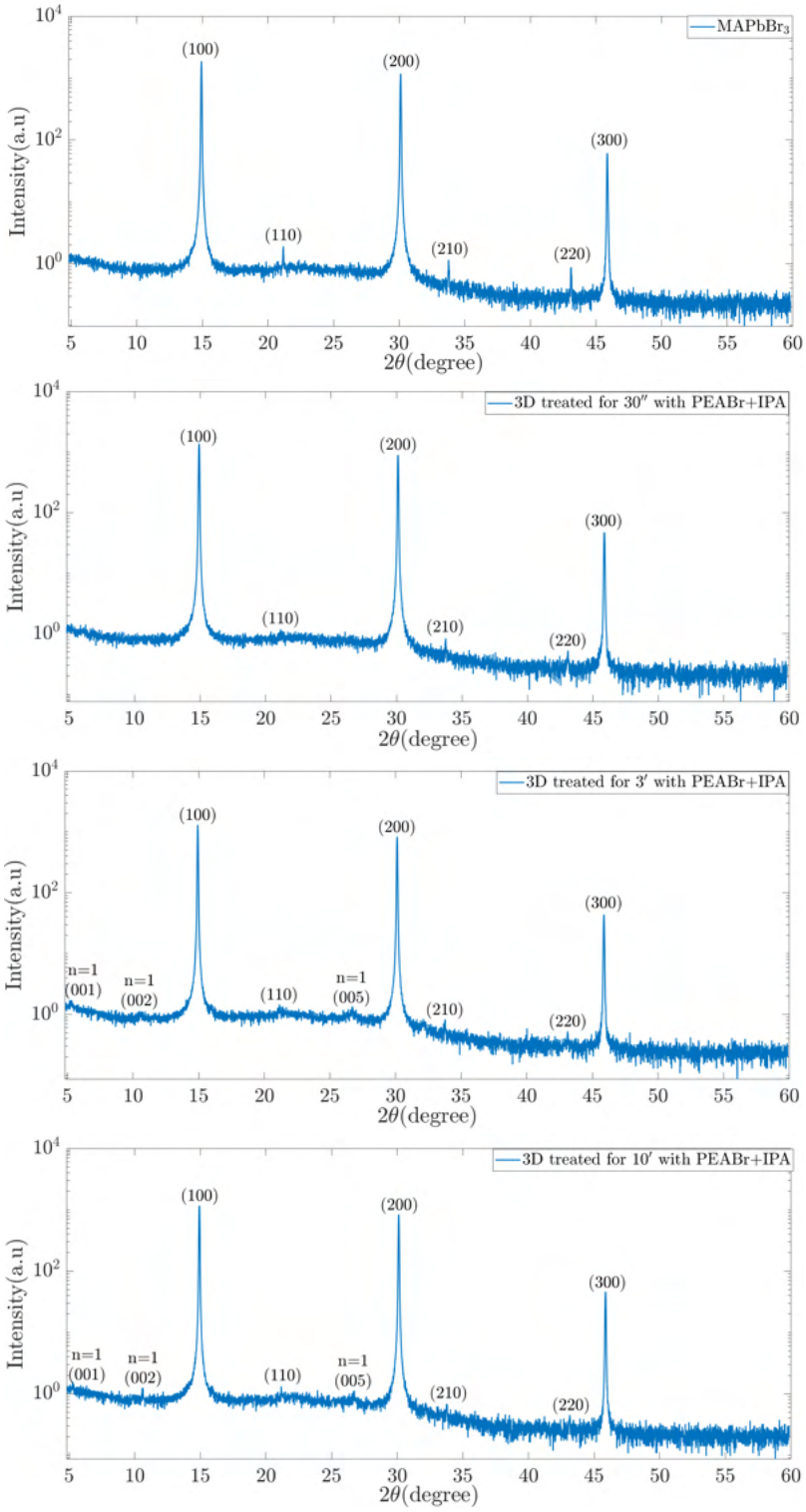

Figure 3.24: XRD spectra of THF pristine, THF_PBI_30″, THF_PBI_3′, THF_PBI_10′.

3.3 Analysis on Charge Transport and Defect States of 2D/3D Perovskite

The study on charge transport and defect states was performed on THFs and SCs treated with PT. The times of treatment for THFs were chosen equal to (15″), 1 minute (1′) and 10 minute (10′). The first two times of treatment were chosen in order to investigate the effect of PT on passivation of surface defect states and hampering of ions movement in case (15″) in which it does not produce a 2D/2D structure and in the case (1′) in which it produces a 2D/3D structure with a 2D perovskite with thin layer n=1. The time of treatment (10′) was chosen in order to study the case in which it produces a 2D/3D structure with a 2D perovskite with thin layer n=1 and n=2. The time of reaction for SCs were chosen equal to 15″ and 1′, because the kinetic of reaction is fast than that of THFs. In the following at first the characteristic of SCs and THFs treated with PT are presented. Then the analysis on charge transport and defect states performed on these samples through I-V and PICTS measurements is illustrated.

3.3.1 Characterization of 2D/3D $MAPbBr_3$ Thin Films

Fig.3.25 shows the images of THFs after the treatment with PT.

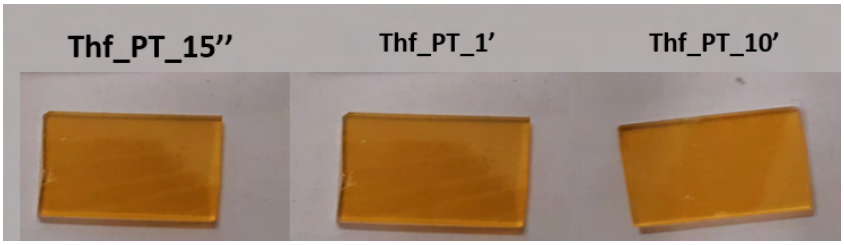

Figure 3.25: Images of THFs after treatment with PT.

The opt and S.E.M micrographs (Figs.3.26a and 3.27a), absorbance, PL and XRD spectra (Figs.3.28, 3.29 and 3.29) PT show that THF_PT_15″ has the same characteristic of THF_PT_1′. The time of treatment 1′ produces a 2D/3D perovskite in which the 2D perovskite was formed with layer n=1. However, unlike time treatment 3′, it was possible to identify the formation of 2D perovskite on 3D only through S.E.M micrograph (Fig.3.27b) and PL measurements (Fig.3.29). The reason why it was not possible detect 2D crystal structure with XRD measurement, is due to that forms on the surface of 3D perovskite and not in the bulk where the sensibility of XRD detector is low. To investigate in deeper the surface of THFs after the treatment with PT, GIXRD measurements were performed on THFs treated. From GIXRD spectra (Fig.3.31) it can be seen that (i) THF_PT_15″ has only the diffraction peak of 3D perovskite, (ii) THF_PT_1′ has the diffraction peak of 2D perovskite with n=1, other 3D one (iii) THF_PT_10′ has the

diffraction peak of 2D perovskite with n=1 and n=2, other 3D one. The characteristic of THFs treated with PI and which were analysed through I-V and PICTS measurements are summarized in table 3.1.

Sample	Characteristic
THF_PT_15″	3D perovskite
THF_PT_1′	2D/3D perovskite (2D with n=1)
THF_PT_10′	2D/3D perovskite (2D with n=1, n=2)

Table 3.1: Characteristic of THFs treated with PT.

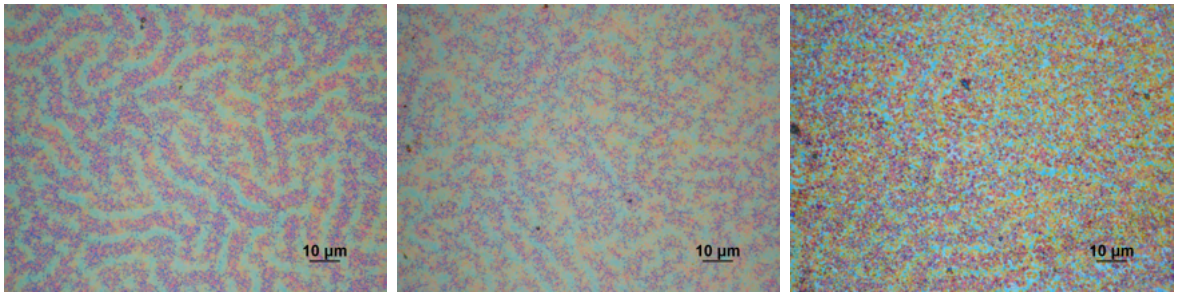

(a) THF_PT_15″ (b) THF_PT_1′ (c) THF_PT_10′

Figure 3.26: Optical microscope images of THFs after treatment with PT.

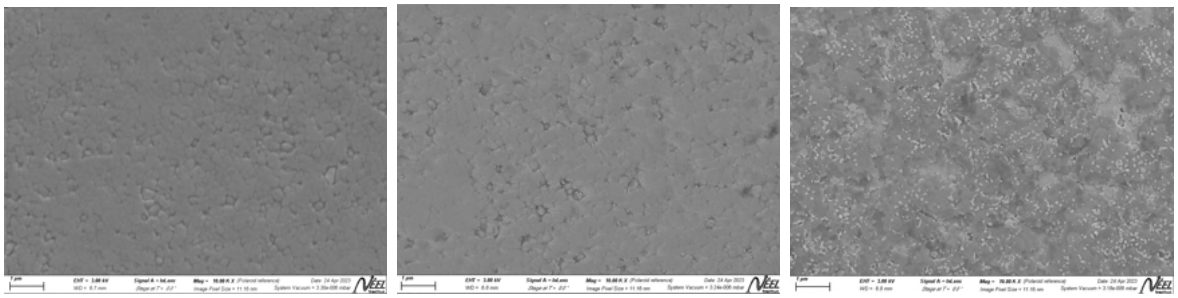

(a) THF_PT_15″ (b) THF_PT_1′ (c) THF_PT_10′

Figure 3.27: S.E.M images of THFs after treatment with PT.

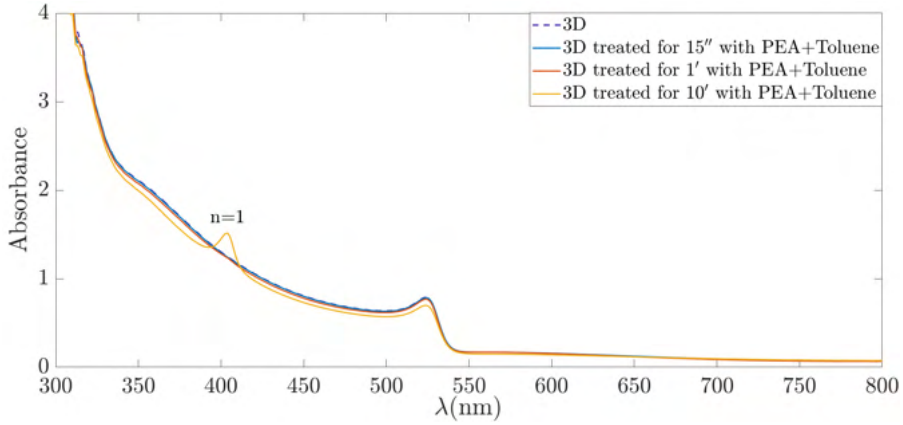

Figure 3.28: Absorbance spectra of THF pristine, THF_PT_15″, THF_PT_1′, THF_PT_10′.

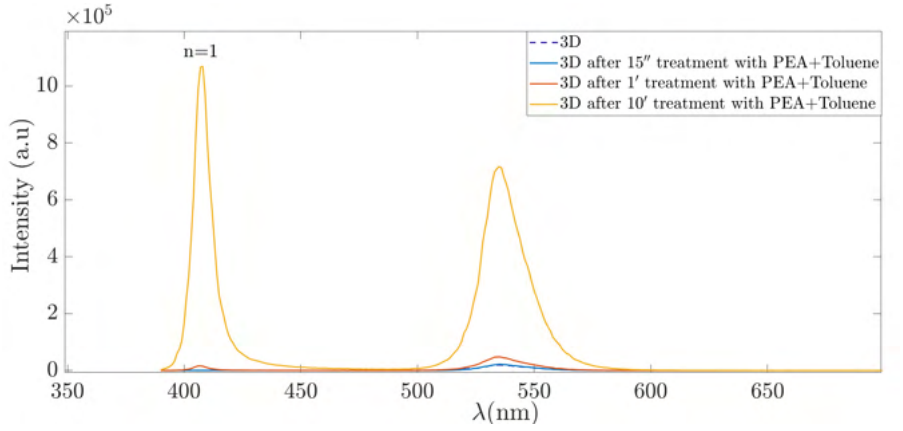

Figure 3.29: PL spectra of THF pristine, THF_PT_15″, THF_PT_1′, THF_PT_10′.

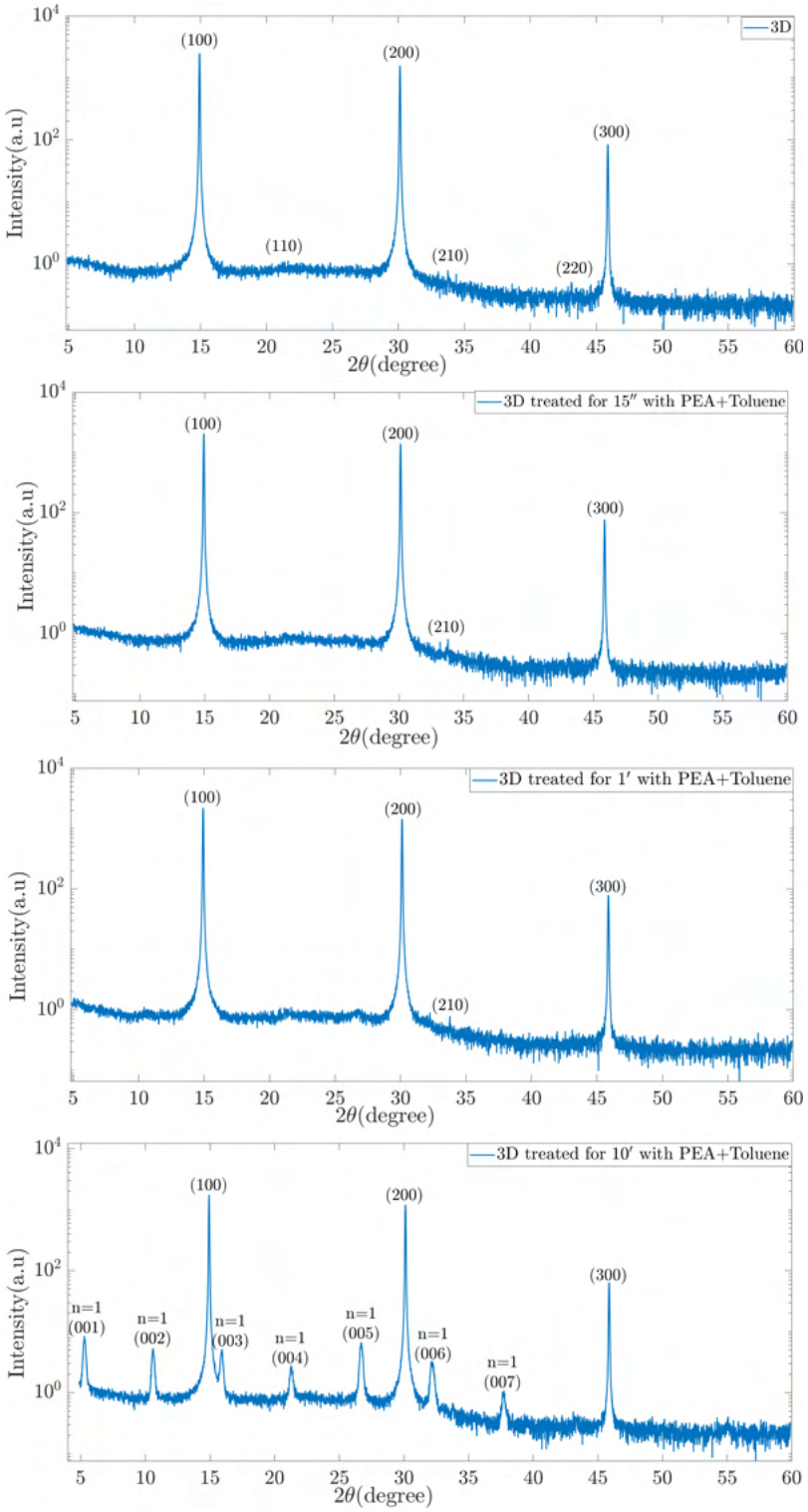

Figure 3.30: XRD spectra of THF pristine, THF_PT_15″, THF_PT_1′, THF_PT_10′.

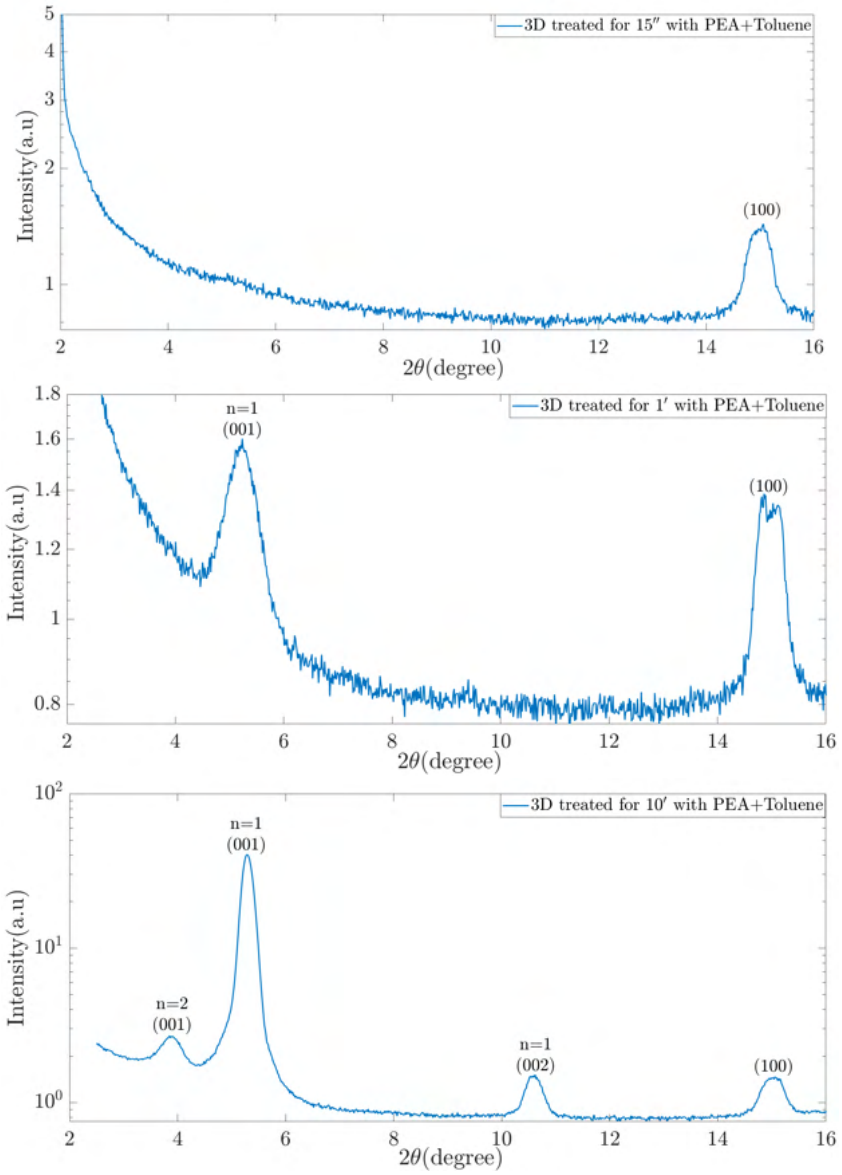

Figure 3.31: GIXRD spectra of THF pristine, THF_PT_15″, THF_PT_1′, THF_PT_10′.

3.3.2 Characterization of 2D/3D $MAPbBr_3$ Single Crystals

Fig.3.32 shows the images of SCs treated with PT.

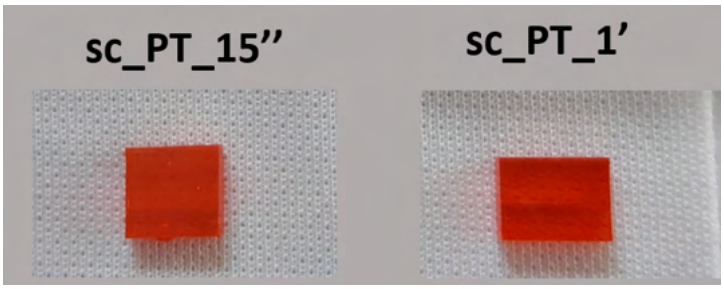

Figure 3.32: Images of SCs after treatment with PT.

The opt micrograph of SC_PT_15″ and SC_PT_1′ are shown in Fig.3.33. The PL measurements allowed to detect (i) for SC_PT_15″ a 2D PL peak which corresponds to 2D perovskite with layers n=1 (ii) for SC_PT_15″ a 2D PL peaks which correspond to 2D perovskite with layers n=1 and n=2. The PL spectra of SCs pristine, SC_PT_15″ and sc_PT_1′ are shown in Fig.3.34. The XRD spectra Fig.3.35 of SC_PT_15″ and SC_PT_1′ present only 3D diffraction peaks. This means that the 2D perovskite is formed for both times of treatment on the surface and not in the bulk. To investigate in deeper the surface of 3D SC after the treatment, GIXRD measurements are performed on treated SCs. From GIXRD spectra (Fig.3.36) it can be seen that only that of SC_PT_1′ has the diffraction peak of 2D perovskite with n=1. In conclusion, the analysis conducted on SCs treated shows that (i) the time of treatment 15″ produces a 2D/3D perovskite structure in which the 2D perovskite forms with layer n=1 (ii) the time of treatment 1′ produces a 2D/3D perovskite structure in which the 2D perovskite forms with layers with n=1 and n=2. The characteristic of SC treated with PI and which were characterized through I-V and PICTS measurements are summarized in table.3.2.

Sample	Characteristic
SC_PT_15″	2D/3D with (2D with n=1)
SC_PT_1′	2D/3D (2D with n=1 and n=2)

Table 3.2: Characteristic of SCs treated with PT.

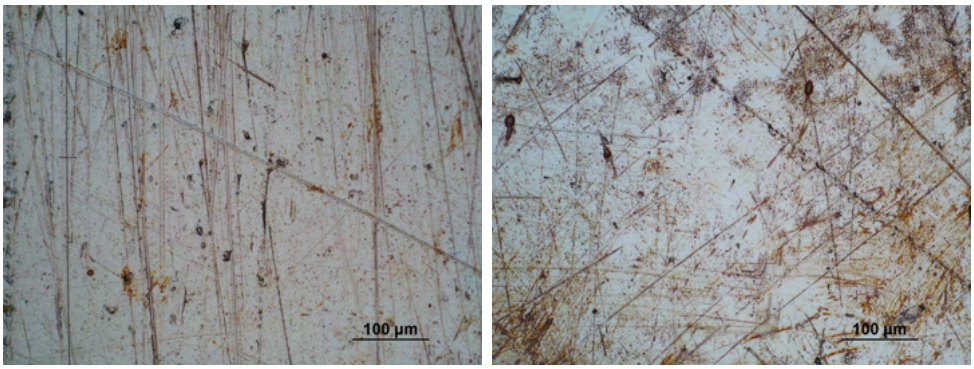

(a) SC_PT_15″ (b) SC_PT_1′

Figure 3.33: Optical microscope image of scs after treatment with PT.

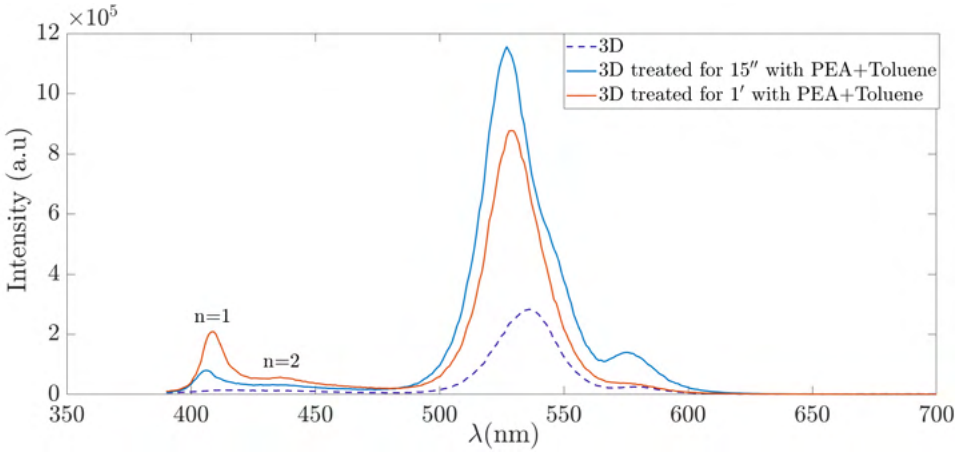

Figure 3.34: PL spectra of SC pristine, SC_PT_15″, SC_PT_1′.

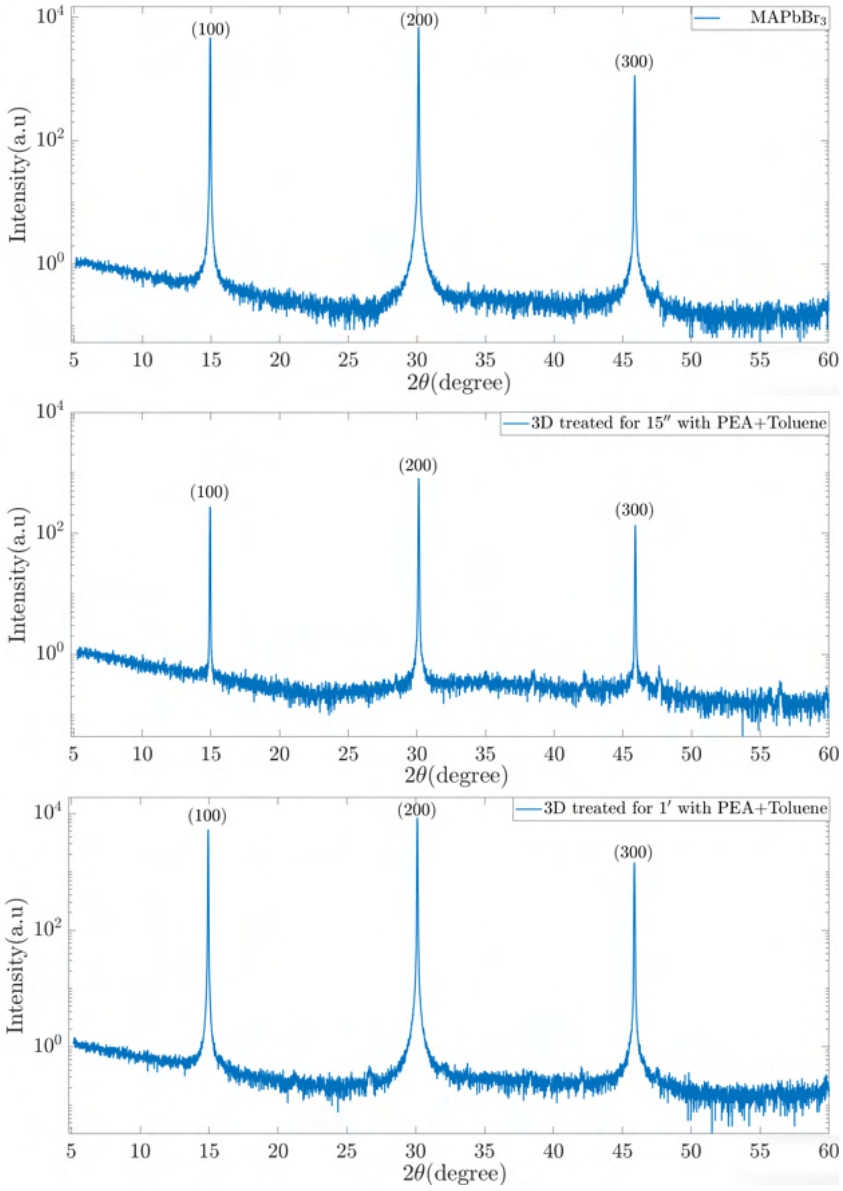

Figure 3.35: XRD spectra of SC pristine, SC_PT_15″, SC_PT_1′.

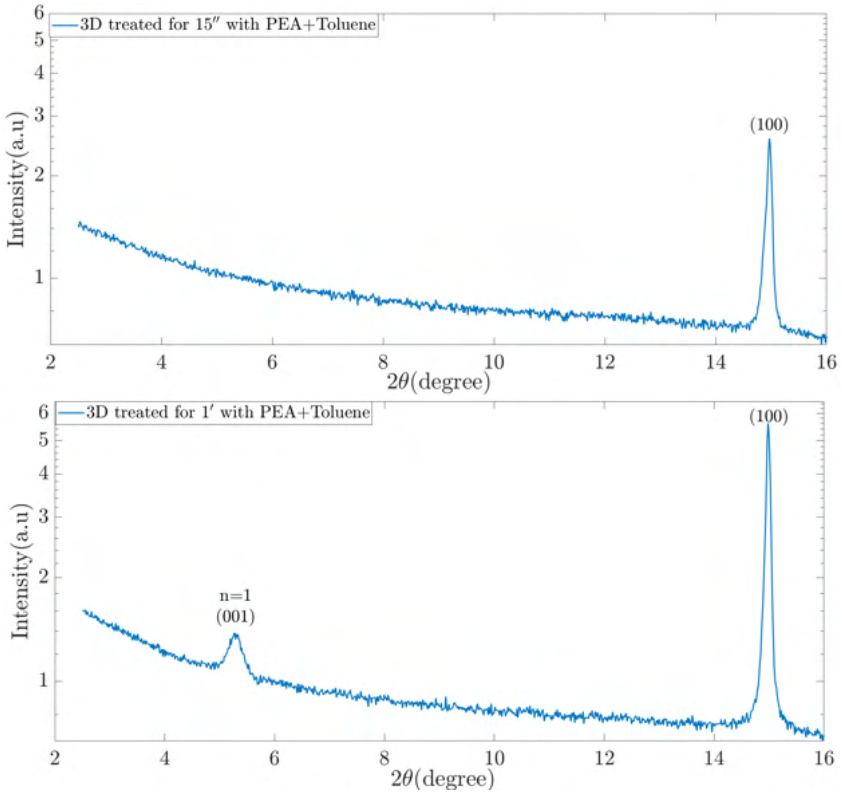

Figure 3.36: GIXRD spectra of SC pristine, SC_PT_15″, SC_PT_1′.

3.3.3 I-V Characterization of 2D/3D $MAPbBr_3$ Thin Films

The current-voltage (I-V) characteristics in dark and in light of THF pristine, THF_PT_15″, THF_PT_1′, THF_PT_10′ measured in air and in vacuum at 300K are shown respectively in Fig.s 3.37 and 3.38. From such graphs it can be observed that:

(i) the curves of pristine and treated THFs have an ohmic behaviour both in air and in vacuum (the curve at negative voltage is symmetric to that positive voltage)

(ii) the curves under vacuum condition show current value of 2-3 order of magnitude lower than that in air (dark and light). This is can be explained considering that the grain boundaries in polycrystals capture water and oxygen molecules which filling these or other defects passivate in some sense them and improving in this way the overall charges transport. When the I-V curves are measured in vacuum this beneficial effect disappears because the air and oxygen molecules are removed from vacuum pump and this causes a decrement of current values

(iii) THF_PT_10′ is low conductive. The current value measured has the same order of magnitude (picoamperes) of the instrumental noise.

To verify if the treatments PT 15″ and 1′ have improved the charge transport in 3D perovskite, it was performed the graphs shown in Fig.s 3.39 and 3.40 in order to compare the current values of THFs pristine and treated. From such graphs it can be observed that:

(i) In air the values of current of THF_PT_15″ in dark and light are high compared to THF pristine and THF_PT_1′

(ii) In general there is no trend for current value of THFs treated which allows to affirm that charge transport properties are improved after the treatment.

To assess which effect the treatments PT 15″ and 1′ have had on hampering the ions migration in 3D perovskite the ions migration activation energy E_a was calculated by performing Nernst-Einstein fit. To calculate these, first the resistivity of THFs pristine and treated were derived by linear fitting the I-V temperature dependent characteristics at 20V in dark. Then it was performed a linear fit using Nernst-Einstein relation. Nerst-Einstein fit performed on THFs pristine and treated for 15″ and 1′ are shown in Fig.3.41, whereas the E_a values are listed in table 3.3. The E_a values are compatible with those reported for 3D perovskite which are typically between 0.2-0.8 eV [18], but results higher for a materials in which ions play an important role in charge transport[5][11]. The high ions activation energy may be due to barrier potential which found at grain boundaries in the polycrystals which could limit the ion movement, but not that of charge carriers(holes or electrons)[5]. The increasing and decreasing of E_a values with time of treatment may be due to a change in dimension of grain boundaries [19],[21], observed in S.E.M

micrographs (Fig.s3.27). By plotting the conductivity versus 1/T in Nernst-Einstein formalism (Fig.3.41) it seems that there is another activation energy which could be that of electronic conduction regime [9].

Sample	$E_a(eV)$
THF pristine	(0.58±0.02)
THF_PT_15″	(0.69±0.03)
THF_PT_1′	(0.55±0.01)

Table 3.3: Activation energy values for THFs extracted by Nerst-Einstein fit.

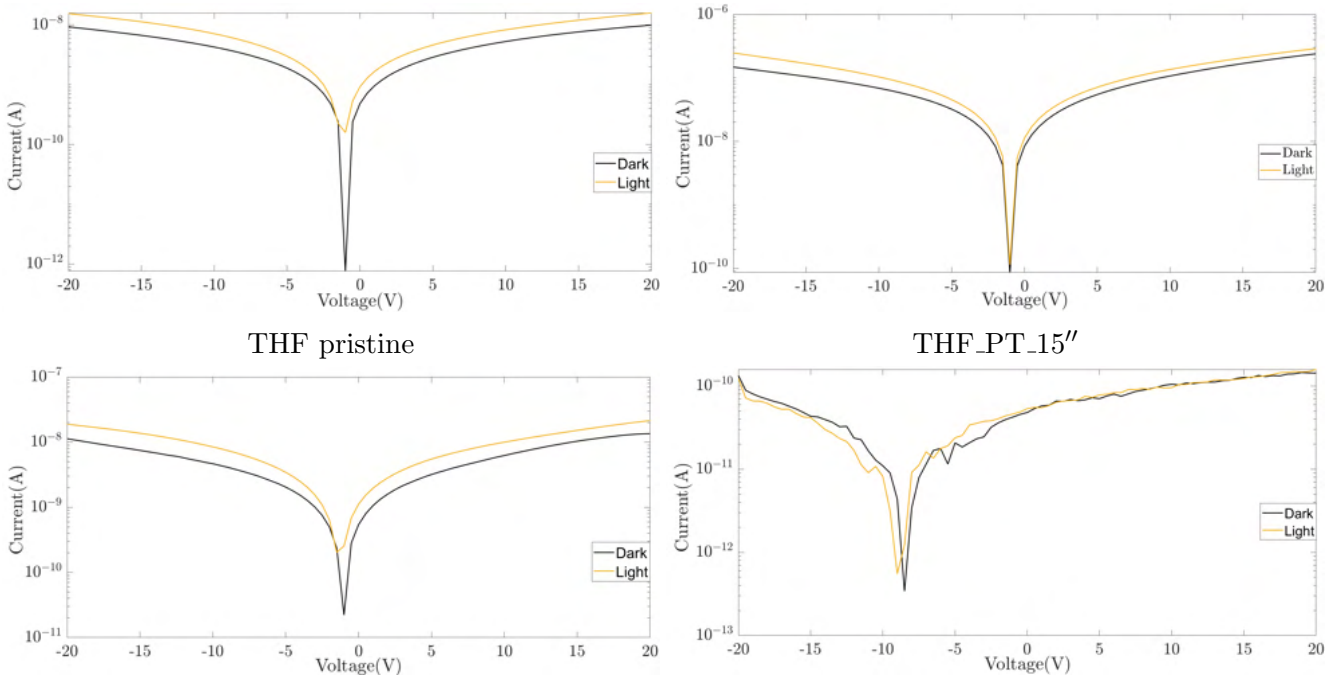

THF pristine THF_PT_15″

THF_PT_1′ THF_PT_10′

Figure 3.37: I-V curve, measured in air at 300K for THFs.

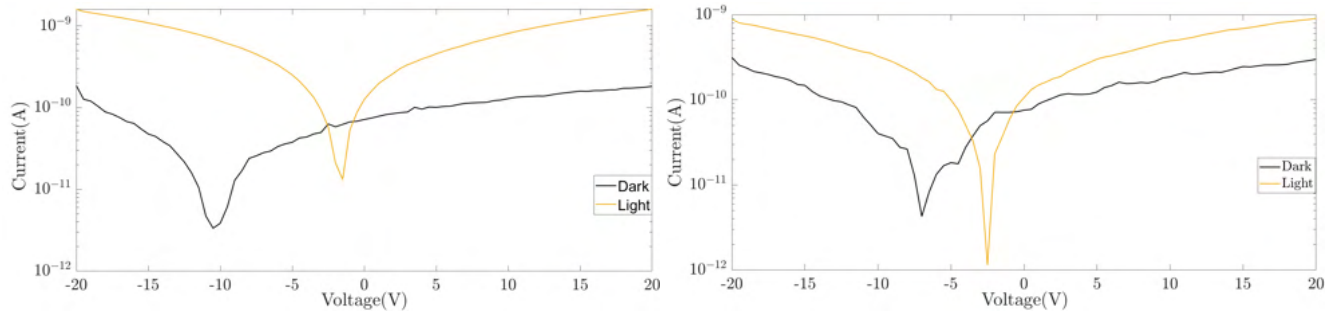

THF pristine

THF_PT_15″

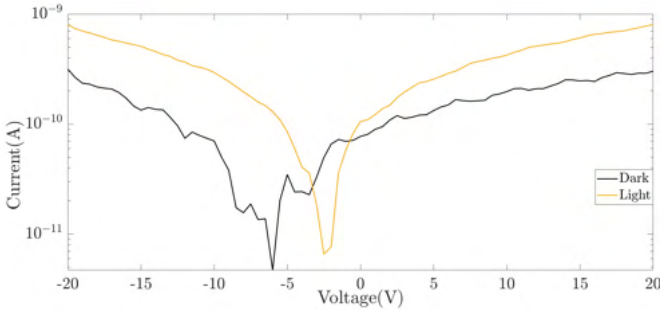

THF_PT_1′

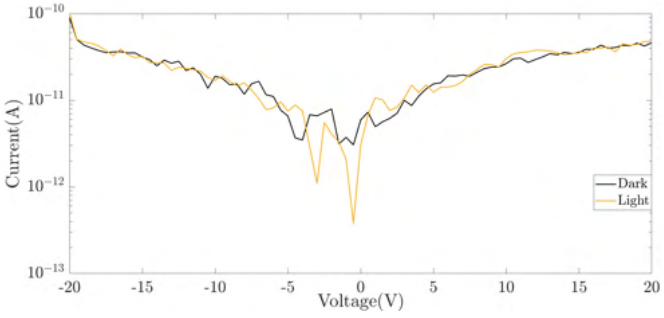

THF_PT_10′

Figure 3.38: I-V at 300K in vacuum for THFs .

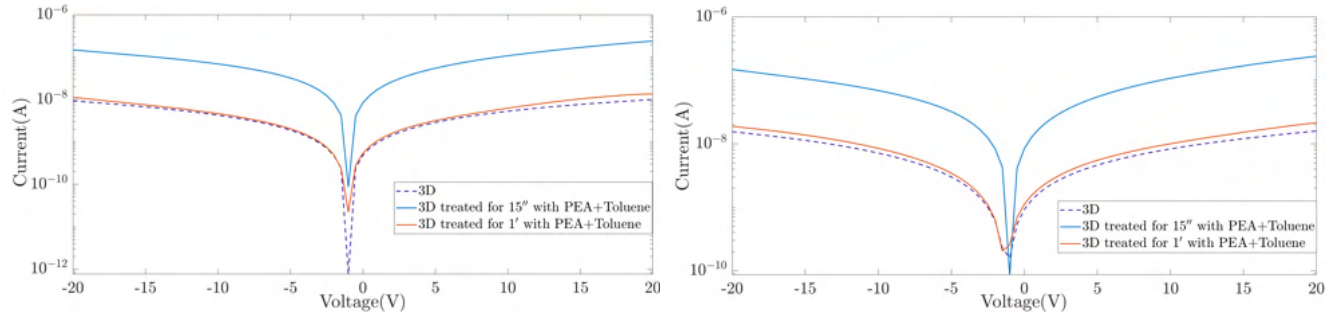

I-V in dark I-V in light

Figure 3.39: I-V at 300K in air of THF pristine, THF_PT_15″, THF_PT_1′, THF_PT_10′.

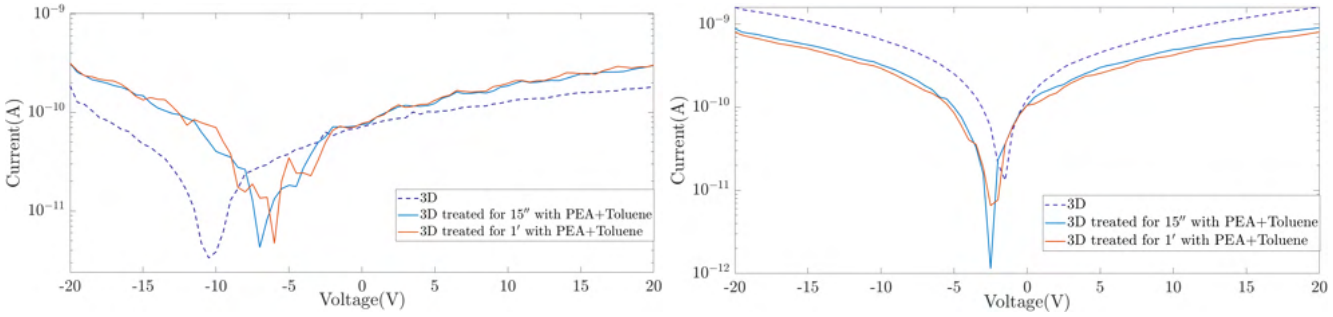

I-V in dark I-V in light

Figure 3.40: I-V at 300K in vacuum of THF pristine, THF_PT_15″, THF_PT_1′, THF_-PT_10′.

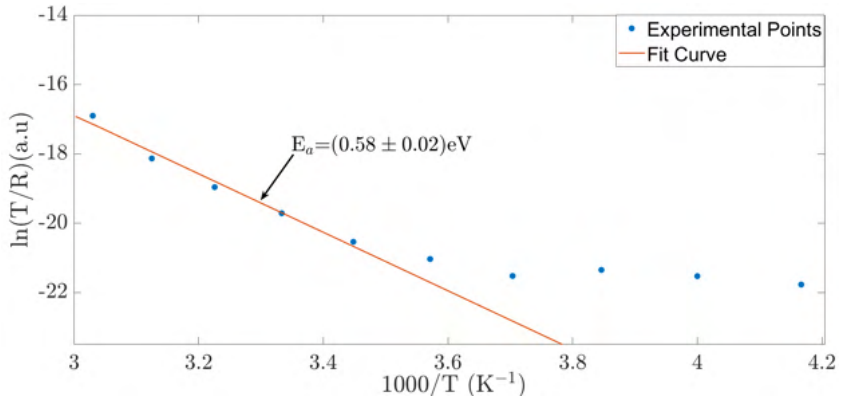

THF pristine

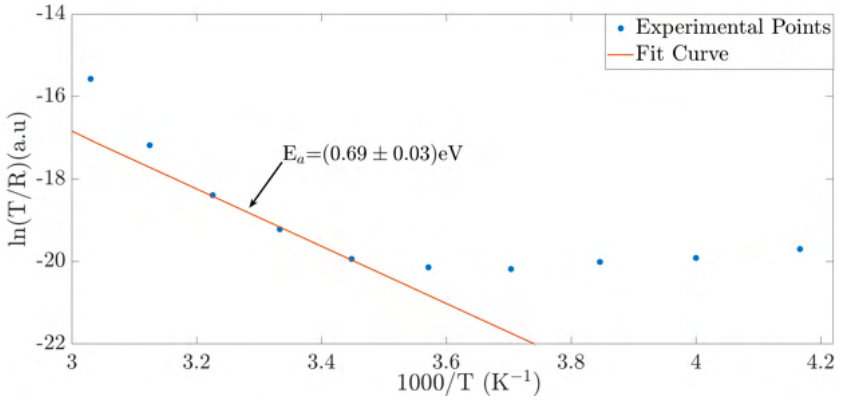

THF_PT_15″

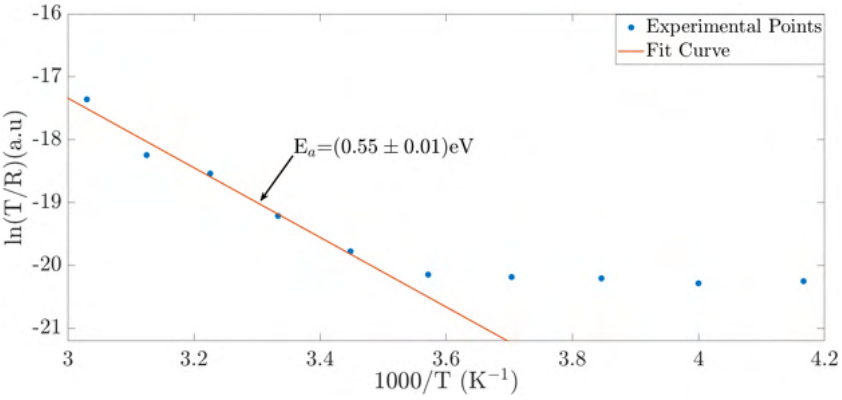

THF_PT_1′

Figure 3.41: Nernst-Einstein fit at 20V for THFs.

3.3.4 I-V Characterization of 2D/3D $MAPbBr_3$ Single Crystals

The current-voltage (I-V) characteristics in dark and in light of SC pristine, SC_PT_15″ and SC_PT_1′ measured in air and in vacuum at 300K are shown respectively in Fig.s 3.42 and 3.43. From such graphs it can be observed that:

(i) the curves of pristine and SCs treated show current values of the same order of magnitude both in air and in vacuum. This may be ascribable to the absence of grain boundaries in SC, that capturing water and oxygen molecules in polycrystals make higher the current value in air compared to vacuum

(ii) the curves in dark and light of SC pristine and treated for 15″ and 1′ are asymmetric with the current at +20V of almost one order of magnitude higher than that at -20V. This can be explained by considering the top-bottom contact geometry of the electrodes used to perform I-V measurements and that the mobility of holes is higher than that of electrons [5][22]. When the top contact is negative polarized, the holes reach quickly this contact. When instead the top is positive polarized the electrons to reach this electrode employee more time causing this asymmetry between positive and negative voltage.

To verify if the treatments PT 15″ and 1′ have improved the charge transport in 3D perovskite, it was performed the graphs shown in Fig.s 3.44 and 3.45 in order to compare the current values of SCs pristine and treated. From such graphs it can be observed that:

(i) In vacuum and air the value of current in dark of SC_PT_1′ is higher than that SC pristine and SC_PT_15″

(i) In general there is no trend for current value of SCs treated which allows to affirm that charge transport properties are improved after the treatment.

To assess which effect the treatments PT 15″ and 1′ have on hampering the ions migration in 3D perovskite, the ions migration activation energy E_a were calculated by performing Nernst-Einstein fit. To calculate these, first the resistivity of SC pristine and treated for 15″ and 1′ were derived by linear fitting the I-V temperature dependent characteristics at 20V in dark. Then it was performed a linear fit using Nernst-Einstein relation. Nerst-Einstein fit performed on SCs pristine and treated for 15″ and 1′ are shown in Fig.3.46, whereas the E_a values found through these fit are listed in table 3.4. The E_a values are very similar to each others and compatible with those reported for 3D perovskite which are typically between 0.2-0.8 eV [18]. The low value of E_a means that ions gives an important contribution to conductivity of the materials[5][9][19]. By plotting the conductivity versus 1/T in Nernst-Einstein formalism (Fig.3.46) shows that there is only one activation energy which is that of ionic conduction regime [9].

Sample	$E_a(eV)$
SC pristine	(0.31±0.02)
SC_PT_15″	(0.29±0.02)
SC_PT_1′	(0.34±0.01)

Table 3.4: Activation energy values for SCs extracted by Nerst-Einstein fit.

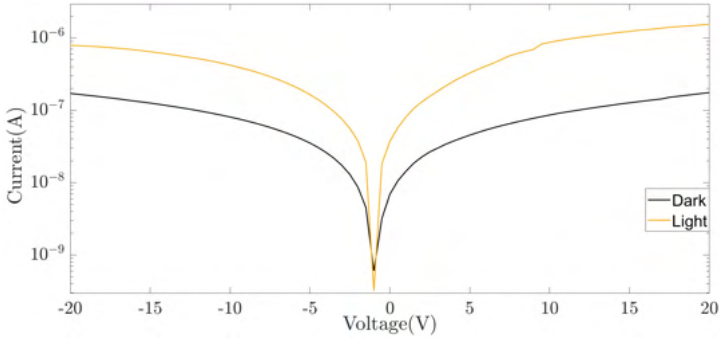

SC pristine

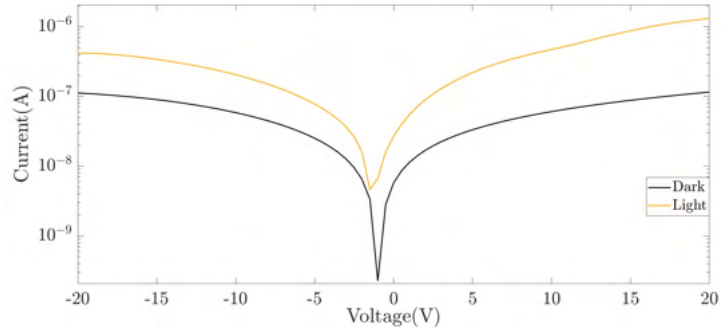

SC_PT_15″

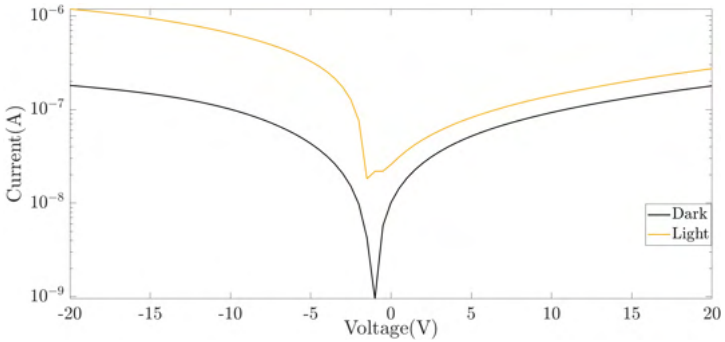

SC_PT_1′

Figure 3.42: I-V at 300K in air for SCs.

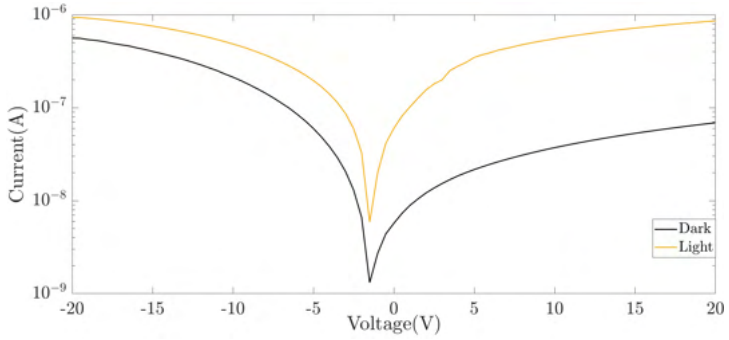

SC pristine

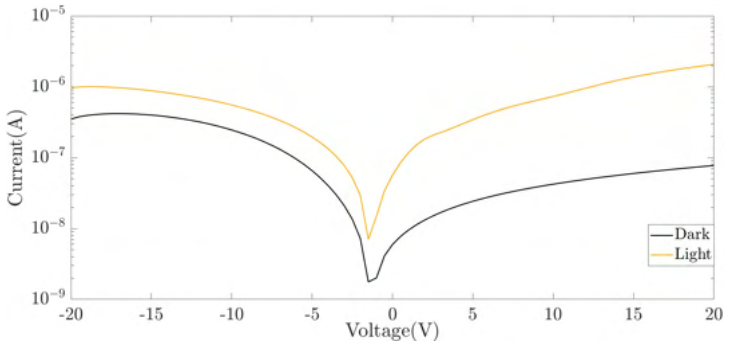

SC_PT_15″

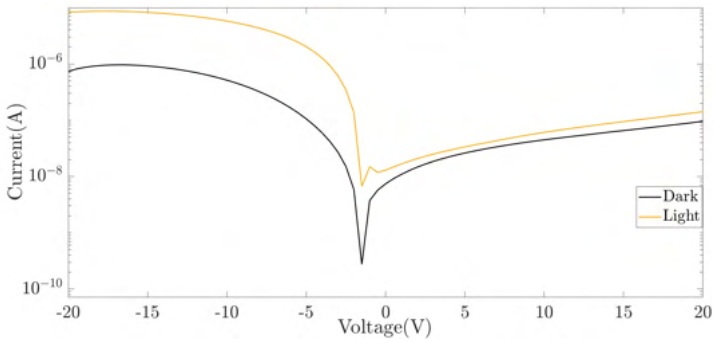

SC_PT_1′

Figure 3.43: I-V at 300K in vacuum for SCs.

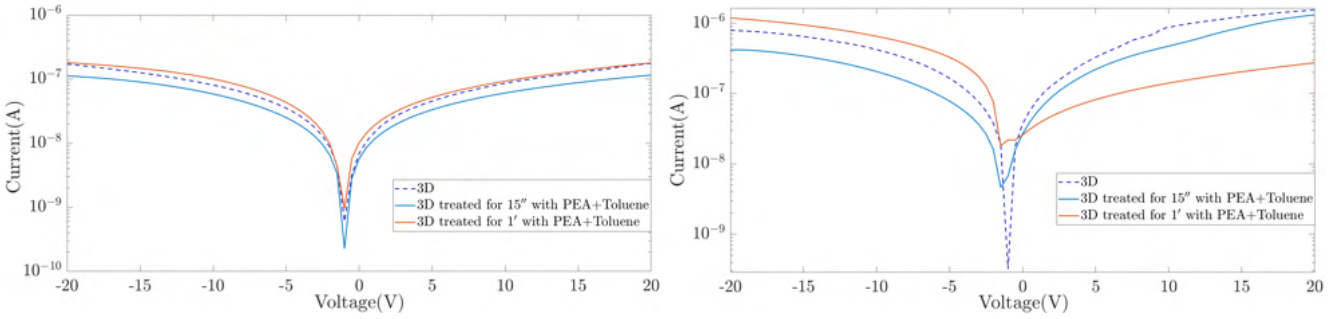

I-V in dark I-V in light

Figure 3.44: I-V at 300K in air of SCs pristine, SC_PT_15″ and SC_PT_1′

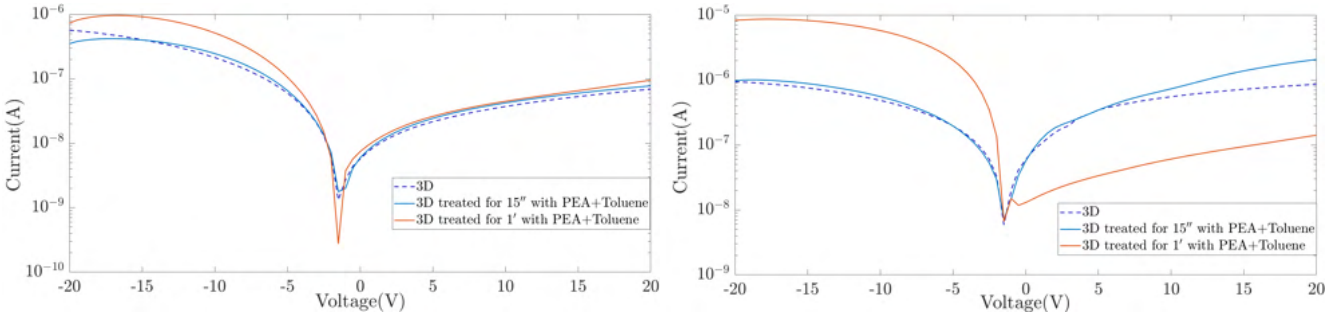

I-V in dark I-V in light

Figure 3.45: I-V at 300K in vacuum of SCs pristine, SC_PT_15″ and SC_PT_1′.

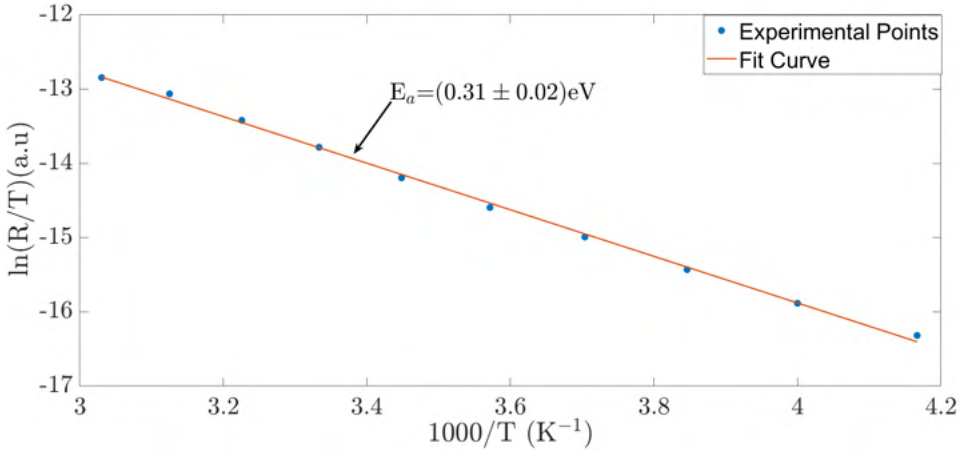

SC pristine

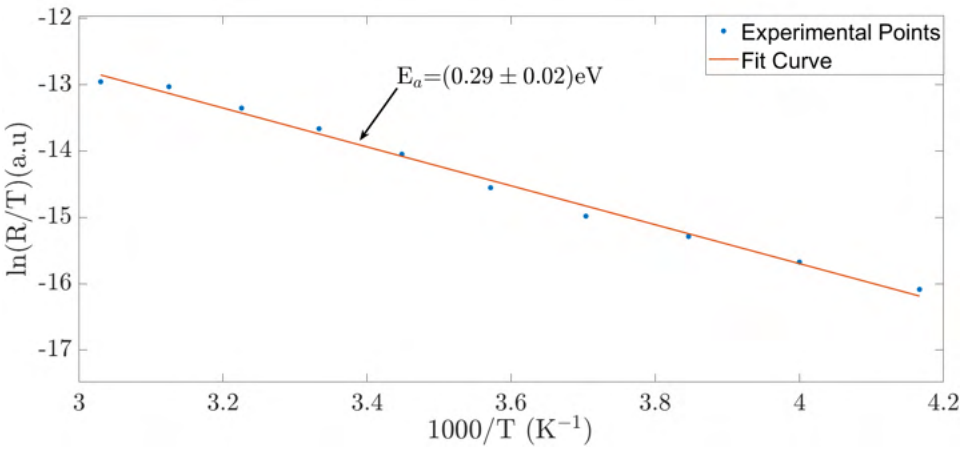

SC_PT_15″

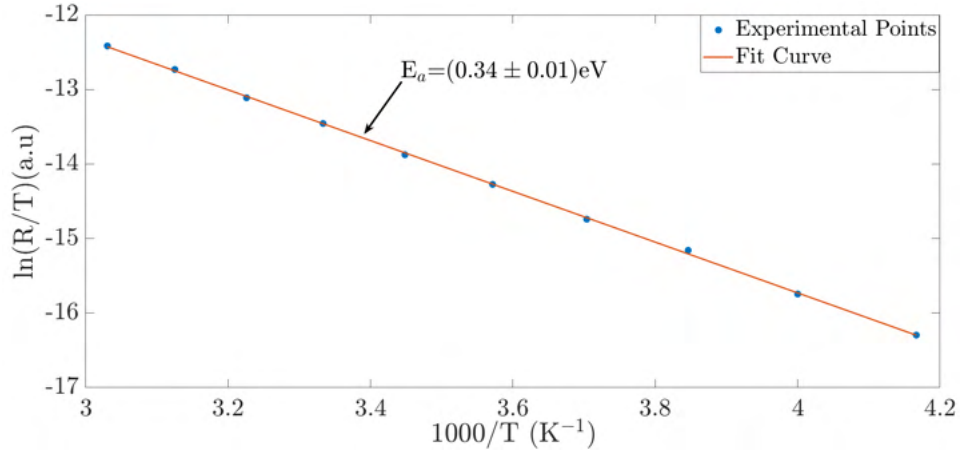

SC_PT_1′

Figure 3.46: Nernst-Einstein fit at 20V for SCs.

3.3.5 PICTS Measurements on 2D/3D $MAPbBr_3$ Thin Films

Fig.3.47 shows the photocurrent transients of THF pristine, th_PT_15″, th_PT_1′ acquired in the temperature range (240-330)K and at negative voltages (-5V). The photocurrent transient of th_PT_10′ was not detectable because of low conductivity. The photocurrent transient shape of THFs pristine and treated shown in figure 3.47 is similar to that reported in literature for electronic defect states (Fig.2.12d) rather than that due to ions drifts (Fig.2.14d). In fact there is no asymmetry in rise and fall time which indicate that the PICTS signal is generated by slow charge, the ions[15]. Moreover the transient decay time, 10^{-3}s is too fast compared to that reported in literature for photocurrent generated by ions drift which is of order of second, and the frequency value, 300 Hz, to photogenerate the charge carriers is higher compared to that reported in literature 3D $MAPbBr_3$ (0.1-100Hz)[15]. All this information suggests that the defects in THFs could not have ionic nature. The nature of defects cannot be determined through PICTS measurements because of absence of the PICTS signals from the measured photocurrents (Fig.3.48). The absence of PICTS signal can be due to no temperature dependence of the photocurrent.

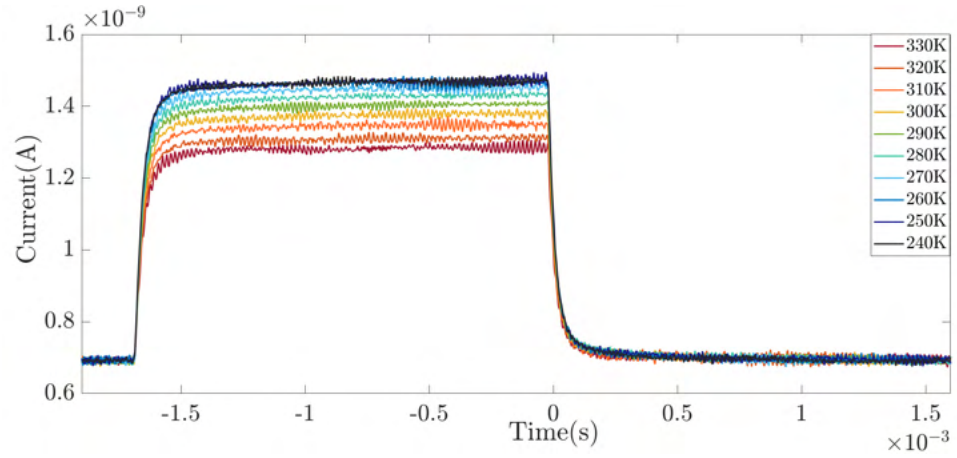

THF pristine

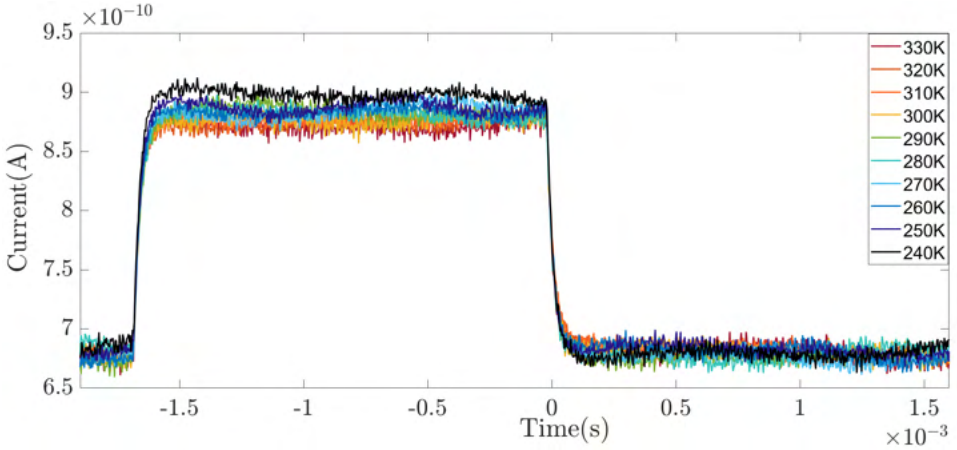

THF_PT_15″

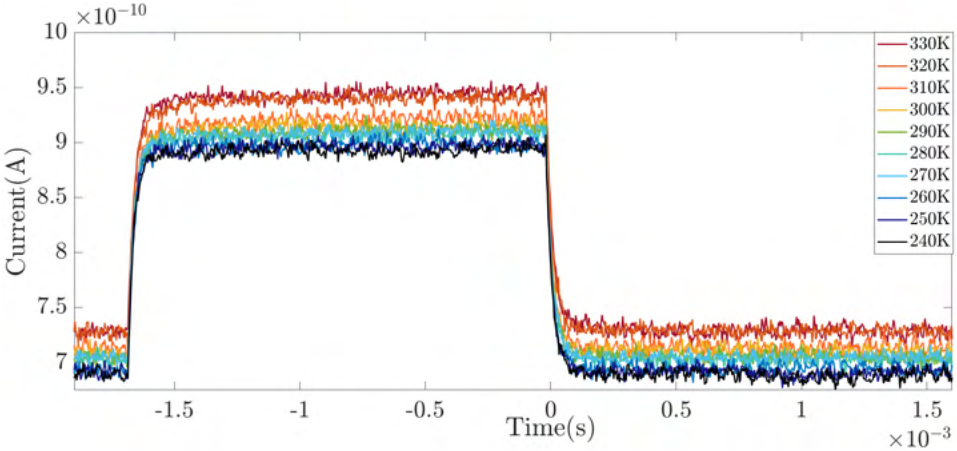

THF_PT_1′

Figure 3.47: Photocurrent transients of THFs.

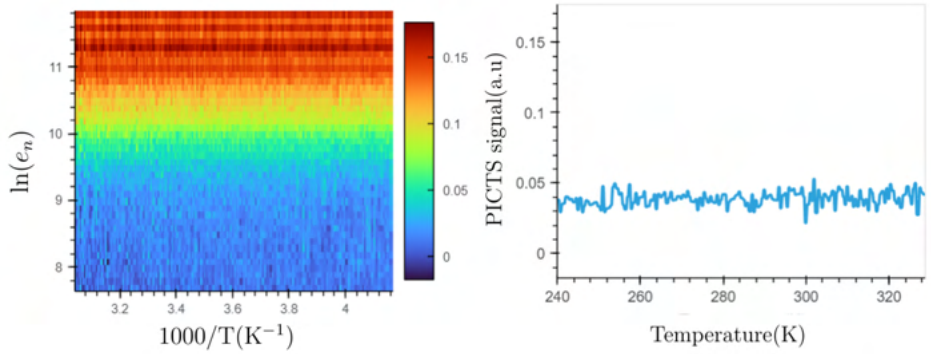

THF pristine

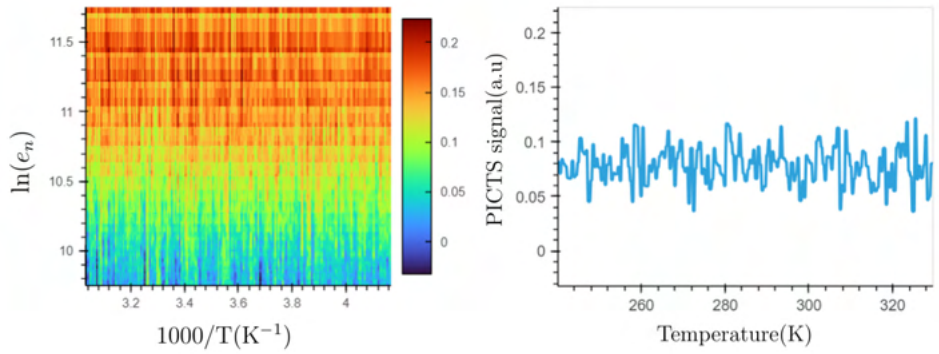

THF_PT_15″

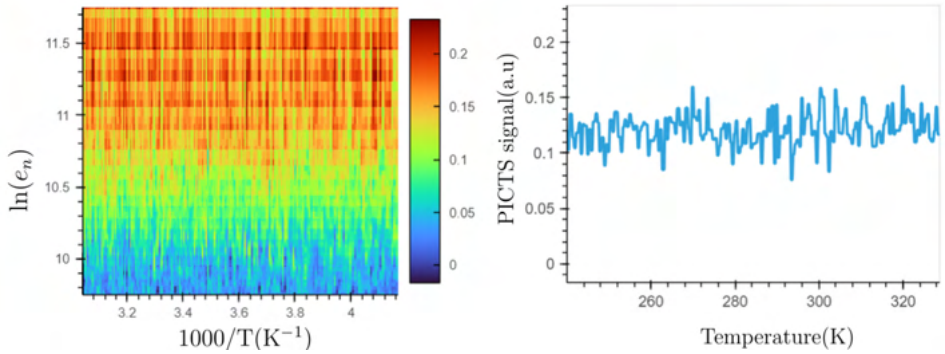

THF_PT_1′

Figure 3.48: PICTS maps of THFs

3.3.6 PICTS Measurements on 2D/3D $MAPbBr_3$ Single Crystals

The photocurrent transients of SC pristine and SC_PT_15″ and SC_PT_1′ measured in temperature range (240-330)K and at negative voltage (-5V) are shown in figure 3.49. Unlike THFs, the photocurrent transients of SCs pristine and treated show the asymmetry in rise and fall time which is typical of photocurrent transients produced by ions drifts. Moreover the decay time of photocurrent, of order of seconds, and the frequency value, 0.2 Hz, to photogenerate charge carriers are compatible with those reported in literature for photocurrent transients due to ions drifts[15]. The PICTS maps of SC pristine and SC_PT_15″ and SC_PT_1′, calculated from photocurrent transients, are shown respectively in Fig.3.48. Using this PICTS maps, it was possible to build the Arrhenius plot from which the nature of defects and their activation energy can be determined. The figure 3.51 shows the trap signatures of SC pristine and treated, and compares them with those reported in literature for ions migration defects in 3D $MAPbBr_2$ and PEA_2PbBr_4 (2D perovskite)[15][23]. In this Arrhenius plot (Fig.3.51) the signatures of single crystal pristine and untreated lay in a region which corresponds to signatures measured at medium frequency and negative voltage. This collocation for the trap signature in the Arrhenius plot is in agreement with the experimental conditions at which the transients were measured. According to Arrhenius plot of trap signatures for ions migrations the defects of SC pristine and treated corresponds to positive ions species [15][23]. These positive ionic species were identified with bromine vacancy[15][23]. The table 3.5 reports the activation energy calculated from Arrhenius and the tentative of assignment of PICTS signature. For SC_PT_1′ it was not possible to determine exactly the ions activation energy because of weak PICTS signal from the acquired photocurrent. The low values of E_a for SC_PT_15′ and the same type of defect of SC pristine could be indicate that PT is not efficient to passivate the bromine vacancy in $MAPBBr_3$.

Single Crystal	E_a(eV)	Tentative of assignment
SC pristine	(0.473 ± 0.003)	$V^{\bullet}_{Br}$
SC_PT_15′	(0.372 ± 0.005)	$V^{\bullet}_{Br}$

Table 3.5: Experimental value of ions activation energies obtained by PICTS measurements and the tentative assignment of the PICTS signature with ions migration species.

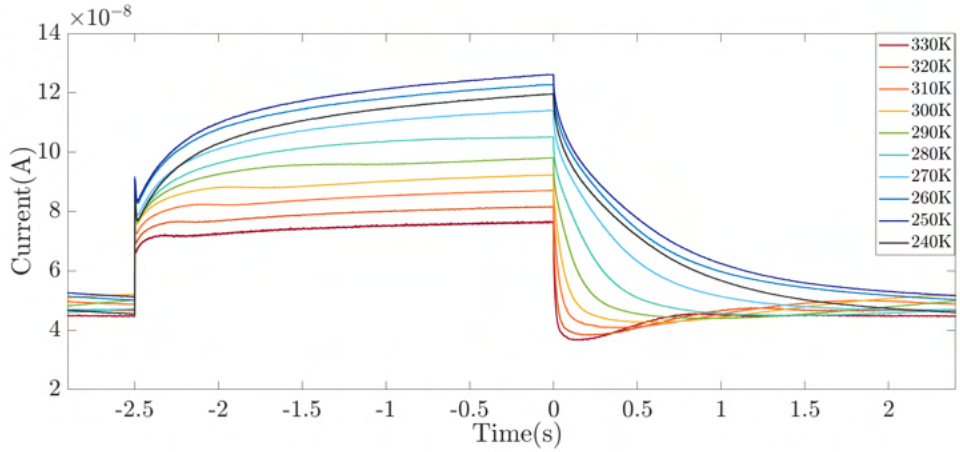

SC pristine

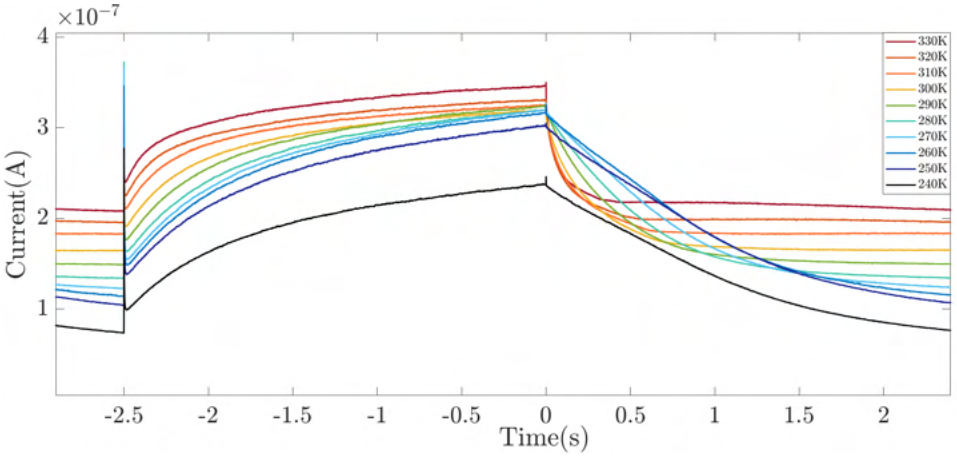

SC_PT_15″

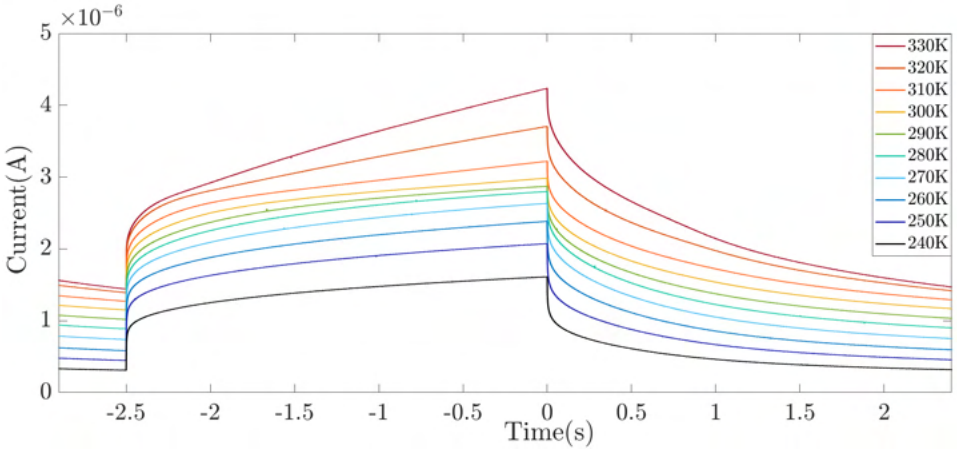

SC_PT_1′

Figure 3.49: Photocurrent transients of SCs.

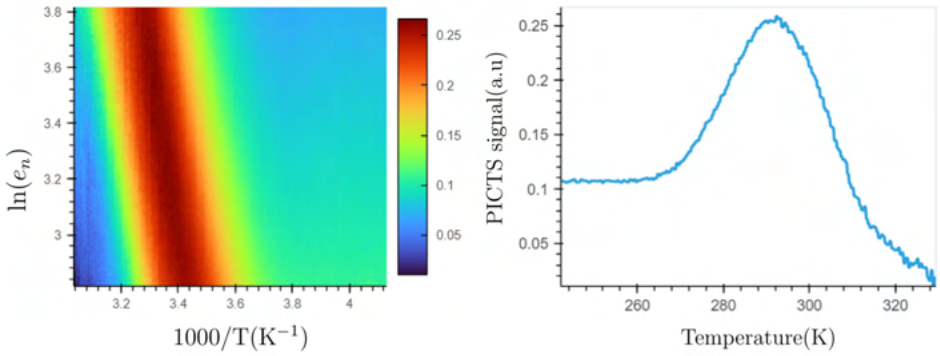

SC pristine

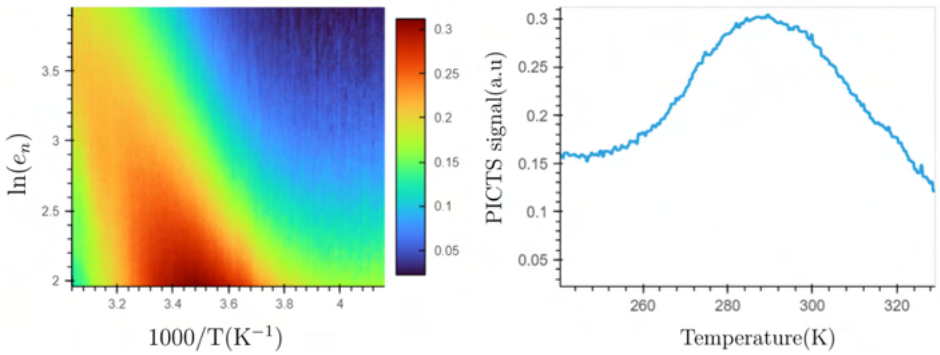

SC_PT_15″

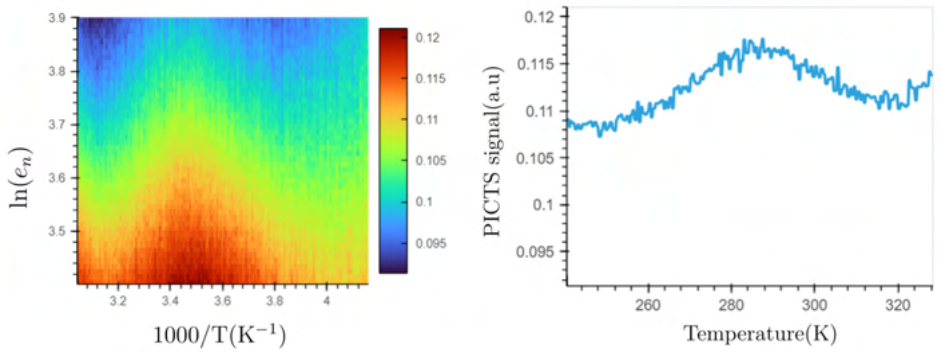

SC_PT_1′

Figure 3.50: PICTS maps of SCs.

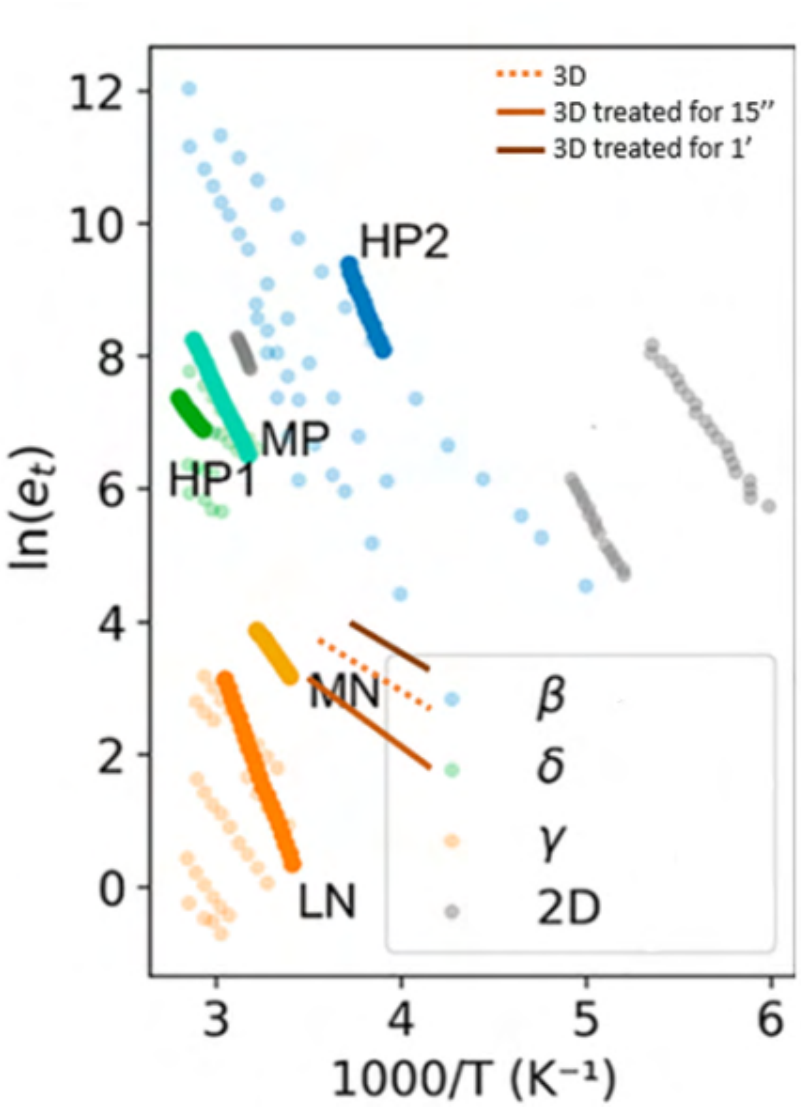

Figure 3.51: Arrhenius plots of PICTS signatures measured on SCs pristine and treated and those reported in literature[15][22] for ions migration in 3D $MAPbBr_2$ and PEA_2PbBr_4 (2D perovskite). In this graph the signature are labelled according to light pulse frequency (low-L, medium-M, high-H) and the sign of applied voltage(N-negative, P-positive)[15]. Moreover according to Reichert et al. notation[23] the ion migration defects due to methylammonium interstitials are labelled with β, whereas those due to bromine vacancy with γ, δ.

Chapter 4

Conclusion

This thesis work has two purposes. The first is to find the best process to fabricate 2D/3D perovskite structure. The second is to verify if the construction of a thin 2D perovskite layer on the 3D surface has passivated the surface defects and has improved the charge transport in 3D perovskite. The analysis on fabrication of 2D/3D perovskite structure has shown that only the PEA+Toluene treatment for 3 and 10 minute is efficient to fabricate a 2D/3D perovskite structure. In particular the time of treatment of 3 minute is enough to fabricate a 2D perovskite with layer n=1 on the 3D surface, whereas that of 10 minute a 2D perovskite with layer n=1 and n=2. The analysis performed in the second part of this work on thin films show that the time of treatment of 15 second does not produce a 2D/3D perovskite structure, whereas that of 1 minute builds a thin 2D perovskite with n=1 on the surface of 3D perovskite. For single crystals, instead the time of treatment of 15 second is enough to produce a 2D perovskite with layer n=1, whereas that of 1 minute produces a 2D with layers n=1 and n=2.
The I-V measurements do not produce a clear difference between treated and pristine thin films and single crystals, showing that the charge transport does not improve upon the treatments. Moreover it was observed that the I-V curves of thin films pristine and treated have an ohmic behaviour and show current values in vacuum of 2-3 order of magnitude lower than air. This is due to presence of grain boundaries which in air capture water and oxygen molecules and improves the overall charges transport. Unlike thin film, the I-V curves of pristine and treated single crystals show the same current value in dark and in air and they are asymmetric with the current at +20V of almost one order of magnitude higher than that at -20V. The same current value in dark and air is due to the absence of grain boundaries. The asymmetry of curves can be explained by the top-bottom contact geometry of the electrodes used to perform I-V measurements and by higher mobility of holes than electrons which allows the holes to reach quickly the contact compared to electrons. The ions activation energies for thin films, calculated by Nernst-Einstein fit, are higher compared to those found for single crystals. This can be explained by a potential barrier at grain boundaries which limits the ions movement,

but not that of charge carriers (holes or electrons). Moreover, it was possible to observe for thin films that ions activation energies show a trend with time of treatment. This is explained by a change of dimension in grain boundaries observable in S.E.M micrographs. The low value of ions activation energies in pristine and treated single crystals means that ions give an important contribution to conductivity. The plot of conductivity versus 1/T in the Nernst-Einstein formalism has shown that for thin films there is another activation energy which may be attribute to electronic conductivity.
The PICTS measurements performed on thin films allowed to detect the photocurrent signal for thin film pristine and treated for 15 second and 1 minute, but not the PICTS signal. The absence of PICTS signal is related to the lack of a proper temperature dependence of the photocurrent. However, the shape of photocurrent signal, the decay time of photocurrent and the frequency at which the photogenerated carriers are created indicated that the nature of defect states in thin films may not have a ionic nature. The PICTS measurements allowed to detect PICTS signal for single pristine and treated from which it was possible to calculate the PICTS maps. By comparing the traces of Arrhenius plot with those reported in literature for ions migration it was identified the bromine vacancy as main defects in both pristine and treated single crystals. The same kind of defect states found for single crystals pristine and treated allowed to conclude that the PEA+Toluene treatment is not efficient to passivate bromine vacancy.

Bibliography

[1] A decade of perovskite photovoltaics, Nat Energy 4, 1 (2019), https://doi.org/10.1038/s41560-018-0323-9

[2] Gregor Kieslich, Shijing Suna, Anthony K. Cheetham, Solid-state principles applied to organic–inorganic perovskites: new tricks for an old dog, Chem. sci, 2014 (5) 4712-4715, https://doi.org/10.1039/C4sc02211D

[3] R. D. Shannon, Revised effective ionic radii and systematic studies of interatomic distances in halides and chalcogenides, Acta Cryst. (1976). A32, 751-767 https://doi.org/10.1107/S0567739476001551

[4] M. Songvilay, M. Bari, Z.-G. Ye, Guangyong Xu, P. M. Gehring, W. D. Ratcliff, K. schmalzl, F. Bourdarot, B. Roessli, and C. Stock, Lifetime-shortened acoustic phonons and static order at the Brillouin zone boundary in the organic-inorganic perovskite $CH_3NH_3PbCl_3$, Phys. Rev. Materials 2018 (2), 123601 https://link.aps.org/doi/10.1103/PhysRevMaterials.2.123601

[5] Hybrid Perovskite Solar Cells: Characteristics and Operation, Hiroyuki Fujiwara, 2022 Wiley-vch, https://onlinelibrary.wiley.com/doi/book/10.1002/9783527825851

[6] Giulia Grancini, Mohammad Khaja Nazeeruddin, Dimensional tailoring of hybrid perovskites for photovoltaics, Nat Rev Mater 2019 (4), 4–22, https://doi.org/10.1038/s41578-018-0065-0

[7] Nicola Sestu, Michele Cadelano, Valerio Sarritzu, Feipeng Chen, Daniela Marongiu, Roberto Piras, Marina Mainas, Francesco Quochi, Michele Saba, Andrea Mura, and Giovanni Bongiovanni, Absorption F-Sum Rule for the Exciton Binding Energy in Methylammonium Lead Halide Perovskites, The Journal of Physical Chemistry Letters 2015 6 (22), 4566-4572, https://doi.org/10.1021/acs.jpclett.5b02099

[8] Fabrizio Mariano, Arianna Cretì, Luigi Carbone, Armando Genco, Stefania D'Agostino, Sonia Carallo, Giovanni Montagna, Mauro Lomascolo, Marco Mazzeo,

Saha equilibrium in trap passivated $CH_3NH_3PbBr_3$ perovskite, Commun Phys 2020 3, 41, https://doi.org/10.1038/s42005-020-0309-3

[9] Heejae Lee, Sofia Gaiaschi, Patrick Chapon, Denis Tondelier, Jean-Eric Bourée, Yvan Bonnassieux, Vincent Derycke, and Bernard Geffroy,Effect of Halide Ion Migration on the Electrical Properties of Methylammonium Lead Tri-Iodide Perovskite Solar Cells, the Journal of Physical Chemistry C 2019 123 (29), 17728-17734, https://pubs.acs.org/doi/10.1021/acs.jpcc.9b04662

[10] Junsang Cho, Jeffrey T. DuBose, An Ngoc Thien Le, and Prashant V. Kamat, Suppressed Halide Ion Migration in 2D Lead Halide Perovskites, ACS Materials Letters 2020 2 (6), 565-570, https://pubs.acs.org/doi/abs/10.1021/acsmaterialslett.0c00124

[11] Po-Cheng Huang, Shao-Ku Huang, Ting-Chun Lai, Min-Chuan Shih, Hung-Chang Hsu, Chun-Hsiang Chen, Cheng-Chieh Lin, Chun-Hao Chiang, Chi-Ying Lin, Kazuhito Tsukagoshi, Chun-Wei Chen, Ya-Ping Chiu, Shiow-Fon Tsay, Ying-Chiao Wang, Visualizing band alignment across 2D/3D perovskite heterointerfaces of solar cells with light-modulated scanning tunneling microscopy, Nano Energy, 2021,89 (A),106362, https://www.sciencedirect.com/science/article/pii/S2211285521006170

[12] Constantinos C. Stoumpos, Duyen H. Cao, Daniel J. Clark, Joshua Young, James M. Rondinelli, Joon I. Jang, Joseph T. Hupp, and Mercouri G. Kanatzidis, Ruddlesden–Popper Hybrid Lead Iodide Perovskite 2D Homologous Semiconductors, https://pubs.acs.org/doi/10.1021/acs.chemmater.6b00847

[13] M. Pratheek, T. Abhinav, Susmita Bhattacharya, Goutam Kumar Chandra, P. Predeep, Recent progress on defect passivation in perovskites for solar cell application, Materials science for Energy Technologies, 2021 (4), 282-289, https://doi.org/10.1016/j.mset.2021.07.003

[14] Pecunia, Vincenzo and Zhao, Jing and Kim, Chaewon and Tuttle, Blair R. and Mei, Jianjun and Li, Fengzhu and Peng, Yueheng and Huq, Tahmida N. and Hoye, Robert L. Z. and Kelly, Nicola D. and Dutton, Siân E. and Xia, Kai and MacManus-Driscoll, Judith L. and Sirringhaus, Henning, Assessing the Impact of Defects on Lead-Free Perovskite-Inspired Photovoltaics via Photoinduced Current Transient Spectroscopy, Advanced Energy Materials, 2021 11 (22) 2003968, https://doi.org/10.1002/aenm.202003968

[15] Giovanni Armaroli, Lorenzo Maserati, Andrea Ciavatti, Pierpaolo Vecchi, Alberto Piccioni, Martina Foschi, Valentina Van der Meer, Chiara Cortese, Matias Feldman, Vito Foderà, Thibault Lemercier, Julien Zaccaro, Javier Mayén Guillén,

Eric Gros-Daillon, Beatrice Fraboni, and Daniela Cavalcoli, Photoinduced Current Transient Spectroscopy on Metal Halide Perovskites: Electron Trapping and Ion Drift,ACS Energy Letters 2023 8 (10), 4371-4379, https://doi.org/10.1021/acsenergylett.3c01429

[16] Patrycja Makuła, Michał Pacia, and Wojciech Macyk, How To Correctly Determine the Band Gap Energy of Modified Semiconductor Photocatalysts Based on UV–Vis Spectra, The Journal of Physical Chemistry Letters 2018 9 (23), 6814-6817, https://doi.org/10.1021/acs.jpclett.8b02892

[17] Yun Lin, Yang Bai, Yanjun Fang, Zhaolai Chen, Shuang Yang, Xiaopeng Zheng, Shi Tang, Ye Liu, Jingjing Zhao, and Jinsong Huang, Enhanced Thermal Stability in Perovskite Solar Cells by Assembling 2D/3D Stacking Structures, The Journal of Physical Chemistry Letters 2018 9 (3), 654-658, https://doi.org/10.1021/acs.jpclett.7b02679

[18] Luoran Chen, Hu Wang, Wenqing Zhang, Fenghua Li, Zhiyuan Wang, Xueyan Wang, Yuchuan Shao, and Jianda Shao, Surface Passivation of $MAPbBr_3$ Perovskite Single Crystals to Suppress Ion Migration and Enhance Photoelectronic Performance, ACS Applied Materials & Interfaces 2022 14 (8), 10917-10926, https://doi.org/10.1021/acsami.1c21948

[19] Yingjun Chai, Zhili Juan, Ye Wu, Yang Liu, and Xiaoming Li, Suppressing the Ion Migration in Halide Perovskite Wafers for Current-Drift Free X-ray Detectors, ACS Applied Electronic Materials 2023 5 (1), 544-551, https://doi.org/10.1021/acsami.1c21948

[20] Eya Belarbi, Marta Vallés-Pelarda,Bruno Clasen Hames, Rafael S. Sanchez, Eva M. Barea, Hager Maghraoui-Meherzi, Iván Mora-Seró, Transformation of PbI_2, $PbBr_2$ and $PbCl_2$ salts into $MAPbBr_3$ perovskite by halide exchange as an effective method for recombination reduction https://doi.org/10.1039/C7CP01192J

[21] Lucie McGovern, Isabel Koschany, Gianluca Grimaldi, Loreta A. Muscarella, and Bruno Ehrler Grain Size Influences Activation Energy and Migration Pathways in $MAPbBr_3$Perovskite Solar Cells, the Journal of Physical Chemistry Letters 2021 12 (9), 2423-2428, https://doi.org/10.1021/acs.jpclett.1c00205

[22] Oriane Baussens, Loli Maturana, Smaïl Amari, Julien Zaccaro, Jean-Marie Verilhac, Lionel Hirsch, Eric Gros-Daillon, An insight into the charge carriers transport properties and electric field distribution of $CH_3NH_3PbBr_3$ thick single crystals, Applied Physics Letters, 2020, 117 (4), pp.041904,https://hal.science/hal-02947932/file/APL20-AR-03618.pdf

[23] Sebastian Reichert, Qingzhi An, Young-Won Woo, Aron Walsh, Yana Vaynzof, Carsten Deibel, Probing the ionic defect landscape in halide perovskite solar cells, Nat Commun 11, 6098 (2020), https://doi.org/10.1038/s41467-020-19769-8

[24] Daniele Meggiolaro, Edoardo Mosconi, and Filippo De Angelis, Formation of Surface Defects Dominates Ion Migration in Lead-Halide Perovskites, ACS Energy Letters 2019 4 (3), 779-785, https://doi.org/10.1021/acsenergylett.9b00247

[25] Carlos Pereyra, Haibing Xie, Mónica Lira-Cantu, Additive engineering for stable halide perovskite solar cells, Journal of Energy Chemistry, 2021 60(9), 599-634 https://doi.org/10.1016/j.jechem.2021.01.037

[26] Mayuribala Mangrulkar, Keith J. Stevenson, The Progress of Additive Engineering for $CH_3NH_3PbI_3$Photo-Active Layer in the Context of Perovskite Solar Cells, Crystals 2021, 11(7), 814, https://doi.org/10.3390/cryst11070814

[27] https://www.nrel.gov/pv/cell-efficiency.html

[28] Eun-Bi Kim, M. Shaheer Akhtar, Hyung-Shik Shin, Sadia Ameen, Mohammad Khaja Nazeeruddin, A review on two-dimensional (2D) and 2D-3D multidimensional perovskite solar cells: Perovskites structures, stability, and photovoltaic performances, Journal of Photochemistry and Photobiology C: Photochemistry Reviews, 2021, 48, 100405, https://www.sciencedirect.com/science/article/pii/S1389556721000046

[29] Chaoyan Ma, Chongqian Leng, Yixiong Ji, Xingzhan Wei, Kuan Sun, Linlong Tang, Jun Yang,a Wei Luo, Chaolong Li, Yunsheng Deng, Shuanglong Feng, Jun Shen,a Shirong Lu, Chunlei Du and Haofei Shi, 2D/3D perovskite hybrids as moisture-tolerant and efficient light absorbers for solar cells